UNIVERSITY OF CALIFORNIA, SAN DIEGO

Relaxation Phenomena in Rechargeable Battery Electrode Materials Beyond Li Intercalation

A dissertation submitted in partial satisfaction of the
requirements for the degree Doctor of Philosophy

in

Chemical Engineering

by

JaeWook Shin

Committee in charge:

Professor Ying Shirley Meng, Chair
Professor Jan B. Talbot, Co-Chair
Professor Seth M. Cohen
Professor Francesco Paesani
Professor Kesong Yang

2016

The Dissertation of JaeWook Shin is approved, and it is acceptable in quality and form for publication on microfilm and electronically:

Co-Chair

Chair

University of California, San Diego

2016

TABLE OF CONTENTS

LIST OF FIGURES

LIST OF TABLES

ACKNOWLEDGEMENTS

First of all, I would like to thank my thesis advisor Dr. Ying Shirley Meng for providing me all the opportunities to do this research and her continuous support and good advice throughout the projects. I was sincerely honored to meet and work with her and I shall never forget her endless advice and help for the past five years. I would like to express the deepest gratitude to my other committee members: Prof. Seth M. Cohen, Prof. Francesco Paesani, Prof. Jan B. Talbot, and Prof. Kesong Yang for their time and guidance.

Secondly, I would like to acknowledge my collaborators and co-authors in UCSD, Prof. Min Kim, Prof. Jordi Cirera, Prof. Joseph Wang, Dr. Dae Hoe Lee, Dr. Jing-Min You, Dr. Tom Yersak, Rajan Kumar, Justin Liu, Hitoshi Shobukawa, Judith Alvarado with whom I had many useful and stimulating discussions. I am also grateful to all my group members in Laboratory for Energy Storage and Conversion (LESC) who have helped and inspired me in many ways.

Chapter 1, in part, is a reprint of the material "MIL-101(Fe) as a lithium-ion battery electrode material_ a relaxation and intercalation mechanism during lithium insertion" as it appears in the Journal of the Material Chemistry A, Jaewook Shin, M. Kim, J. Cirera, S. H. Chen, G. Halder, T. A. Yersak, F. Paesani, S. M. Cohen and Y. S. Meng, 2015, 3, 4738. The dissertation author was the primary investigator and author of this paper.

Chapter 1, in part, is currently being prepared for submission for publication of the material "Manganese Based Oxides as Electrode Materials in Energy Storage Devices: A Review" The dissertation author was the primary investigator and author of this paper.

Chapter 2, in part, is currently being prepared for submission for publication of the material “Manganese Based Oxides as Electrode Materials in Energy Storage Devices: A Review” The dissertation author was the primary investigator and author of this paper.

Chapter 4, in part, is a reprint of the material “MIL-101(Fe) as a lithium-ion battery electrode material_ a relaxation and intercalation mechanism during lithium insertion” as it appears in the Journal of the Material Chemistry A, Jaewook Shin, M. Kim, J. Cirera, S. H. Chen, G. Halder, T. A. Yersak, F. Paesani, S. M. Cohen and Y. S. Meng, 2015, 3, 4738. The dissertation author was the primary investigator and author of this paper.

Chapter 5, in part, is a reprint of the material “Relaxation of ZnO on Bismuth Species Towards Rechargeable Zn-based Aqueous Battery” as it appears in the Physical Chemistry Chemical Physics, Jaewook Shin, R. J.-M. You, J. Lee, R. Kumar, L. Yin, J. Wang, and Y. S. Meng,, 2016, accepted manuscript. The dissertation author was the co-primary investigator and author of this paper.

Chapter 6, in part, is a reprint of the material “Relaxation of ZnO on Bismuth Species Towards Rechargeable Zn-based Aqueous Battery” as it appears in the Physical Chemistry Chemical Physics, Jaewook Shin, R. J.-M. You, J. Lee, R. Kumar, L. Yin, J. Wang, and Y. S. Meng,, 2016, accepted manuscript. The dissertation author was the co-primary investigator and author of this paper.

Chapter 7, in part, is currently being prepared for submission for publication of the material “Manganese Based Oxides as Electrode Materials in Energy Storage Devices: A Review” The dissertation author was the primary investigator and author of this paper.

I would like to acknowledge the financial support from the Interdisciplinary Research Award Celebration, an UCSD chancellor's research award and advanced research projects agency - energy (ARPA-E), U.S. Department of Energy, under award number DE-AR0000535.

For the last but not least, my deepest gratitude goes to my parents Wan-Sup Shin and SooKyung You for their love, patience, and never-ending support during my Ph.D.

VITA

2011 Bachelor of Science, University of California, San Diego, USA

2016 Doctor of Philosophy, University of California, San Diego, USA

PUBLICATIONS

1. Jaewook Shin, R. J.-M. You, J. Lee, R. Kumar, J. Wang, and Y. S. Meng, **Relaxation of ZnO on Bismuth Species Towards Rechargeable Zn-based Aqueous Battery**, *Physical Chemistry Chemical Physics*, 2016, 18, 26376. (outside back cover)

2. H. Shobukawa, Jaewook Shin, Judith Alvarado, Cyrus S. Rustomji, and Y. S. Meng, **Electrochemical Reaction and Surface Chemistry for Performance Enhancement of Si Composite Anode Using Bis(fluorosulfonyl)imide Based Ionic Liquid**, *Journal of Material Chemistry A*, 2016, 4, 15117.

3. Jaewook Shin, R. Kumar, J.-M. You L. Yin, Y. S. Meng and J. Wang, **All-Printed, Intrinsically Stretchable, Rechargeable, and Wearable Zn-Ag Battery via Stretchable Binder**, *Submitted Manuscript*.

4. Jaewook Shin, R. Yaylian, J. K. Seo, A. Huang, and Y. S. Meng, **Manganese Based Oxides as Electrode Materials in Energy Storage Devices: A Review**, *Manuscript Under Preparation*.

5. Changrong Zhu, Lu Yang, Joon Kyo Seo, Xiao Zhang, Linyi Bai, Jaewook Shin, Hua Zhang, Y. Shirley Meng, and Hong Jin Fan, **Core-branched MnO2 Heterostructure Nanowires with Enhanced Pseudocapacitive Properties**, *Manuscript Under Preparation.*

6. Jaewook Shin, M. Kim, J. Cirera, S. H. Chen, G. Halder, T. A. Yersak, F. Paesani, S. M. Cohen and Y. S. Meng, "**MIL-101(Fe) as a lithium-ion battery electrode material_ a relaxation and intercalation mechanism during lithium insertion**" , *Journal of Materials Chemistry A*, 2015, 3, 4738.

7. T. A. Yersak, Jaewook Shin, Z. Wang, D. Estrada, J. Whiteley, S-H Lee, M. J. Sailor, and Y. S. Meng, "**Preparation of Mesoporous Si@PAN Electrodes for Li-Ion Batteries via the In-Situ Polymerization of PAN**", *ECS Electrochemistry Letters*, 2015, 4 (3), A33.

8. Honghan Fei, Jaewook Shin, Ying Shirley Meng, Mario Adelhardt, Jorg Sutter, Karsten Meyer, and Seth M. Cohen, **Reusable Oxidation Catalysis Using Metal-**

Monocatecholato Species in a Robust Metal−Organic Framework, *Journal of the American Chemical Society*, 2014.

ABSTRACT OF THE DISSERTATION

Relaxation Phenomena in Rechargeable Battery Electrode Materials

Beyond Li Intercalation

by

JaeWook Shin

Doctor of Philosophy in Chemical Engineering

University of California, San Diego, 2016

Professor Ying Shirley Meng, Chair

Professor Jan B. Talbot, Co-Chair

An intercalation reaction is the most commonly utilized redox reaction scheme for commercial Li-ion batteries (LIBs) due to minimized crystal deformation during the redox reaction. However, to meet the growing demands for large-scale energy storage

criteria, low cost and high energy density, other reaction schemes need to be explored. In order to fully utilize the new schemes, mechanistic understanding of the respective materials is crucial. A relaxation phenomenon facilitates the mechanistic understanding because it inspects both kinetic and thermodynamic products of the reaction.

MIL-101(Fe), a MOF material is applied to study the relaxation phenomenon. MIL-101(Fe) demonstrates a unique rate dependent rechargeability. Through X-ray absorption spectroscopy and electronic state calculation, a kinetically stable product and thermodynamically stable product of MIL-101(Fe) are proposed. Kinetically, Fe^{3+} is reduced upon reduction, however, due to thermodynamic stability, the Fe^{2+} self oxidizes back to Fe^{3+} after relaxation. This work demonstrates relaxation phenomenon on the molecular level.

Zn electrode is one of the conversion materials with high energy density, yet Zn electrode lacks rechargeability due to the zincate ion formation during oxidation reaction. The zincate ions dissolve into electrolyte making the Zn electrode not rechargeable. One of the ways to overcome this issue is incorporating Bi_2O_3 as a composite additive. We have added the Bi_2O_3 additive and identified a comprehensive role of the Bi_2O_3. Through electron microscopy coupled with energy dispersed X-ray spectroscopy and X-ray photoelectron spectroscopy, we have discovered that the ZnO and Bi_2O_3 form an intermediate phase that allows zincate ions to deposit and retain ZnO on the electrode surface. This work demonstrates relaxation phenomenon on the particle level.

Understanding the relaxation phenomenon upon redox reactions distinguishes the kinetic and thermodynamic products. The findings in this dissertation provide more comprehensive methods to identify the energy storage mechanism. MnO_2 is one of the

low-cost, environmentally benign, and promising material for energy storage system. A preliminary Mn^{2+} deposition test suggested that Bi_2O_3 addition can adhere Mn^{2+}. Based on the knowledge gained through relaxation characterization, a series of characterizations and methods to improve MnO_2 aqueous energy storage system are proposed.

Chapter 1. Introduction

1.1. Li-ion batteries and intercalation reaction

Power generation on a grid-scale is a complicated system in which various power generating methods are available. A large-scale energy storage system provides substantial benefits to an electric power grid.[1] Without the energy storage system accompanying the power generation, constant high power must be generated most of the time. Since the consumers' need for the power fluctuates throughout the day, excess power is generated that can be wasted without the energy storage system. The load leveling is to store and utilize the excess energy when needed (**Figure 1.1**).[2] Currently, less than 2.5% of the total electric power delivered in the United States uses energy storage system (**Figure 1.2**).[2, 3] The need for the large-scale energy storage system is evident. As an energy storage device, the pumped hydroelectric system is the dominant system, however, it suffers from a geometric constraint. In addition, the pumped hydroelectricity has the efficiency of 75-80%.[4] To gain flexible installation with higher efficiency, electrical energy storage system (EESS) is favored. While hydroelectricity stores the energy in a form of displacement and converts it to electricity, the EESS stores the energy in the form of electricity. Energy stored in the EESS can be directly utilized in the grid.

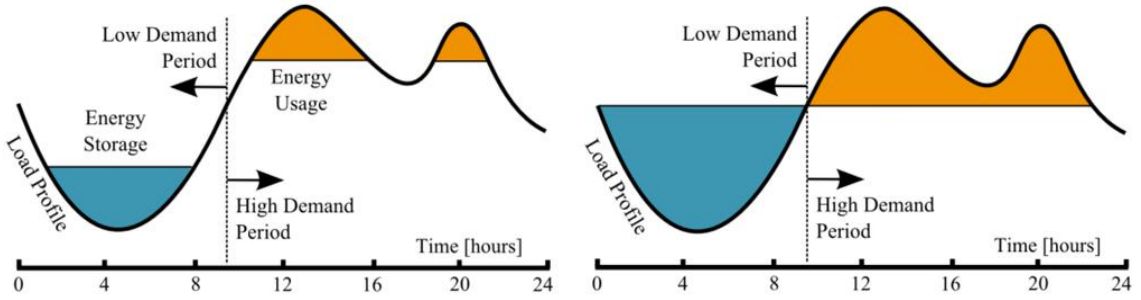

Figure 1.1. Consumer energy demands (load profile) over a 24 h period. The figure on the left shows a typical application of energy storage. While other intermediate applications exist, arguably, the ultimate goal of energy storage is load leveling as shown on the right.[2, 5]

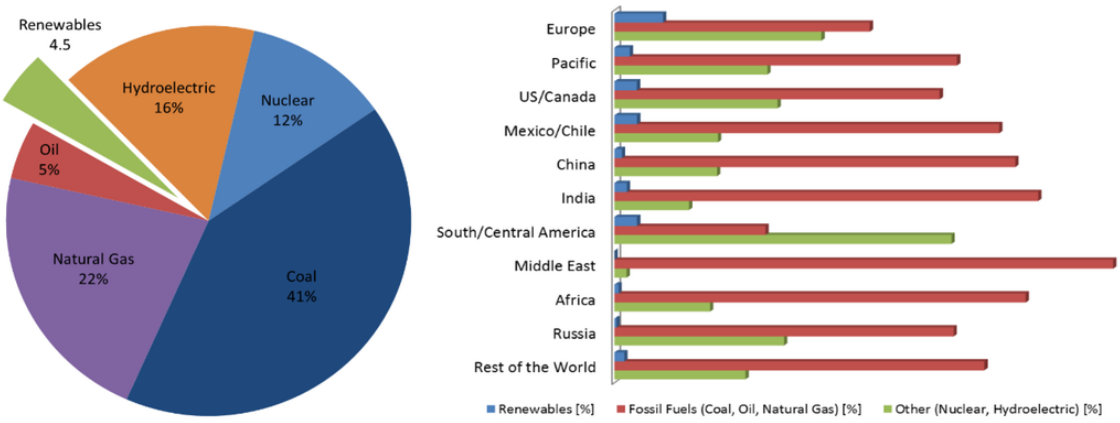

Figure 1.2. The worldwide distribution of electricity production in 2011 (on the left). The national reliance for electricity production as of 2010 (on the right).[2, 6, 7]

Li-ion battery (LIB) is a device that stores electrical energy to power various portable electronics. **Figure 1.3** illustrates the operating mechanisms of LIB. LIB consists of a cathode and an anode electrode separated by a separator with an electrolyte.[8] The energy is stored in a form of electrons. When the electron migrates from one electrode to the other, this creates reduction reaction and oxidation reaction in each electrode. Among various redox reactions, intercalation reaction is one of the most popular and stable reaction schemes for the LIBs.[9-11] In the intercalation reaction, electrons migrate through

an external circuit and Li^+ ions migrate in the same direction through the electrolyte. In order to have a stable retention over prolonged cycles, the electrode materials that hold the electrons and the ions must be stable throughout the redox reaction. During charge, the electrons and the ions migrate from cathode to anode. During discharge, the electrons and ions migrate from anode to cathode. The amount of the migration per cell, per mass, per volume, or per surface area represents the amount of energy stored in a respective unit. Maximizing the amount of migration boosts the energy density, yet it needs to be carefully done. Excessive migration can jeopardize the stability of the electrode materials and lead to degradation in the prolonged cycle stability.[12]

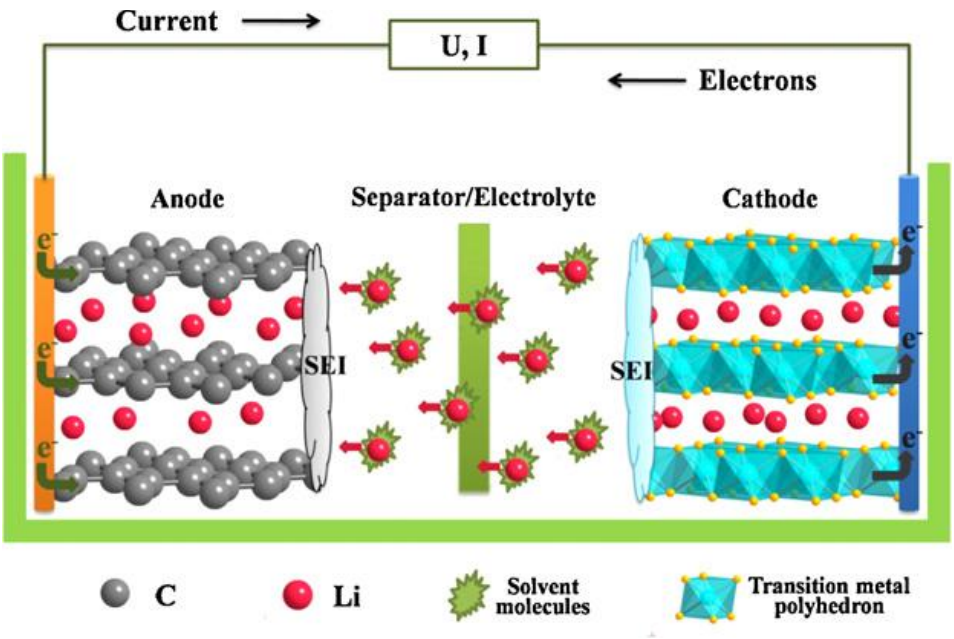

Figure 1.3. Schematic representation and operating principles of Li batteries.[8]

Optimizing the amount of migration and the stability is vital in achieving the commercial LIB cells. Among numerous candidates, three forms of metal oxides are

currently popular as commercial materials (**Figure 1.4**). Firstly, $LiCoO_2$ is a layered material. Li has a two-dimensional diffusion pathway. This layered material can extract half a mole of Li reversibly.[13, 14] Further extraction causes a major crystal deformation that is irreversible. Secondly, $LiMn_2O_4$ is a spinel material.[15, 16] Li has a three-dimensional diffusion pathway. This spinel material can extract all the Li reversibly. However, it lacks electrical conductivity compared to that of the $LiCoO_2$. The lack of electrical conductivity hinders the electron migration. Lastly, $LiFePO_4$ is an olivine material. The Li has one-dimensional diffusion pathway.[17, 18] Although this olivine material has lowest electrical conductivity, it is very stable and can synthesize extremely small particles with high surface area to dramatically shorten the Li diffusion length. As a result, $LiFePO_4$ is mostly known for high power applications. High power applications require the materials to maintain a high voltage at a high current density or rate of electron and the ion migration.

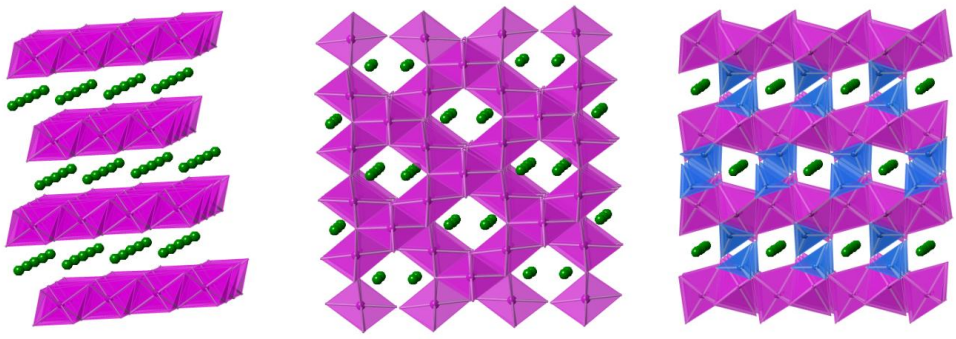

Figure 1.4. Structures of the conventional intercalation based cathode materials. (a) Layer, (b) spinel, and (c) olivine structure (green: Li-ions; pink: TM-ions; blue: P-ions)

1.2. Metal-organic frameworks as LIB material

Rechargeable LIBs are essential in developing smartphones, laptop computers, and many other technologies including grid energy storage.[19] However, the materials used in commercial LIBs are far too expensive and energy intensive for large-scale grid storage applications.[19-22] For example, layered oxide cathode materials are costly because they require a high-temperature synthesis process and contain expensive transition metals such as Co.[23-26] Often times, these cathode materials are synthesized at around 1000 ℃ for several hours. Synthesizing at such a high temperature over a long period of time requires high energy. Even if the battery materials can save energy by storing and releasing energy when necessary, the amount of energy to make such a material is high, the net save can be sacrificed. Furthermore, the energy efficiency dramatically reduces as the utilizing temperature increases because of heat dissipation (**Figure 1.5**). The cost of synthesizing the active material can be greatly lowered reduced if the synthesis temperature decreases. In order to reduce the cost of LIBs for grid-scale applications, metal-organic framework (MOF) cathode materials could be applied. MOF materials offer several advantages with respect to other porous materials owing to their flexible synthetic routes, low-temperature synthesis, and comparatively inexpensive precursor materials.[27]

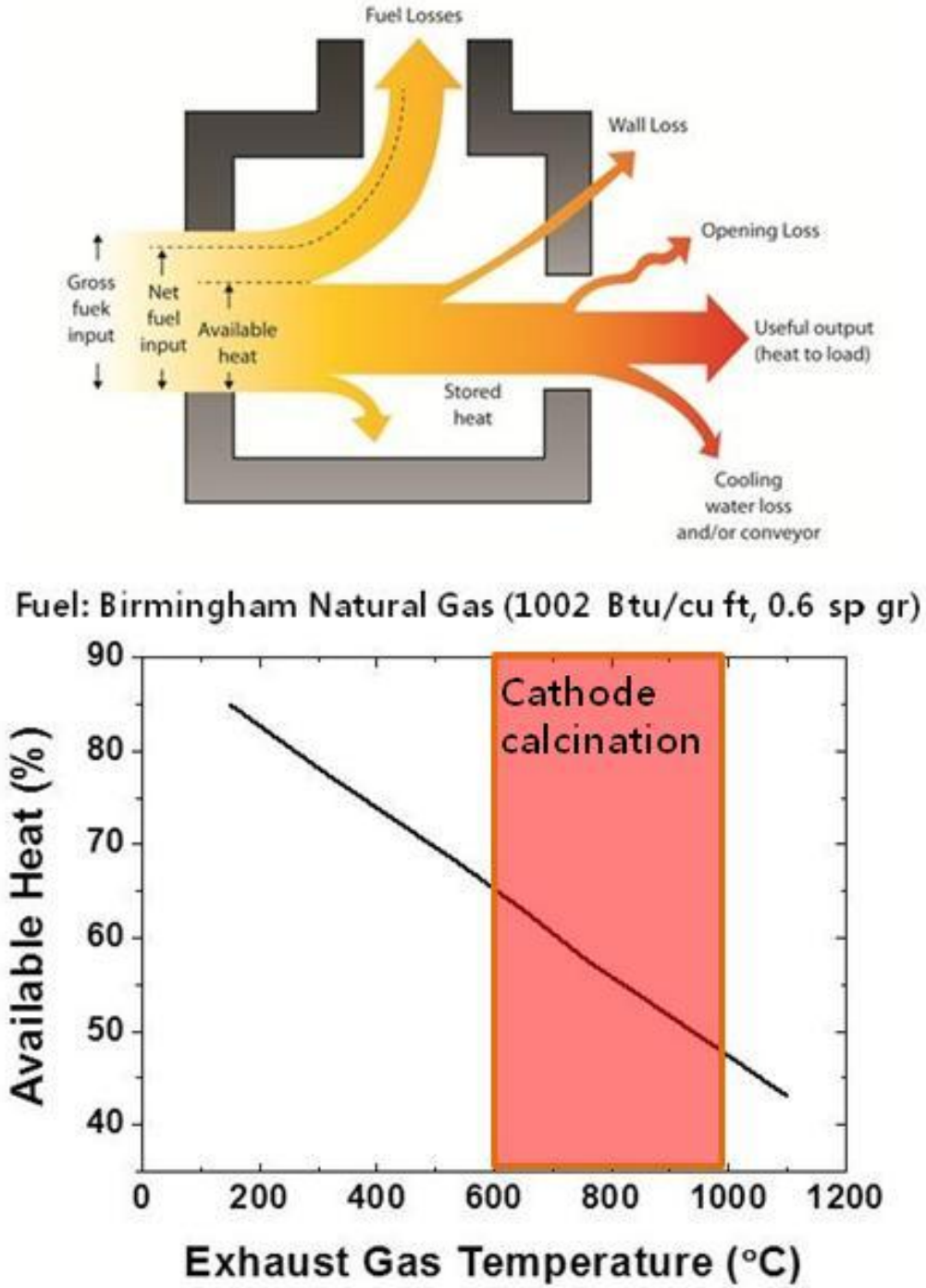

Figure 1.5. Top: Heat dissipation scheme in a typical furnace. Bottom: Available heat efficiency with respect to the furnace temperature.[28, 29]

MOFs represent a relatively new class of porous materials assembled from two main components: an inorganic secondary building unit (SBU) and an organic linker (**Figure 1.6**).[30, 31] The SBUs are generally comprised of transition metal ions or small metal clusters, while the organic linkers include a wide range of molecules, such as dicarboxylates, with 1, 4-benzene dicarboxylic acid (H_2bdc) which are most commonly used ligands.[32] In LIB, the MOFs have been applied as active electrode materials, separator, and solid-state electrolyte. The MOFs have micro channels of high porosity, which can be functionalized via pre-synthetic methods and post-synthetic methods. Especially, when the channel is functionalized with a strong dielectric group, this can bridge the Li^+ ion and facilitate Li^+ diffusion. Due to this functionality, MOFs have been utilized as a separator and solid-state electrolyte. The advantage of such applications is safety. The commercial LIB cells utilize organic electrolyte. The molecules utilized for the electrolyte are highly flammable. Utilizing inflammable MOF allows one to fabricate a safe battery.

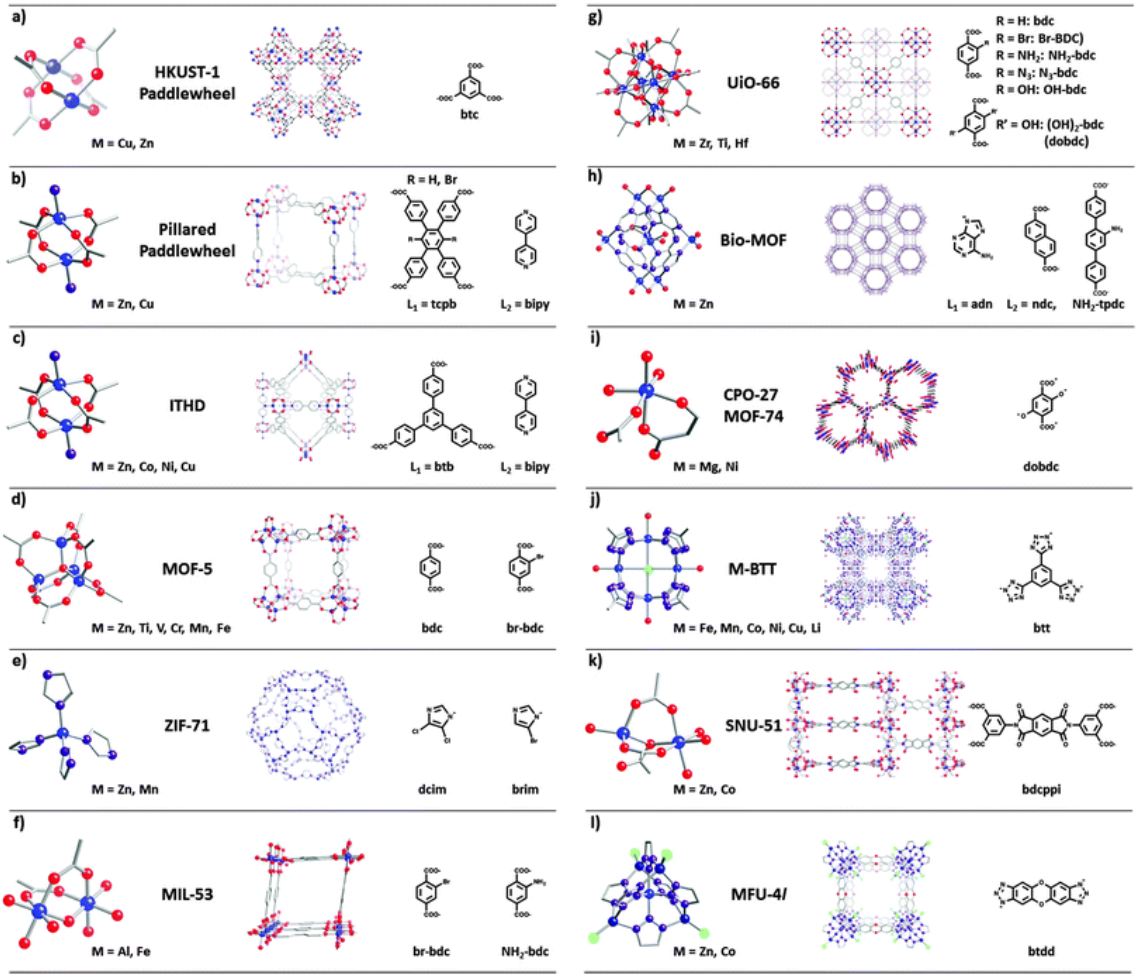

Figure 1.6. Lattice structures (middle), corresponding SBUs (metal nodes; left), and organic linkers (right) of the MOFs discussed in this review. (Atom definition: blue – metal, red – oxygen, purple – nitrogen, grey – carbon, and green – chlorine.).[31]

In terms of MOFs' use as an active electrode material, the Zn_4O(4,4',4''-benzene-1,3,5-triyl-tri-benzoate)$_2$ (MOF-177) is the first MOF to be studied as a host for a lithium insertion.[33] Unfortunately, MOF-177 does not exhibit good electrochemical reversibility. Shortly after this initial study, two Fe^{3+}-based MOFs – $Fe(OH)_{0.8}F_{0.2}$(bdc) (MIL-53(Fe)) and FeOH(bdc) (MIL-68(Fe), MIL = Materials of Institut Lavoisier) – were synthesized and tested as battery materials.[34, 35] MIL-53(Fe) exhibits good electrochemical reversibility and is superior to MIL-68(Fe).[14,15] However, the synthesis of MIL-53(Fe)

requires HF, which limits its potential as a large-scale grid storage battery material. To avoid the use of HF, MIL-101(Fe) can be chosen as an electrode candidate.

1.3. Conversion reaction

Conversion reaction in the energy storage system is a type of redox reaction. Unlike intercalation where the reaction intercalates Li in and out of a host structure without significantly altering the host crystal structure, conversion reaction completely alters the host crystal structure (**Figure 1.7**). Intercalating Li without significantly altering the host structure limits the amount of Li available for intercalation.[36, 37] Removing or inserting too much Li leads to significant structural degradation. The amount of available Li intercalation depends on crystal structural Li sites and transition metal stable oxidation states.[38] Due to these two reasons, the amount of intercalation reactions is often limited to one or less electron per molecular formula. On the other hand, the conversion reactions utilize two or more electron per molecular formula. As a result, the conversion reactions have more than twice the capacity compared to that of the intercalation reactions.[39] However, this excessive amount of redox reaction brings out the complete reconstruction of the crystal structure.[40]

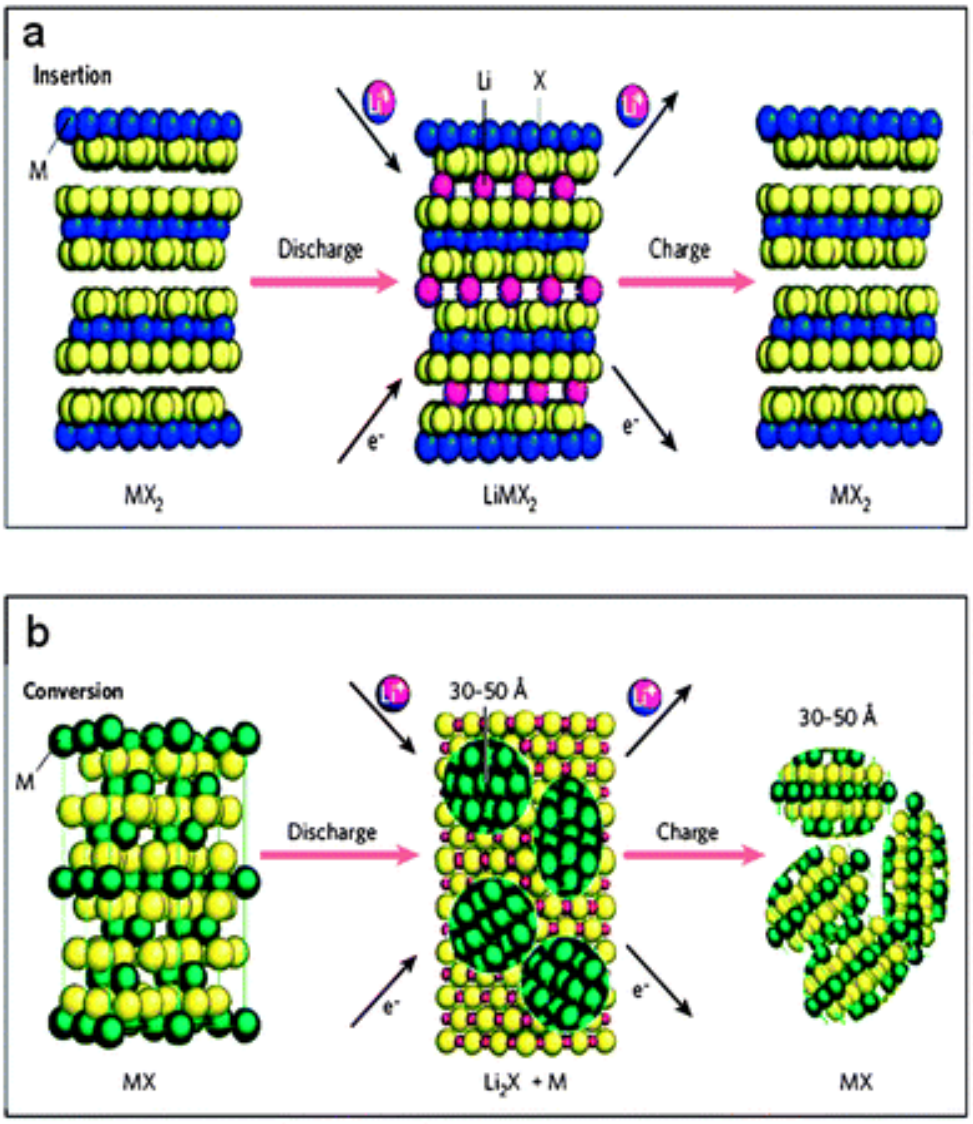

Figure 1.7. Anodes and anode reactions in Li-ion batteries: (a) Insertion reactions, (b) Conversion reactions. M = transition metal.[41]

The intercalation reaction dominates the commercial LIB market because this reaction minimizes the phase transformation and has high rechargeability. Conversion reaction, on the other hand, maximizes the energy density by entirely transforming the crystal phases of the active material.[42] This reconstruction leads to significant volume changes and accompanies a polarization. The volume change in the electrode materials is

unfavorable because this can lead to electrical disconnect.[43-45] Most of the redox-active electrode materials lack electrical conduction. In order to achieve maximum redox activity, electrons must be able to move easily. A conductive additive is added as a composite additive to enhance the electrical conduction. When the electrode materials expand and contract, the electrical connection can be lost, losing redox active particles. Furthermore, when the active materials undergo a crystal reconstruction, the reaction involves nucleation of new materials. For example, CuF_2 reacts to Li to form Cu and LiF.[46-48] Lithiation causes the nucleation of Cu and LiF and delithiation leads to the nucleation of CuF_2. Since nucleation has high activation energy, this causes polarization. The polarization appears as significant voltage hysteresis between charge and discharge.[49]

1.4. Aqueous battery

LIBs have become the alternative energy supply for portable devices.[19] They have excellent energy density and cyclability because the electrode materials host Li^+ without significantly changing its crystal structure.[19] Despite the superior advantages of the LIB's performance, it still suffers from the high fabrication cost and safety issues.[50] The commercial LIB system makes use of organic electrolytes that are stable in wide voltage window. Beck and Ruetschi highlighted the "Three E" criteria; energy, economics, and environment to determine the suitable energy storage system.[51] Utilizing the organic electrolyte allows the batteries to produce high power and energy from its high voltage. However, the organic electrolytes are expensive because they require high purity and are sensitive towards moisture.[52] Furthermore, such electrolytes are flammable, raising safety

concerns. Replacing the organic electrolyte with aqueous electrolyte can drastically reduce the cost of the battery and eliminate the safety concern from flammability.[53]

Large scale EESS is essential for using electricity. In pursuing such EESS, lowering the cost of the battery is vital. To reach this goal, this dissertation has explored two novel chemistries: MIL-101(Fe) and Zn + Bi_2O_3 composite. Both kinetically stable and thermodynamically stable products must be understood to probe the mechanism. A phenomenon that relates these two products is relaxation. The aim of this thesis is to provide methods and comprehension to identify and modify the relaxation phenomenon.

Chapter 1, in part, is a reprint of the material "MIL-101(Fe) as a lithium-ion battery electrode material_ a relaxation and intercalation mechanism during lithium insertion" as it appears in the Journal of the Material Chemistry A, Jaewook Shin, M. Kim, J. Cirera, S. H. Chen, G. Halder, T. A. Yersak, F. Paesani, S. M. Cohen and Y. S. Meng, 2015, 3, 4738. The dissertation author was the primary investigator and author of this paper.

Chapter 1, in part, is currently being prepared for submission for publication of the material "Manganese Based Oxides as Electrode Materials in Energy Storage Devices: A Review" The dissertation author was the primary investigator and author of this paper.

Chapter 2. Relaxation phenomenon in energy storage materials

Until recently, the relaxation phenomenon was mainly described with the IR or voltage drop; a simple electrochemical polarization.[54, 55] During electrochemical bias, especially when a value of current is flowing in one direction, the electrochemical polarization can be observed in various magnitudes. Upon the absence of the current, over a certain period of time, the polarization dissipates as seen by the open circuit voltage. The voltage represents potential difference and has thermodynamic meaning.[56] Observing the voltage provides information in the thermodynamic state of the materials in an electrochemical cell. The electrochemical polarization is representative of the kinetically favored products. After the dissipation of the polarization, the voltage represents the thermodynamically stable products. This dissipation is what is understood as the relaxation phenomenon.[57, 58]

2.1. Relaxation in intercalation reaction

As predominant cathode materials in lithium ion battery systems utilizing the intercalation reaction, the relaxation phenomenon is described as it is related to the intercalation. As mentioned earlier, the intercalation reaction is a reaction in which the electron and cation diffuse in and out of the host material.[19] When electrochemical bias is applied, the diffusions start to occur. Since the electron diffusion is significantly faster than the ion diffusion, the active material may not have an even distribution of the cation throughout the particle.[58] For instance, $LiMn_2O_4$ spinel phase can be delithiated by the current bias (**Figure 2.1**). During the current bias, Li is diffused out starting from the surface.[59, 60] The Li diffusion in the core follows with a lag. Due to this lag, during the

intermediate period, Mn_2O_4 spinel phase forms on the surface and $LiMn_2O_4$ remains in the core. During the intermediate, even if the overall chemical composition is closer to $LiMnO_4$ than the MnO_4, the voltage is that of the MnO_4.[61] When the current bias stops, the Li further diffuses and distributes evenly or thermodynamically. This distribution is the relaxation phenomenon for the intercalation reaction. The voltage at the end of this relaxation represents thermodynamically stable state of the active materials.[62]

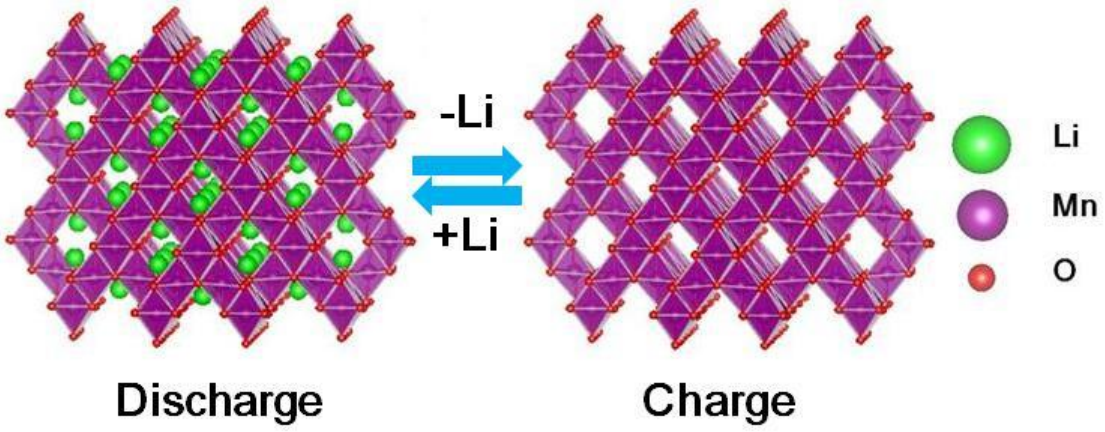

Figure 2.1. Crystal structure of $LiMn_2O_4$ (left) and λ-MnO_2 or Mn_2O_4 spinel (right) after Li has been either etched or diffused out.

Researchers have made strides in improving the electrochemical performance of the LIB electrodes with relaxation phenomenon. For instance, in commercial devices, batteries are charged at a constant current constant voltage (CCCV) step (**Figure 2.2**). This is an electrochemical charging procedure in which the high current is initially applied to a certain voltage and once the target voltage is reached, the voltage is kept for a longer period of time to charge the cell more at lower current. $LiCoO_2$, layered structure, is one of the most commonly used active cathode material in commercial LIB cells. If one-mole amount of Li is extracted out of $LiCoO_2$, the capacity is 274 mAh g^{-1}. However,

when too much Li is extracted out of the layered structure, the crystal deforms into Co_2O_3 phase.[63] This phase does not have good vacant sites for Li to intercalate. In order to maintain the electrode integrity, the Co_2O_3 phase needs to be prevented.[64] One of the easiest ways to prevent this phase from forming is monitoring the voltage. Since Co_2O_3 phase begins at high voltage above 4.3 V vs. Li/Li^+, a common charging practice is to apply constant current and stop the constant current once the cell voltage reaches 4.3 V vs. Li/Li^+.[65-68] During the charging step, the active material is being delithiated. However, if the charging simply stops once the voltage reaches the target, due to polarization, Li distribution is not homogeneous. On the surface, the active particle is on the verge of undergoing the unwanted phase transformation. However, in the core, the Li concentration is higher. To maximize the amount of Li extraction without forming the unwanted phase on the surface, a constant voltage step is commonly added. After a high constant current charge, a constant voltage charge step maintains the thermodynamic stability of the active material, maximize the use of the active material, and shorten the charging time due to the initial high constant current step.

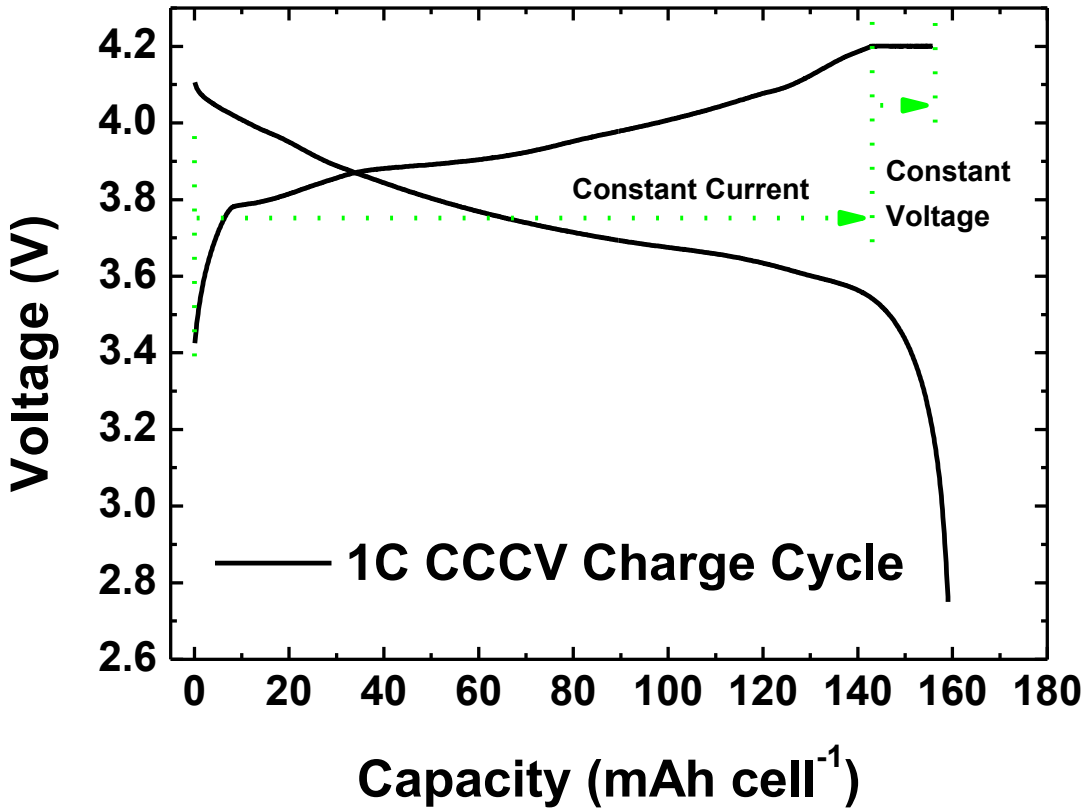

Figure 2.2. A voltage profile of an electrochemical cycling using the CCCV charge step.

2.2. Relaxation in conversion reaction

The understanding of the relaxation phenomenon in the conventional LIB cathode materials has allowed the scientists to leap forward in EESS performance. In order to progress further, unconventional LIB electrode materials need to be explored. Conversion type materials are attractive due to their high energy density.[47] Their bottleneck is the lack of rechargeability associated with the large crystal deformation. NiF_2 is one of the conversion materials. NiF_2 reacts with Li to form Ni and LiF. Upon lithiating NiF_2, NiF_2 diffraction pattern disappears and Ni and LiF diffraction patterns are observed (**Figure 2.3**).[69] During this reaction, the NiF_2 is dissociated into Ni^{2+} and F^- ions. The Ni^{2+} ion

reduces to form Ni metal and F^- reaction with Li^+ to form LiF. The problem with this reaction is that Ni metal does not generate the same sized particle as the pristine NiF_2 particle. When the pristine NiF_2 particle is microsized, the resulting Ni metal is nanosized.[69] Furthermore, in the prolonged cycles, the Ni metal particle size becomes even smaller. There are two drawbacks associated with this process. When the particle size of the active material is changing, the electrical connections in the electrode are compromised. Some active particles may completely lose the electrical connection, making them electrochemically inactive.[70, 71] The other drawback is the dissociation of Ni^{2+} ions. When the ions are dissociated, they are dissolved in the electrolyte. Some reduce into Ni metal on the surface of the electrode, but others diffuse away from the electrode surface. The ions diffused away are reduced because they do not receive electrons for the reduction reaction. They may even diffuse to the other electrode and precipitate there. In both cases, the Ni^{2+} ions are inactivated.

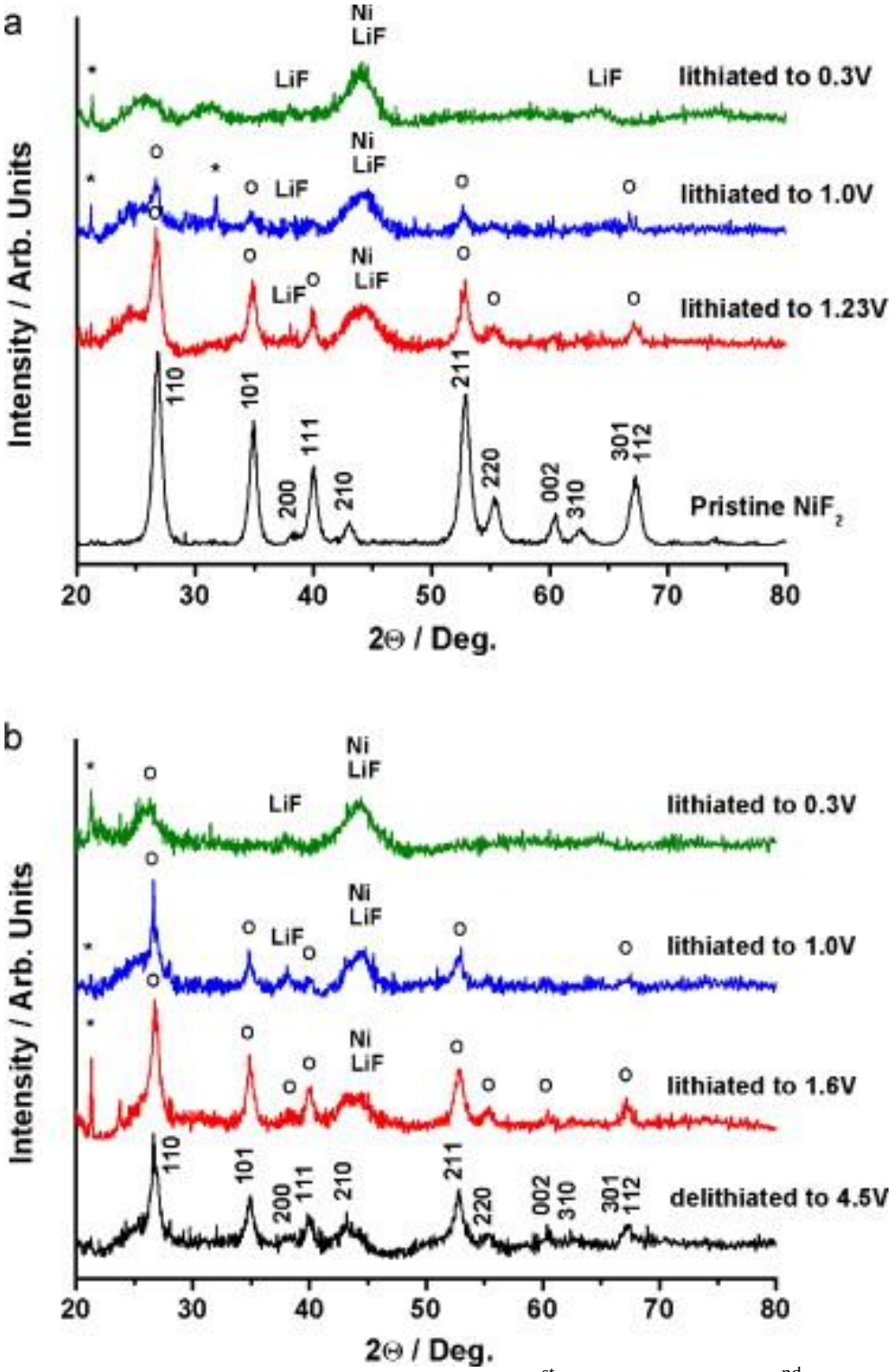

Figure 2.3. *Ex situ* XRD patterns for the (a) 1st lithiation and (b) 2nd lithiation in pristine NiF_2. (°) Reflections are assigned to NiF_2 and (*) marks impurities related to Li_2CO_3.[71]

Thermodynamically, NiF_2 reacting with Li should make Ni metal and LiF. Kinetically, when the NiF_2 electrode starts to reduce, Ni^{2+} dissolves into the electrolyte. Through relaxation, Ni^{2+} is reduced into Ni metal on the electrode surface. One of the keys for successful integrating conversion materials into the commercial LIB cells lies in the relaxation process. If Ni^{2+} dissolution is either prevented or better controlled, the loss of active material and the severe volume change would be alleviated. One of the methods to improve the electrochemical performance of NiF_2 is adding a functional additive. When NiO is added to the NiF_2 electrode, the electrochemical cycling performance is enhanced. This resulted in a stable Ni metal size throughout the prolonged cycle (**Figure 2.4**).[71] The comprehensive mechanism of the role of NiO in the NiF_2 electrode is still unclear, but further exploration of the relaxation phenomenon will pave the way for advancement in energy density of commercial LIBs.

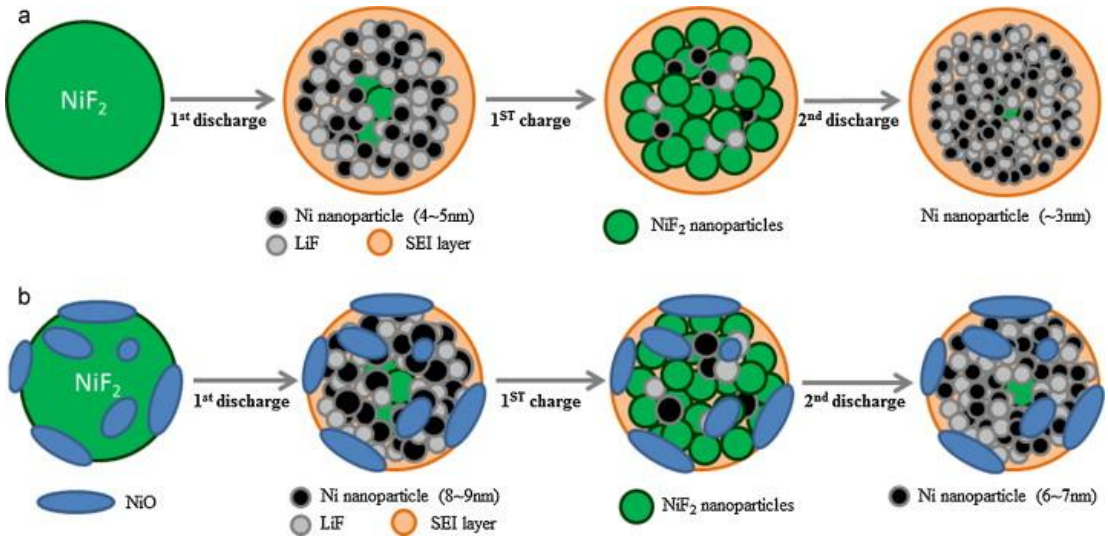

Figure 2.4. Schematics illustrating possible reaction mechanisms involving the change in Ni metal particle size variation for (a) pristine NiF_2 conversion electrode and (b) NiO-doped NiF_2 conversion electrode.[71]

Chapter 2, in part, is currently being prepared for submission for publication of the material “Manganese Based Oxides as Electrode Materials in Energy Storage Devices: A Review” The dissertation author was the primary investigator and author of this paper.

Chapter 3. Advanced characterization tools

Throughout the LIB research for this dissertation, by and large, there are three forms of characterization techniques involved: diffraction, imaging, and spectroscopy. In any form of characterization tools, there are sources, samples, and detectors. All three components of a tool are complimentary and variations of these components dictate the resulting analysis. It is imperative to decide proper tools to observe a respective phenomenon.

3.1. Diffraction

Incident light, electron, or neutron is generated from the source and interact with the sample. Diffraction detects bending of the incident source through the sample via the elastic interference. This utilizes the constructive and destructive wave-like behavior of the source going through the sample (**Figure 3.1**).[72] When a set of waves goes through slits, constructive or destructive interactions are observed depending on the position of the detector. The destructive interactions cause the reduction or absence of signal and constructive interactions generate signals. Depending on the atom arrangement or the crystal structure, the diffraction results demonstrate the crystal structure of the sample.[73]

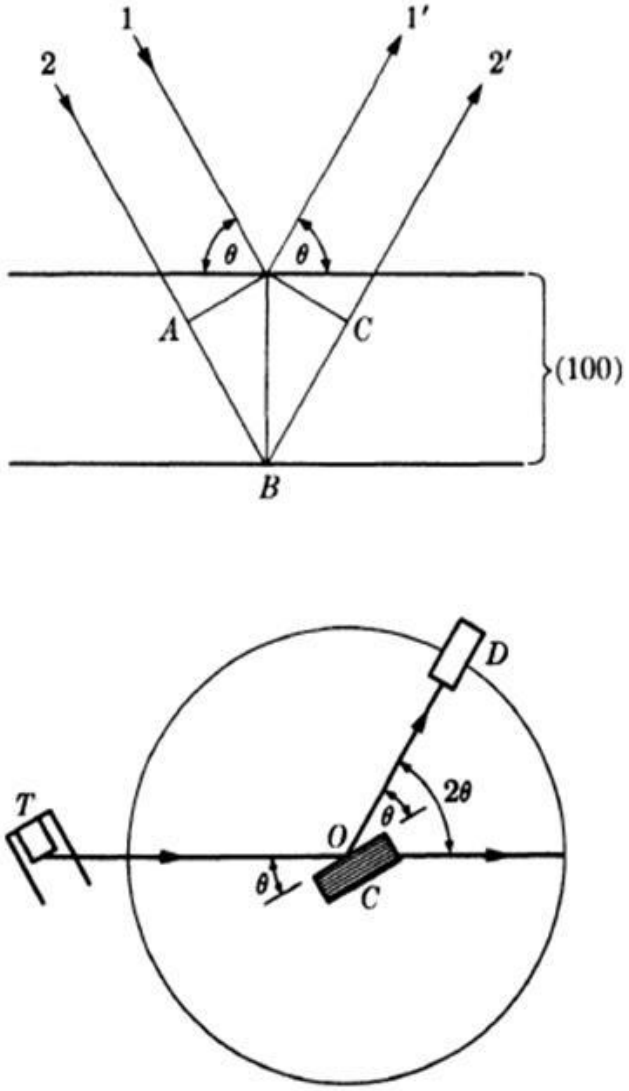

Figure 3.1. Top: Photon diffracting off of a 100 lattice. Bottom: The X-ray diffractometer. Where 2θ is the angle in which the photon diffracts out of a lattice plane.[72]

There can be two forms of samples in diffraction techniques. Single crystal samples generate a diffraction pattern of one crystal. The source goes through the sample projects diffraction pattern onto the 2D screen of detectors.[74] Spots of signals on the detectors represent the presence of lattice planes. The magnitude of the distance at the center of the detector screen to the signal signifies lattice distance. The closer distance

refers to the further lattice distance.[75] The angular location of the signal refers to the specific lattice of the crystal. These diffraction results obtained from the single crystal form of samples can be used to define the crystal structure whereas powder samples are mixtures of crystals. Instead of a 2D patterned signal, rings of signals are observed and the lattice distance can be distinguished without specific lattice. Thus, with the powdered sample, the exact crystal is harder to solve.[76, 77] Since 2D pattern does not exist in PXRD, one detector with a variable angle or an arc of detectors is adapted to measure the diffraction pattern rather than using a screen detector.

There are three sources for the diffraction characterization. A most commonly implemented X-ray diffraction (XRD) utilizes photons in the X-ray wavelength range. Single crystal X-ray diffraction (SCXRD) can solve the exact crystal structure and it needs single crystal samples of at least 100 μm sized particles.[78] Powder X-ray diffraction (PXRD) gives an idea of the crystal structure and it uses samples of any size above about 10 nm. Since most of the battery materials are a few micro-sized or less, the PXRD is the most suitable diffraction tool.[79] Another commonly utilized source of diffraction is an electron. Electron diffraction (ED) is an add-on tool for a transmission electron microscope (TEM).[80-82] Compared to photons, electrons interact with the sample significantly more due to a charge. Thus the sample thickness needs to be very thin (>100 nm) to obtain enough elastically interfered electrons. Single crystal electron diffraction is easy to obtain due to the thickness requirement, however figuring the crystal structure is not as easy because it is difficult to tilt the sample and obtain diffraction patterns in different angles. Neutron diffraction (ND) is another source, which utilizes neutrons but is not as frequently used. While X-ray interacts with the electron, the neutron interacts

with the nucleus. Hydrogen in a sample lacks electron due to its bonding environment.[83-85] Thus, XRD cannot be used to identify the hydrogen or proton arrangement. ND is the only form of diffraction that identifies the hydrogen arrangement. A downside of ND is its lack of interaction, thus requiring almost 10 g of electrode material sample, which is difficult to obtain in a research scale.

3.2. Imaging

Unlike diffraction techniques, X-ray and neutron sourced imaging techniques are still under development other than electron sourced imaging techniques. In terms of electrons as the source, sets of magnets are used to focus the source. The focused electrons interact with the sample in various ways. The electron source is focused into a coherent incident beam towards the sample (**Figure 3.2**). Upon interaction with the sample, the secondary electrons from the sample and incoherent elastic backscattered electrons are scattered out of the sample other than electron sourced imaging techniques. Scanning electron microscopy (SEM) techniques detect these electrons.[82, 86-89] On the other hand, if the sample is thin (<100 nm), there are forward scattering electrons going through the sample. Some electrons have no interaction as a direct beam coming through the sample. Other electrons with interaction are coherent elastic scattered electrons, incoherent inelastic scattered electrons, and incoherent elastic forward scattered electrons. The technique detecting these forward scattered electrons going through the thin sample is called TEM.[90, 91] TEM detects the electrons that are not transmitted but scattered in the forward direction.

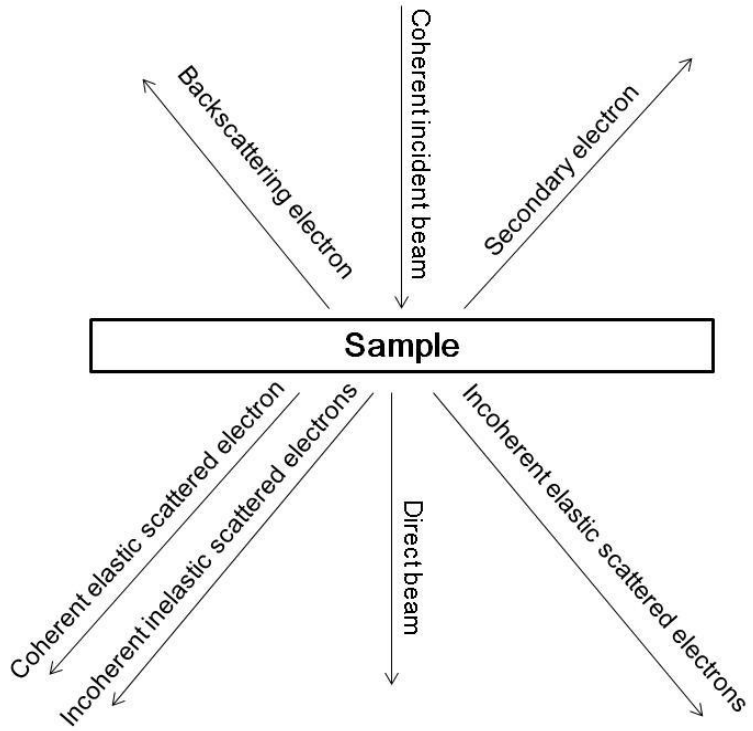

Figure 3.2. Coherent electron beam interactions with the sample.

Neutron sourced microscopy technique is underdeveloped because the interaction between the nucleus and the sample is scarce. However, it penetrates through a thick sample.[92] The penetration depth with the photon sourced microscopy techniques depends on the wavelength. The optical microscope uses photons in the optical range and these techniques are well developed.[93-96] Due to low energy of the photon, only surface properties are observed. X-ray sourced microscopy techniques, on the other hand, uses X-ray ranged photons.[97, 98] For X-rays similar to diffraction, the source mainly uses a monochromator. Since the X-ray has higher energy than an optical photon, it penetrates deeper.

3.3. Spectroscopy

An atom is composed of a nucleus and electrons. The electron density is

determined around a nucleus in shells of energy levels (**Figure 3.3**). More stable energy level shells are located closer to the nucleus. The electrons in the outer most shell is least stable and these are valence electrons; The electrons in the inner shells are called core-shell electrons. In spectroscopy, an incident source inelastically interacts with the electron of the sample.[99-101] Depending on the energy state of the incident source, the energy state of the electron, the detector, and extra information can be obtained. More stable electrons require higher energy to excite compared to the electrons in higher energy levels. When a core-shell electron is excited by the incident source, the core-shell electron gets ejected out to the vacuum. All electrons have their respective signature excitation energy depending on the number of protons and electrons in the atom. Spectroscopy is used to identify elements, their oxidation states, and/or their chemical environment.[101]

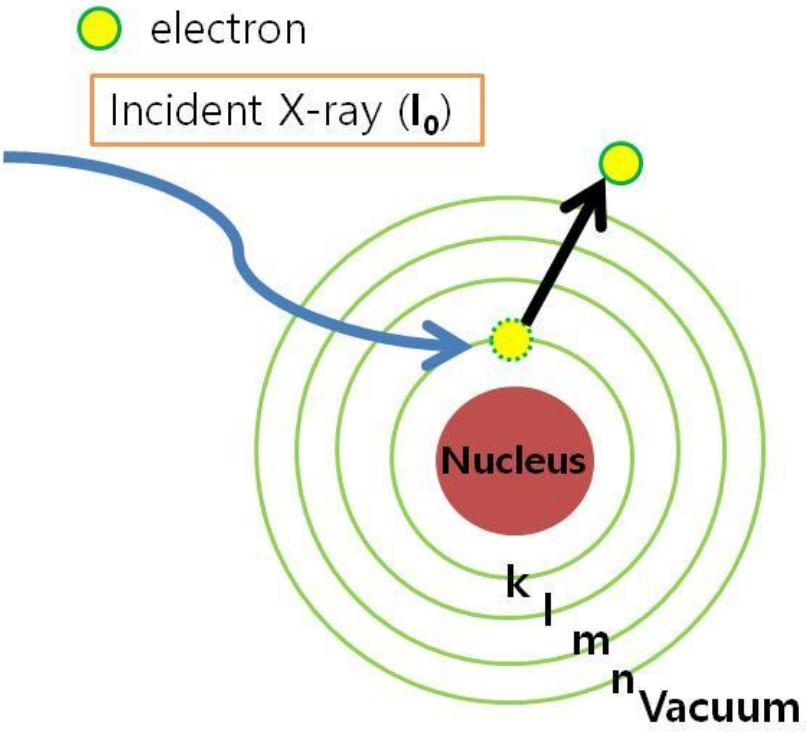

Figure 3.3. A Nucleus with electron shells bombarded with an incident X-ray.

3.3.1. X-ray absorption spectroscopy

X-ray absorption spectroscopy (XAS) is a spectroscopy technique, which utilizes a tunable X-ray beam as a source. To be able to tune the X-ray and provide a high flux of photons, synchrotron facilities are built to supply the radiation sources.[102] The most common elements to use XAS to detect and characterize is the first row transition metals because these transition metals have their K shell energy within the hard X-ray range. The hard X-ray range is about 2000 - 10,000 eV. Above 10,000 eV photons are closer to the gamma ray that has more complicated interactions.[103] Below 2000 eV photons are soft X-rays, which is less common than the hard XAS owing to more experimental constraints.[104] With the soft XAS, the sample thickness has to be small to obtain the transmission data because the X-ray has significantly lower energy than the hard X-ray.[105] If the sample is too thick, fluorescence can be detected for the similar effect, but

the scattering fluorescence has low intensity and only provides the surface information. X-ray photoelectron spectroscopy (XPS) is more developed and a suitable technique that does not require synchrotron radiation and delivers similar information. One of the main advantages of soft XAS over XPS is the fact that the samples do not have to be in a vacuum for soft XAS.

For the XAS, the source is supplied from the synchrotron radiation. The energy of source is tuned using a double slit monochromator via the diffraction phenomenon (**Figure 3.4**). When the energy of the source reaches the excitation energy of the core-shell electron, sudden increase in absorption is observed during the source tuning.[99-101] Due to the absorption, the amount of X-ray transmitted through the sample decreases at a certain energy level. The energy of this sudden absorption is called the edge. The edge signifies the energy of the excited electron. As mentioned above, this edge is specific to an element and its oxidation state.

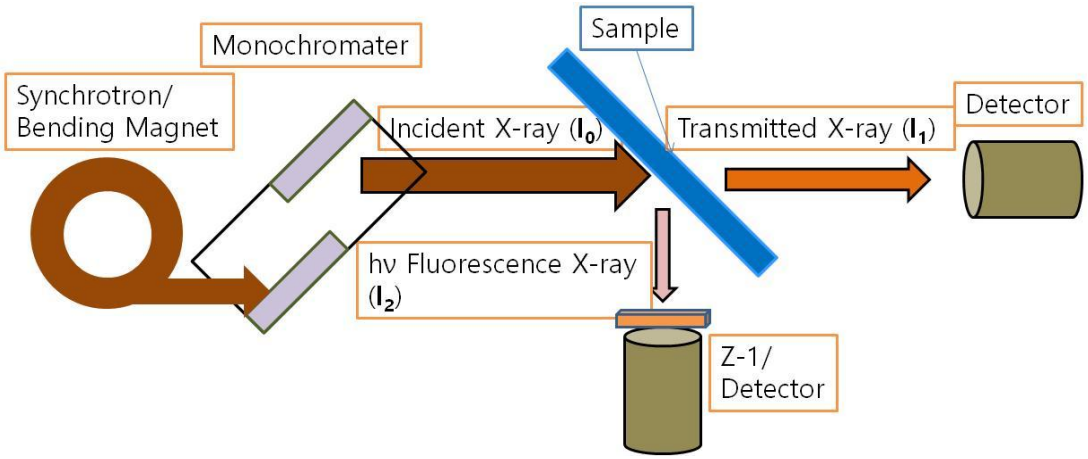

Figure 3.4. A simplified schematic diagram of a bending magnet XAS facility.

Upon the electron excitation, an electron hole in the core-shell is generated as

well as an ejected electron in the vacuum out of the valence shell. Due to the hole, an electron from a higher energy state enters the core-shell and fills that hole.[99-101] Since the core-shell electrons are at lower energy state, the energy difference between the core-shell and the electron in the vacuum is scattered as a form of a photon. This scattering photon is called the fluorescence (**Figure 3.5**). For XAS, the photon energy is in the X-ray range.[106]

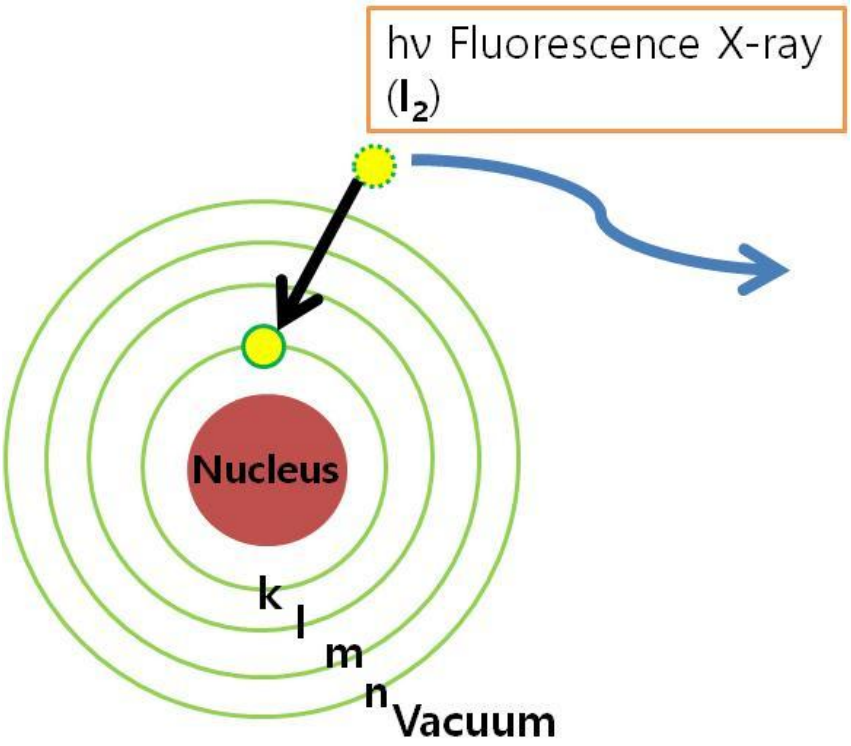

Figure 3.5. An atom with a core-shell hole filled with an electron from the vacuum while emitting a fluorescence X-ray.

When the fluorescence X-ray is emitted due to the relaxation of the hole and the electron of the vacuum, the fluorescence interacts with the surrounding atoms. The interactions cause constructive and destructive interactions among the fluorescence X-ray (**Figure 3.6**). Thus, depending on the scattering factor of the surrounding atoms and the

radial location of the surrounding atoms with respect to the center excited atom, the intensity of the fluorescence out of the sample varies.[106] In addition, due to the fact that the source has a tunable energy, as the energy of the incident X-ray increases, the interaction between the incident X-ray and the fluorescence X-ray varies as well.

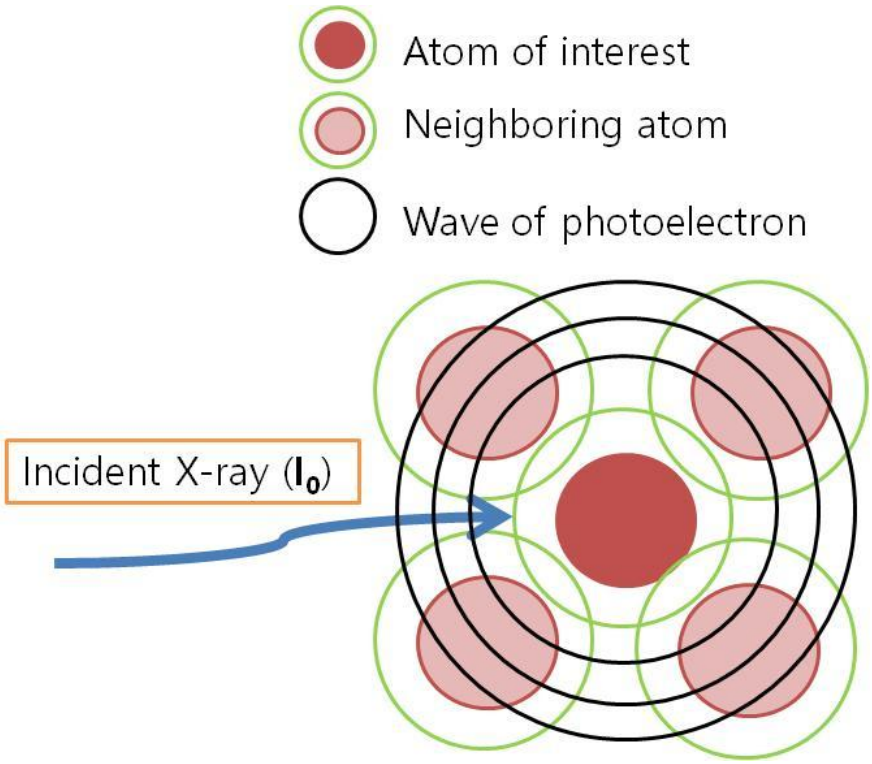

Figure 3.6. The wave of photoelectron and the fluorescence from the center atom interacting with the surrounding atoms.

At the moment where the edge is observed, a sudden spike of a signal is observed. Near this edge, the set of data in this region is called X-ray absorption near edge spectrum (XANES) (**Figure 3.7**). The energy of the absorption edge and the immediate fluctuation of a signal caused by the photoelectron interaction between the center atom and surrounding atoms are included in the XANES.[107] Typically, this region is qualitatively compared among samples because quantitatively simulating the

photoelectron interaction among atoms requires first principles calculations with high computing power. The set of data after the XANES region to the next several hundreds of eV is called extended X-ray absorption fine structure (EXAFS) region. This region mainly contains the fluctuations from the photoelectron interaction. Because EXAFS is mostly governed by the Hook's law, this region is quantitatively analyzed.

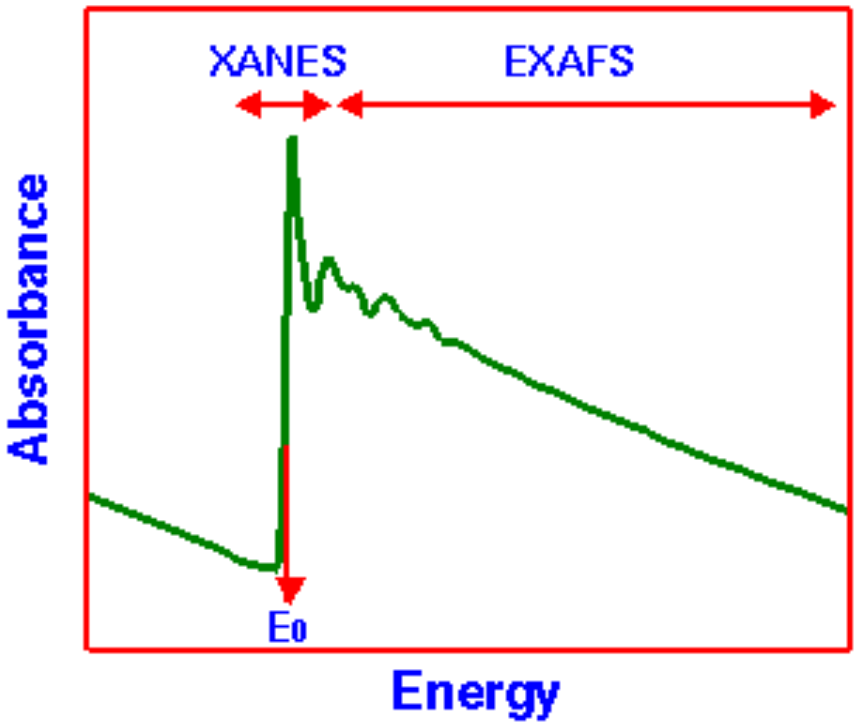

Figure 3.7. A typical XAS spectrum.[108]

From the raw data, the spectrum is removed from the background and normalized (**Figure 3.8**). Performing EXAFS analysis is more involved. However, it can be quantitatively analyzed more easily. The below equation dominates the EXAFS signal:[109]

$$\chi(k) = \sum_i \chi_i(k)$$ **Equation 3.1.**

with

$$\chi_i(k) = \left(\frac{(N_i S_0^2) F_i(k)}{kR_i^2} \sin\left(2kR_i + \varphi_i(k)\right) \exp(-2\sigma_i^2 k^2) \exp\left(-2R_i/\lambda(k)\right)\right)$$ **Equation 3.2.**

and

$$R_i = R_0 + \Delta R$$ **Equation 3.3.**

where, $F_i(k)$ is effective scattering amplitude, $\varphi_i(k)$ is effective scattering phase shift, $\lambda(k)$ is mean free path, R_0 is initial path length, N_i is a degeneracy of path, S_0^2 is a passive electron reduction factor, σ_i^2 is mean squared displacement, and ΔR is the change in half-path length. First, upon background removal, an x-axis is rescaled into k scale. The rescale is as follows:[109]

$$k^2 = \frac{2 m_e (E - E_0)}{\hbar^2}$$ **Equation 3.4.**

where m_e is the mass of the electron, E_0 is the threshold energy, and $\hbar^2$ is the Planck's constant. Because the EXAFS signal is inherently sinusoidal, to analyze the data qualitatively as well as quantitatively, the EXAFS signal is Fourier transformed. Upon Fourier transformation, the x-axis represents radial path length from the central atom. The signal observed in the Fourier transformed EXAFS represents the neighboring atom. Depending on the scattering pathway, various signals can be found.

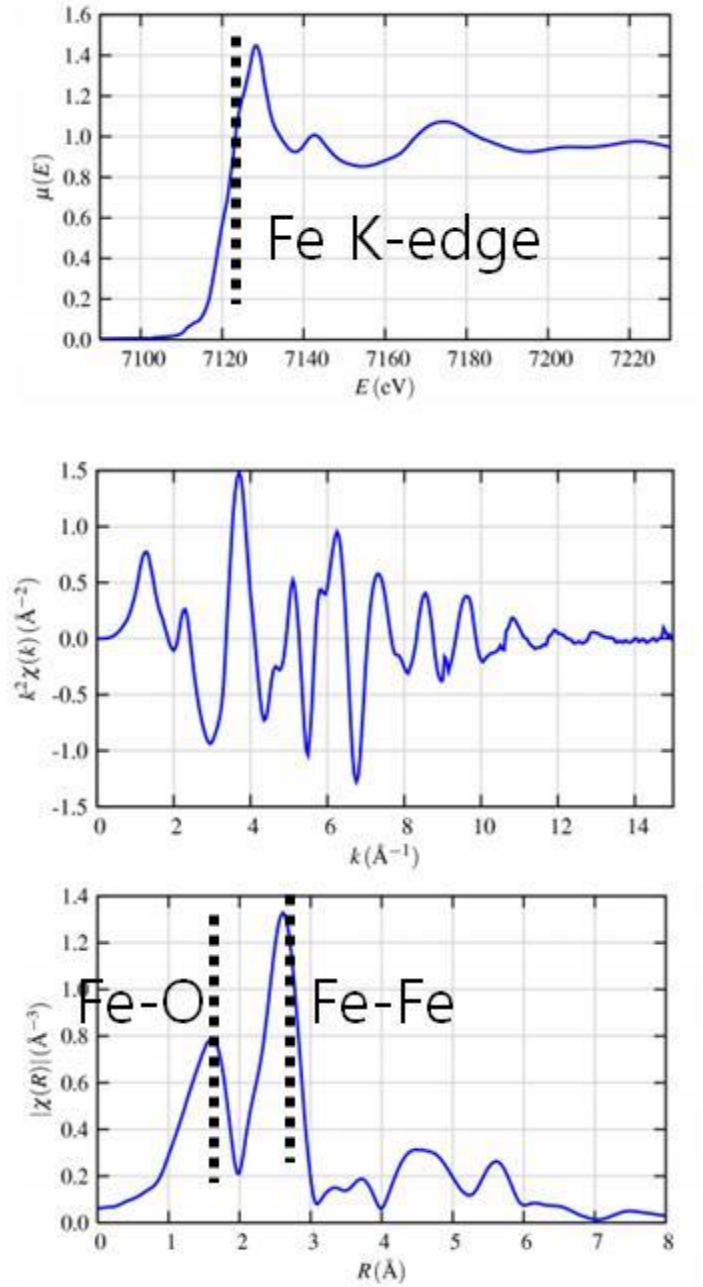

Figure 3.8. Top: XANES after background removal and normalization. Middle: k weighed EXAFS region. Bottom: Fourier transformed EXAFS region.

Most common detector utilized in the XAS measurement is the ion detector. The ion detector chamber is filled with a designated amount of selective gas molecules. Detector sensitivity is controlled by the gas filled chamber. When the X-ray interacts with

the gas molecules in the chamber, the gas molecule becomes ionized and gets collected by the electrodes placed inside the chamber. The amount of electron collected due to this process is counted from the detector and represented as the signal. A transmission mode is the most popular method to detect the XAS signal. This is a mode where the detector is placed directly behind the sample. This detector detects the amount of X-ray transmitting through the sample. The data are plotted using the following equation:

$$\text{Intensity} = \log\frac{I_1}{I_0} \quad \textbf{Equation 3.5.}$$

where, I_0 is the amount of incident X-ray and I_1 is the amount of transmitted X-ray through the sample. Another popular way to measure XAS is a fluorescence mode. Instead of the detector behind the sample, the sample is placed perpendicular to the incident X-ray and the sample is tilted 45° to maximize the signal sent to the fluorescence detector. While the fluorescence mode adopts the same ion detector as the transmission mode, a Z-1 filter is used to avoid the fluorescence signal from saturating the detector. Other modes of detection are called electron yield modes. Total electron yield mode and partial electron yield mode both detect photoelectron coming out of the sample as a form of current. Unlike the bulk transmission and fluorescence modes, these electron yield modes are surface sensitive due to the electron's mean free pathway.[110, 111] The difference between the two electron yield modes is that the total electron counts any electron coming out of the sample whereas the partial electron only counts the photoelectrons of a certain energy. Since the partial electron yield mode is more selective, this mode is more surface sensitive.

3.3.2. X-ray photoelectron spectroscopy

XPS is also an X-ray spectroscopy technique similar to XAS. Unlike the XAS, where the spectrum is measured in the ambient environment, XPS is obtained when the sample is in the ultra-high vacuum (UHV) environment.[112-115] This difference derives from the fact that the XPS measures the photoelectrons coming out of the sample. Because the photoelectrons have a short mean free path, the sample is under UHV to maximize the travel distance. The detector uses an energy analyzer to identify the energy of the photoelectron to classify the chemical state of the sample. Similar to the electron yield modes of XAS, XPS is surface sensitive experiments but due to the detector further away, the detection is most surface sensitive.[112-115]

Instead of a tunable X-ray source for XAS, XPS's source has constant energy. The detectors in XAS often do not discriminate the energy of the X-ray or photoelectron of detection. In XPS, however, the detected photoelectron is usually energy analyzed and the detector in XPS detects the kinetic energy of the photoelectron. However, the kinetic energy is not as meaningful as the binding energy of the photoelectron. The equation to express the binding energy is as follows:[112-115]

$$E_{binding} = E_{photon} - (E_{kinetic} + \phi)$$ **Equation 3.6.**

where, $E_{binding}$ is the binding energy of the photoelectron, E_{photon} is the energy of the source, $E_{kinetic}$ is the kinetic energy of the photoelectron, and ϕ is the adjustable instrumental correction. Most of the XPS instruments internally operate the above equation to present the binding energy.[112-115]

One of the issues with measuring the photoelectron is the presence of Auger effect. The Auger effect is a phenomenon in which the inner-shell electron is filling the core-shell hole and ejecting another inner-shell electron as a photoelectron. Since the

XPS only measures the kinetic energy, the instrument cannot distinguish the Auger electrons from the core-shell electrons. Sometimes, these Auger electrons is convoluted with the core-shell electron signals. In this case, the Auger electron is moved by utilizing a different X-ray source. Al k_α (1486.7 eV) is the most common source of XPS. When the Auger complicates the spectra analysis, Mg k_α (1253.7 eV) is used as the alternative X-ray source occasionally.[112-115] Since the alternative has lower energy, the Auger appears in lower binding energy. As the core-shell photoelectron is dependent on the energy of the X-ray source, the Auger electron is independent of the X-ray source.

3.3.3. Electron energy loss spectroscopy

Electron energy loss spectroscopy (EELS) is an electron based spectroscopy technique. It is an add-on for the TEM instrument especially for the scanning transmission electron microscope (STEM).[116-120] STEM focuses the electron source to a small spot on the sample and scans the sample to obtain the image rather than obtaining an image from a wide electron focus. STEM allows us to focus on a certain spot and collect localized spectral information. Similar to XPS, the electron source has a constant energy and the transmitted electron is energy analyzed. However, Auger effect is less since the detecting electron is closer to the transmission mode XAS, unlike XPS. The transmitted electron is detected rather than the photoelectron emitted from the sample.

3.4. *Ex-situ, in-situ,* and *operando experiment*

Aside from choosing the characterization tools, the way to set up the characterization is just as important. Especially for studying a component of a device, a simple pristine, as-synthesized, or as-prepared characterization is not enough to fully comprehend the relaxation phenomenon.[121, 122] The characterization needs to be

conducted with respect to the device operation.[123] The material stability or the deformation from the operation can be assessed this way. Especially in energy storage devices, the redox reaction is pushed to the boundary of instability. After the device operation, oxidation state, and/or crystal structure are altered. *Ex situ* setting is where the device is assembled and disassembled after the device operation, which is a most benign setting for the instrument. Regardless of the device configuration, the sample is prepared in the most suitable way for the instrumental measurement. However, this setting may not perfectly simulate the material inside the device as the energy storage device has electrode materials immersed in the electrolyte.[122] Essentially, *ex situ* setting takes the sample out of its operation environment to meet the instrumental requirement. *In situ,* on the other hand, alters both the device and the instrument to meet halfway.[124-127] The material is kept in the operation environment to ensure that the collected data represent the material after the device operation properly. Lastly, *operando* setting is similar to *in situ* but the instrumental measurement is conducted during the device operation.[122] There is a complication such as a device performance decay from applying two different perturbations. However, *operando* ensures that the data obtained has the kinetically stable product. The other two do not have the kinetically stable products due to the time between the device operation and the sample measurement.

Chapter 4. MIL-101(Fe) as a lithium-ion battery electrode material_ a relaxation and intercalation mechanism during lithium insertion

4.1. Introduction

Rechargeable Li-ion batteries are essential for the development of smartphones, laptop computers, and many other technologies including grid energy storage.[19] The materials used in commercial Li-ion batteries are far too expensive and energy intensive for large-scale grid storage applications.[19-22] For example, layered oxide cathode materials are costly because they require a high temperature synthesis process and contain expensive transition metals like Co.[23-26] In order to reduce the cost of Li-ion batteries for grid scale applications, metal-organic framework (MOF) cathode materials could be utilized. MOF materials offer several advantages with respect to other porous materials because of their flexible synthetic routes, low temperature synthesis, and comparatively inexpensive precursor materials.[27] MIL-101(Fe) was chosen as an electrode candidate. The MIL-101(Fe) SBU is composed of a carboxylate-bridged, oxo-centered, trinuclear Fe^{3+} complex (**Figure 4.1.a**). This particular SBU complex is a well-known motif in inorganic chemistry, and its electron density distribution, magnetic, and electrochemical properties have been previously reported.[128-130] The theoretical capacity of the material with one lithium insertion per Fe atom is 107.74 mAh g^{-1}.

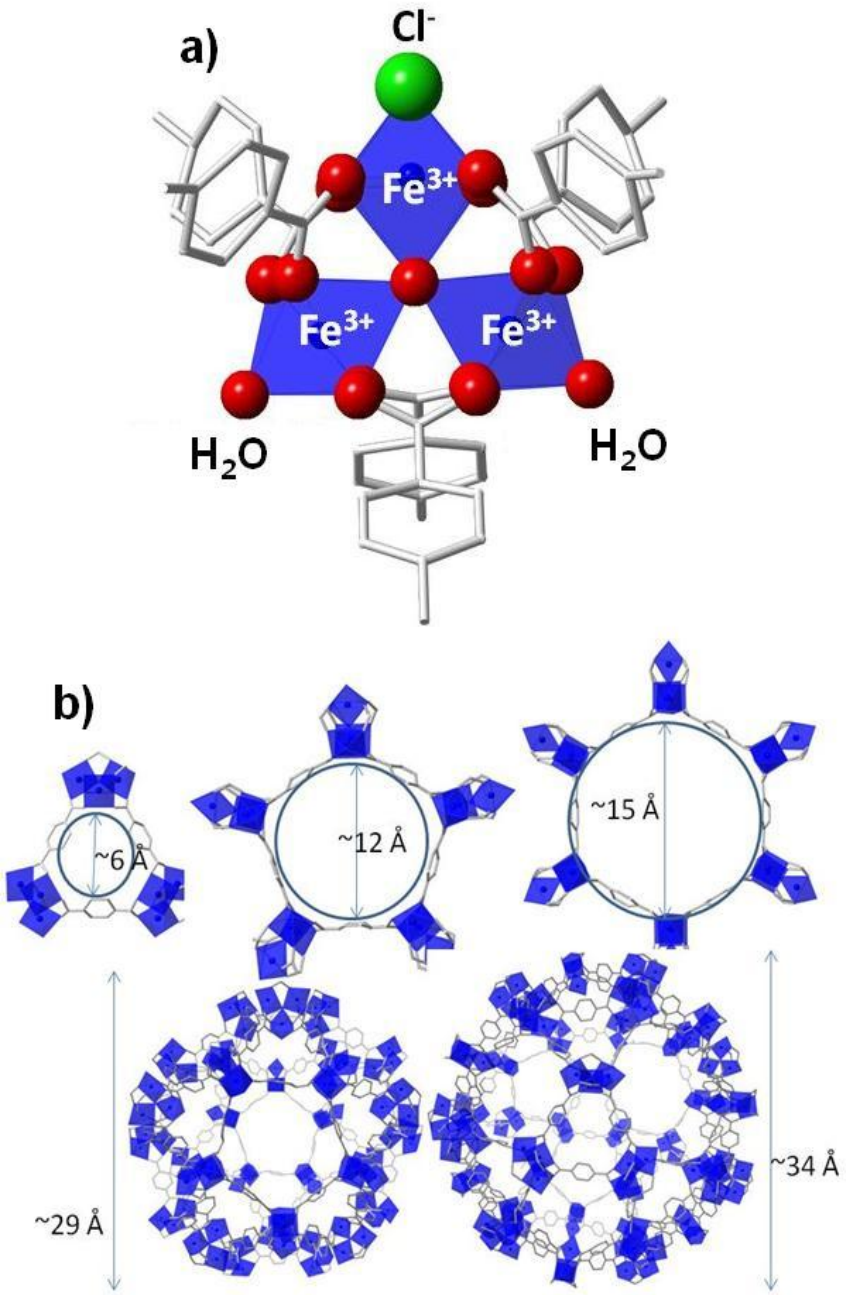

Figure 4.1. Structure of MIL-101(Fe). a) The SBU (blue, Fe; red, O; stick, C; green, Cl; H is omitted for clarity). b) The windows and pores of MIL-101(Fe) with Cl and O atoms omitted for clarity.

Using PXRD and XAS, we find that MIL-101(Fe) undergoes structurally reversible intercalation reactions, with the Fe^{3+}/Fe^{2+} redox couple being

electrochemically active. However, in long term cycling, we observe an exponential decay in reversible lithium insertion capacity. To evaluate the irreversibility associated with MIL-101(Fe), *ex-situ* and *in-operando* XAS experiments are conducted. The two types of XAS results reveal Fe^{2+} relaxation back to the pristine Fe^{3+}. To rationalize this phenomenon, electronic structure calculations were conducted to model the side reactions responsible for the lack of reversibility. We propose that the observed Fe^{2+} to Fe^{3+} relaxation promotes irreversible accumulation of lithium in MIL-101(Fe), which leads to the poor capacity retention.

4.2. Experimental and Computational Methods

MIL-101(Fe) preparation

MIL-101(Fe) was prepared by using a modified procedure.[131] Equimolar (0.346 mmol) $FeCl_3 \cdot 5H_2O$ (Sigma Aldrich) and H_2bdc (Sigma Aldrich) were dissolved in 15 mL *N*,*N*-dimethyl formamide (DMF, Alfa Aesar). This solution was then heated to 150 ℃ for 15 min via microwave irradiation (CEM discover S-class microwave reactor). After cooling to room temperature, the particles were filtered and washed with 20 mL of DMF and methanol.[131] After washing, the product was dried to evacuate water molecules trapped in the pores. Water can deteriorate the quality of battery electrolyte. Drying was performed at 150 ℃ under vacuum for 3 h. After the drying process, the product was transferred into a dry glove box (MBraun) filled with high purity Argon (Ar) without exposure to air (**Figure 4.2**). The MIL-101(Fe) H_2O sample is the MIL-101(Fe) electrode exposed in air. The MIL-101(Fe) DMC sample is the MIL-101(Fe) electrode soaked in DMC. The magnetic susceptibility is zero field cooled and temperature sweep was done

in 2 K/min rate and in 5000 Oe. A shift in the magnetic susceptibility is observed and signifies the change in coordination environment of Fe from H_2O to DMC.

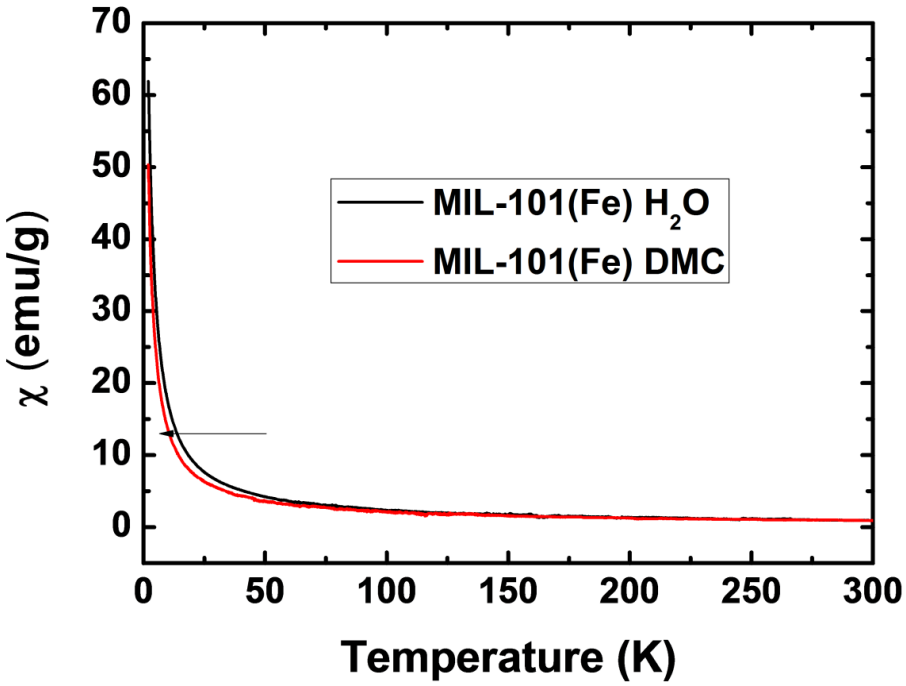

Figure 4.2. Magnetic susceptibility plot of MIL-101(Fe) with H_2O vs. DMC.

Electrochemical testing

Unless otherwise noted, electrochemical cells were constructed using Swagelok cells with 0.5 inches diameter stainless steel rods as the current collector. Following a previously outlined procedure,[132] assembly was conducted in an Ar filled glove box with Li metal foil (Sigma Aldrich) used as the counter electrode, Whatman GF/D borosilicate glass fiber sheets used as the separators, and 1 M $LiPF_6$ in 1:1 (by weight) ethylene carbonate:dimethyl carbonate (EC:DMC) (BASF, 1.6 PPM of water) used as the electrolyte. The working electrodes were prepared by ball milling (Retsch PM 100)

carbon black (Super-P (SP), Timcal) and MIL-101(Fe) powders in a weight ratio of 3:7, respectively. Specifically, 100 mg total of the powder was milled at 100 rpm for 10 min in a 50 mL agate (Retsch Part # 01.462.0139) jar with a ball to powder weight ratio of 120:1, respectively. Cells were cycled under galvanostatic conditions at room temperature using an Arbin BT 2100 battery tester between the voltages of 2.0 and 3.5 V (versus Li^+/Li) at rates of C/60, C/40, C/20, and C/10. Theoretical capacity was calculated assuming the complete one electron redox reaction of the Fe^{3+}/Fe^{2+} redox couple.

Powder X-ray Diffraction (PXRD)

Cycled MIL-101(Fe) material used in the PXRD was prepared at a rate of C/40. After cycling was complete, the electrode was recovered from the disassembled Swagelok cell and washed with dimethyl carbonate (DMC). Upon drying in Ar environment, the sample was placed inside a kapton capillary tube and sealed with epoxy glue. Ex situ synchrotron powder diffraction experiments were performed using the monochromated X-rays (0.6661 Å, 300 μm diameter beam size) available at the 1-BM beamline of the Advance Photon (Argonne National Laboratory). The samples were sealed in 0.9 mm diameter polyimide capillaries. Diffraction data were collected using a Perkin-Elmer flat panel area detector (XRD 1621 CN3-EHS) over the d-spacing range 1-50 Å. The raw images were processed within Fit-2D,[20, 21] refining the sample-to-detector distance and tilt of the detector relative to the beam based on the data obtained for a LaB_6 standard.

X-ray Absorption Spectroscopy

In-operando XAS was performed at the Stanford Synchrotron Radiation Lightsource (SSRL) using the fluorescence mode of beamline 4-1. The *in-operando* battery was assembled using a custom designed coin cell with Cirlex film (Fralock) as the X-ray transparent window and cycled at a rate of C/20 during *in-operando* XAS measurements. Transmission mode *ex-situ* XAS experiments were performed at APS 9-BM. Electrode samples were prepared as outlined above for the PXRD samples. After drying, the sample was sealed between two layers of Kapton tape (KaptonTape.com). For both experiments, the XANES (X-ray Absorption Near Edge Spectroscopy) region normalization and the EXAFS (Extended X-ray Absorption Fine Structure) region Fourier transformation were done using Athena software.[22] The extracted EXAFS signals $\chi(k)$, were weighted by k^2 to emphasize the high-energy oscillations and the signals were then Fourier-transformed in a k-range of 2.0 ~ 10.0 $Å^{-1}$ (*in-operando*) or 2.0 ~ 9.0 $Å^{-1}$ (*ex-situ*). During the Fourier-transform, a Hanning termination window with a dk value of 1 was utilized to obtain the magnitude plots of the EXAFS spectra in an R-space (Å).

Computational methods

All calculations were performed with Gaussian 09 (Rev C.01) using the hybrid B3LYP functional with a 10^{-8} convergence criterion for the elements of the density matrix.[23] The fully optimized contracted triple-ζ all-electron Gaussian basis set developed by Ahlrichs and co-workers was employed for all atoms, with the addition of polarization functions for Fe.[133] Vibrational analysis was performed for all the optimized structures, and the corresponding harmonic frequencies were used to estimate the thermodynamic quantities. The MIL-101(Fe) secondary building unit was properly modeled for computational efficiency (Figure 4.3). The different spin topologies were modeled using

the fragments option, which allows the definition of specific electronic structures for each metal center. The broken-symmetry solutions were spin-projected by using **Equation 4.1**, were J is the exchange coupling constant, E_{BS} is the energy of the broken symmetry state, E_{HS} is the energy of the highest spin state, $< S^2 >_{BS}$ is the spin expected value of the total spin for the broken symmetry, and $< S^2 >_{HS}$ is the spin expected value of the total spin for the highest spin state,

$$J = \frac{2(E_{BS} - E_{HS})}{\langle S^2 \rangle_{HS} - \langle S^2 \rangle_{BS}} \qquad \textbf{Equation 4.1.}$$

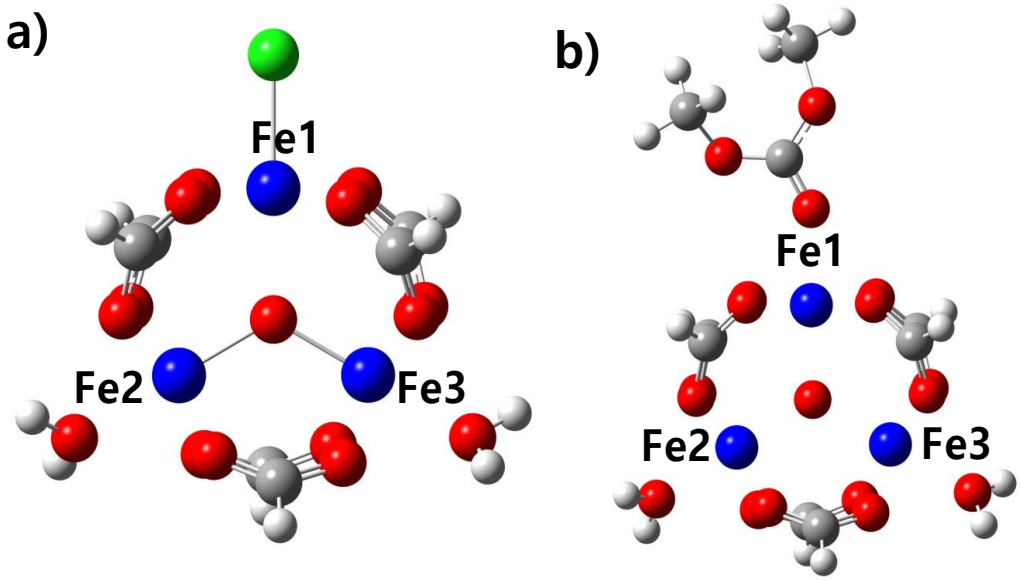

Figure 4.3. a) Trimer and b) TrimerDMC model used for the Gibbs free energy calculation. There are three Fe per model but there are only two different Fe environments as Fe2 and Fe3 are degenerate. Iron, oxygen, carbon, and hydrogen atoms are colored blue, red, grey, and white, respectively.

4.3. Results

Figure 4.4 presents the electrochemical performance of MIL-101(Fe) electrodes versus Li counter electrodes. Upon initial lithiation (**Figure 4.4**), it was found that MIL-101(Fe) accommodates 0.62 Li/Fe. Compared to previous reports, this value is similar to that of MIL-53(Fe) (~0.62 Li/Fe) and higher than that of MIL-68(Fe) (~0.35 Li/Fe). However, MIL-101(Fe) achieves this value at a higher voltage cutoff of 2.0 V (1.5 V cutoff for MIL-53(Fe) and MIL-68(Fe)). The initial Coulombic efficiency for MIL-101(Fe) is 79%, which is lower than the value previously reported for MIL-53(Fe) (~97%) but close to that measured for MIL-68(Fe) (~79%). Due to this irreversibility, MIL-101(Fe) exhibits poor capacity retention and accommodates only 0.37 Li/Fe by the 5th cycle.

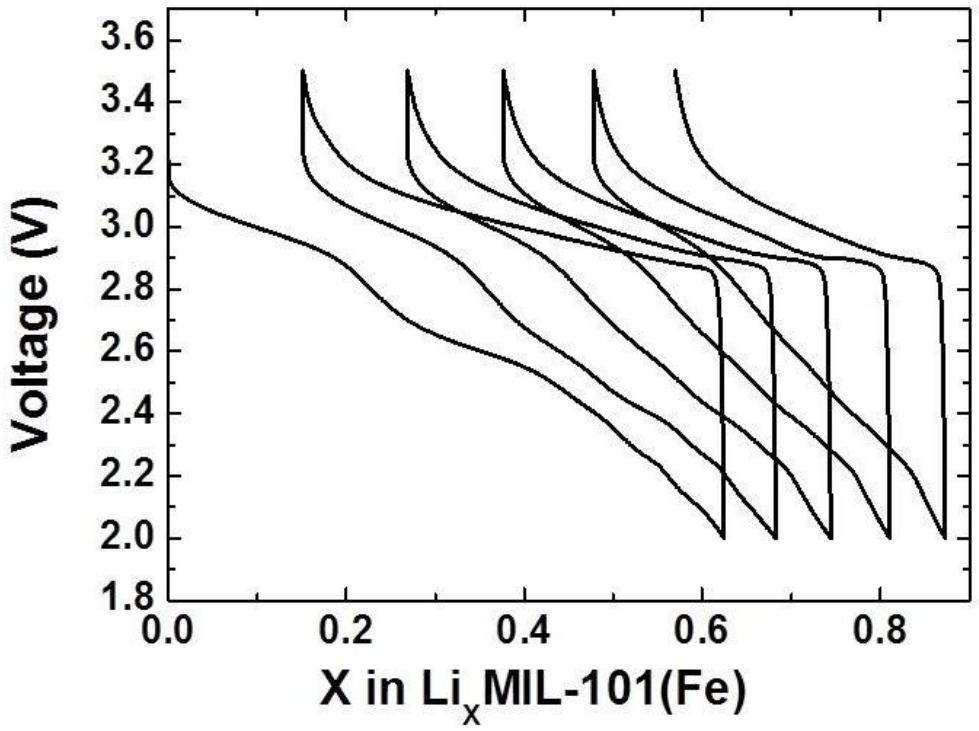

Figure 4.4. Results of galvanostatically cycling MIL-101(Fe) electrodes versus a Li counter electrode. First five voltage profiles at a rate of C/40.

To characterize the electrochemistry of MIL-101(Fe), we studied the differential capacity (dQ/dV) of the first 5 cycles (**Figure 4.5**). During the first cycle, we observed five distinct reduction peaks at 2.99, 2.59, 2.42, 2.27, and 2.13 V as well as two distinct oxidation peaks at 2.87 and 3.00 V. Multiple peaks are expected because MIL-101(Fe) has a complex SBU structure with several different Li insertion sites. A previous computational study found that MIL-53(Fe) has at least two distinct sites available for Li insertion.[25] A set of *ex-situ* XAS data suggests that at least two different reactions occurred upon lithiation of MIL-101(Fe) (**Figure 4.6 and Figure 4.7**). Exact assignment of redox peaks to particular lithiation sites is best left to computational studies beyond the scope of this work. In the subsequent cycles, the 2.42 V reduction peak and the 2.87 V oxidation peak increased in intensity while all other peaks reduced in intensity. With extended cycling, it was observed that all oxidation and reduction peaks decreased in intensity (**Figure 4.8**). It is noted that the 2.99 V and 2.59 V reductive peaks fade at much different rates. A different rate of degradation indicates that the observed irreversibility MIL-101(Fe) may be associated with a particular Li insertion site.

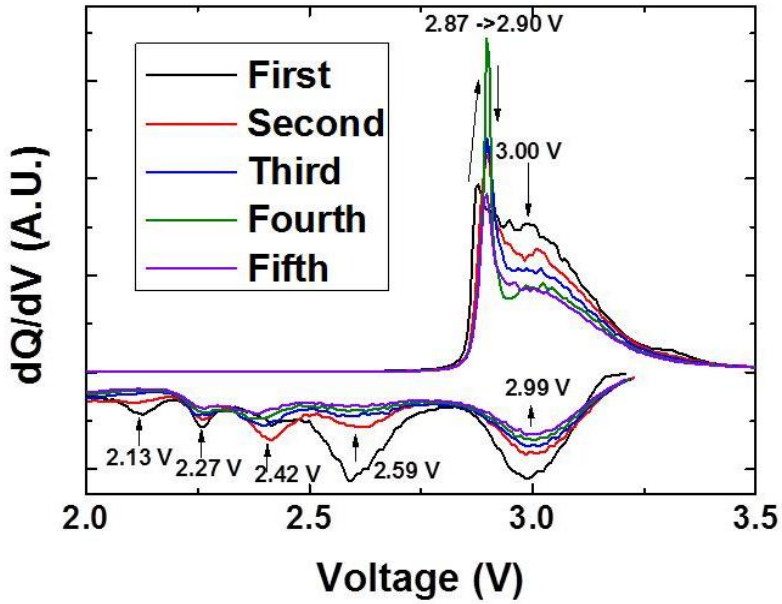

Figure 4.5. Results of galvanostatically cycling MIL-101(Fe) electrodes versus a Li counter electrode. Differential capacity (dQ/dV) of the first 5 cycles at a rate of C/40.

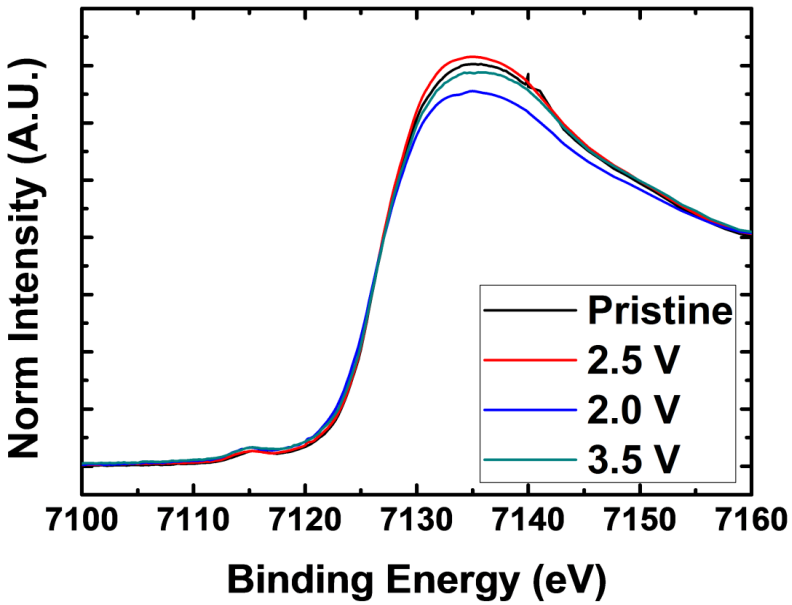

Figure 4.6. XANES region of the MIL-101(Fe)'s ex-situ XAS results at pristine state, lithiation to 2.5 V, lithiation to 2.0 V, and delithiation to 3.5 V.

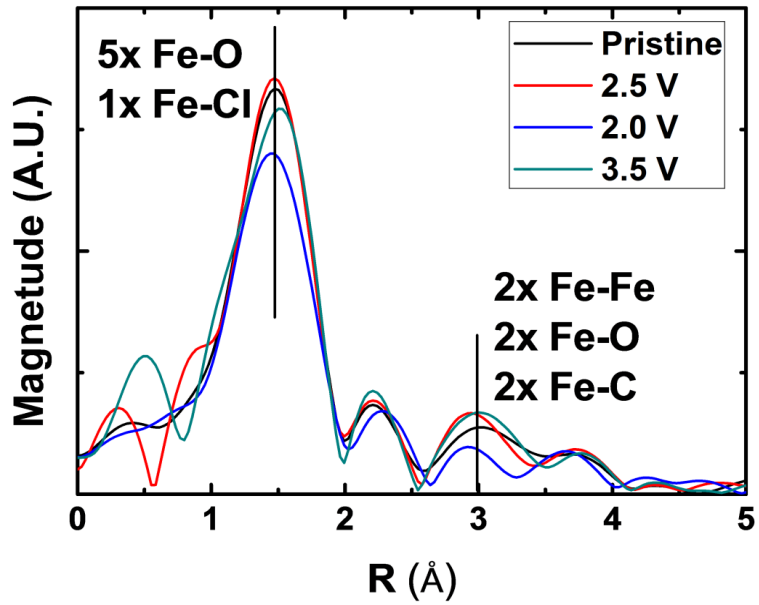

Figure 4.7. Fourier transformed EXAFS region of the MIL-101(Fe)'s ex-situ XAS results at pristine state, lithiation to 2.5 V, lithiation to 2.0 V, and delithiation to 3.5 V.

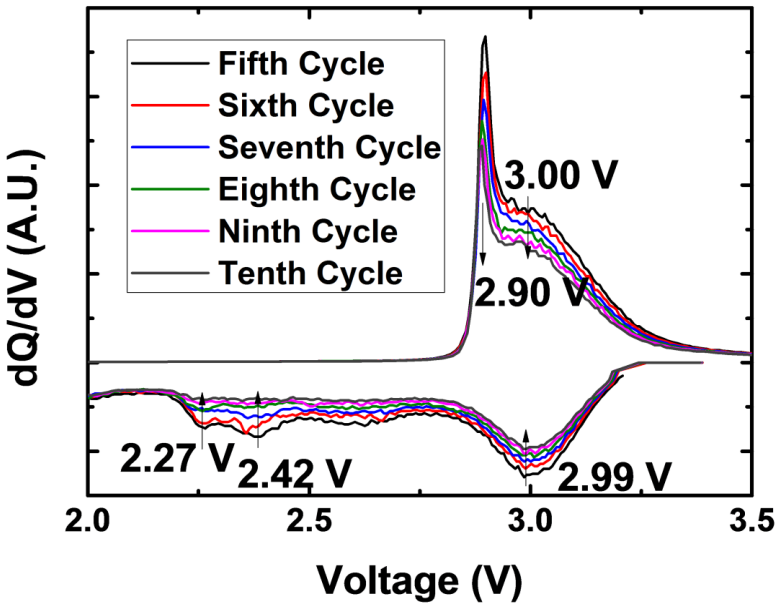

Figure 4.8. dQ/dV plot of the 5th to 10th cycles at a C/40 rate. Both reductive peaks and oxidative peaks decrease continuously.

In order to study how the rate of lithiation/de-lithiation affects reversibility, MIL-101(Fe) cells were cycled for 30 cycles at rates of C/60, C/40, C/20, and C/10 (**Figure 4.9**). Initially, faster rates were associated with lower degrees of lithiation; however, with extended cycling the cells cycled at faster rates exhibited better capacity retention than the cells cycled at slower rates. Specifically, the C/60 cell delivered a 30th cycle discharge capacity of only 0.1 Li/Fe while the C/10 cell delivered a 30th cycle discharge of 0.2 Li/Fe. The C/10 cell delivered a higher 30th cycle discharge capacity in spite of accommodating the least amount of lithium on the first cycle. This result clearly indicated that there is a stability issue with the lithiated state of MOF.

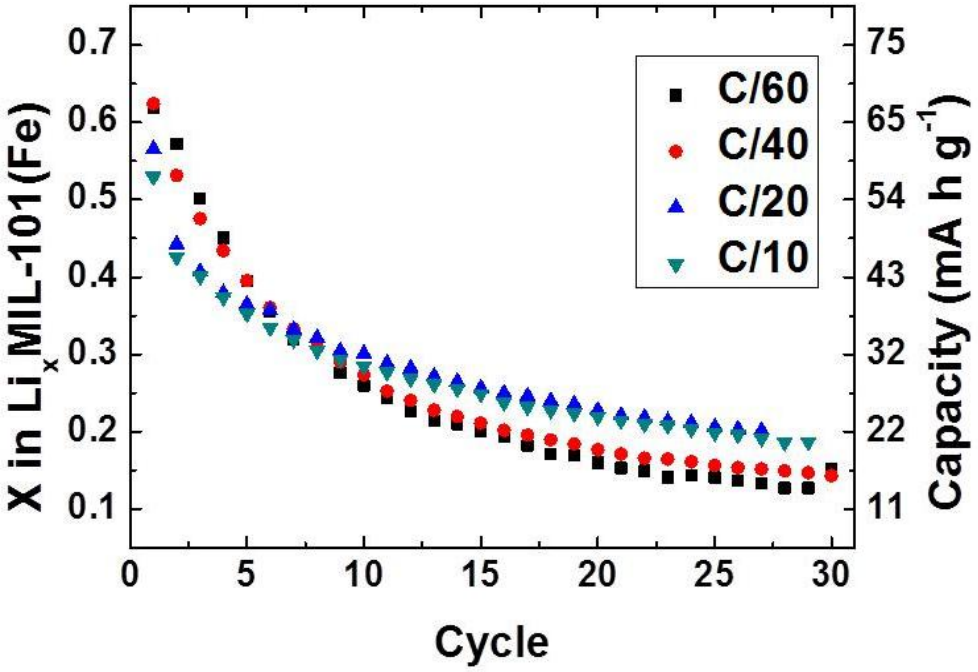

Figure 4.9. Results of galvanostatically cycling MIL-101(Fe) electrodes versus a Li counter electrode. Cyclic capacity of MIL-101(Fe) electrodes at a variety of different C-rates.

To further investigate the dependency that the rate has upon capacity retention, we studied how incorporating an open-circuit voltage rest into the cycling protocol affects the reversibility of lithium extraction. After being discharged at a rate of C/20, the MIL-101(Fe) cells were rested for 0, 10, 20, 50, or 72 hours and then charged at a rate of C/20. **Figure 4.10** it shows that the percentage of lithium extracted was dependent upon the duration of the rest step. If no rest step was included in the cycling protocol, then the Coulombic efficiency was 73%. However, the Coulombic efficiency was only 23% after a rest of 72 hours. This experiment indicates that lithiated MIL-101(Fe) suffers from an irreversible relaxation mechanism that reduces reversibility.

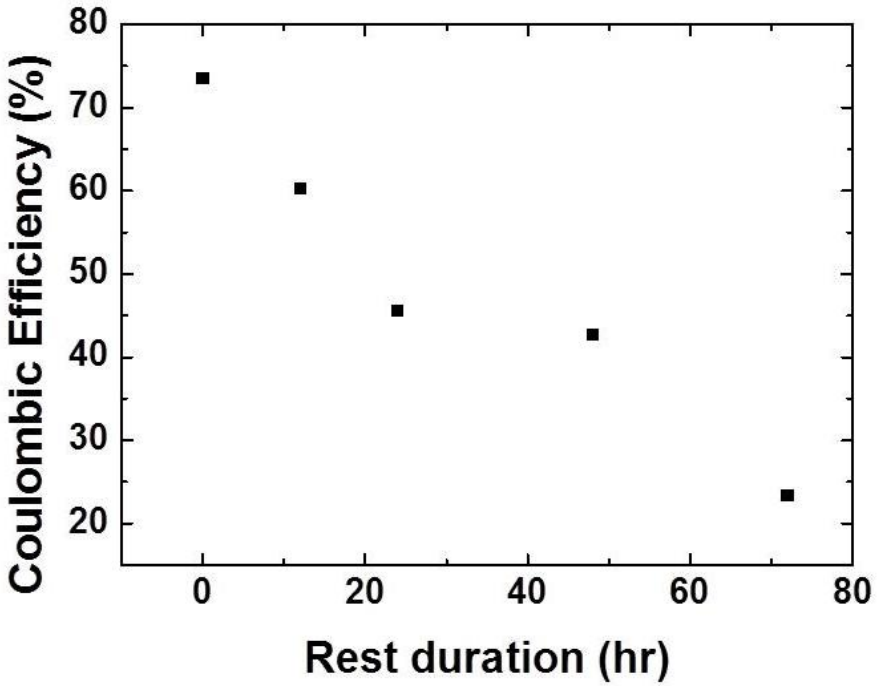

Figure 4.10. Results of galvanostatically cycling MIL-101(Fe) electrodes versus a Li counter electrode. First cycle Coulombic efficiency of MIL-101(Fe) electrodes which were rested between discharge (C/20) and charge (C/20) for different amounts of time. Coulombic efficiency decreases as the rest time is increased.

Like many battery materials, MOFs tend to undergo a conversion reaction if lithiated beyond a certain point. Very often this conversion reaction is irreversible. In the case of MOFs, if the Fe^{3+} is reduced beyond a certain point, this results in the disintegration of the material structure.[13, 25] Synchrotron PXRD was utilized in order to determine if any significant structural changes occur during cycling which could account for MIL-101(Fe) poor reversibility (**Figure 4.11**). A simulated PXRD pattern of MIL-101(Cr) was utilized as a reference.[26] MIL-101(Fe) shows some minor secondary phase peaks that are related to irreversible SP decomposition in the electrochemical cell. In addition, a reversible change in intensity was observed for some peaks including the (022) peak. These changes in intensity are attributed to solvent molecules intercalating along with the Li^+. Further discussions regarding the secondary phases and the intensities changes are described in the Supporting Information. Most importantly, the irreversible changes in the diffraction patterns were only related to the secondary phase, suggesting that MIL-101(Fe) was stable during cycling and that the poor capacity retention was not due to disintegration of the framework.

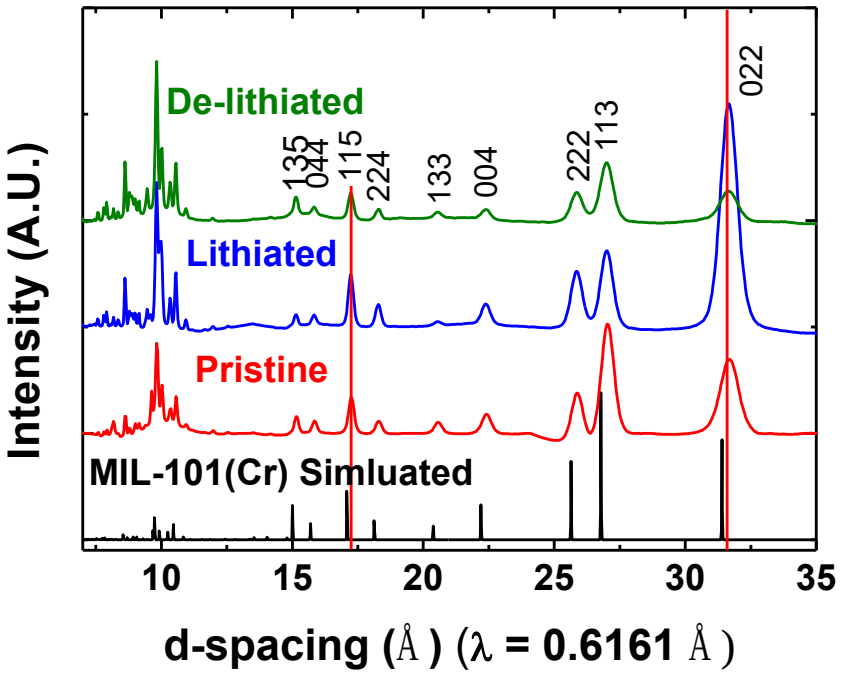

Figure 4.11. Synchrotron PXRD patterns for MIL-101(Fe) prior to cycling (red), after lithiation (blue), and after de-lithiation (green). Patterns are compared to a simulated pattern of the MIL-101(Cr) analogue structure. Red lines indicate peaks that show a reversible change in intensity.

In-operando XAS of the Fe K-edge was used to characterize the short range structural changes occurring in MIL-101(Fe) during a full lithiation/de-lithiation cycle at a rate of C/20. In the XAS experiment, MIL-101(Fe) only achieved an initial discharge capacity of 0.3 Li/Fe, whereas in the C/20 experiment without the beam, (**Figure 4.9**) MIL-101(Fe) could achieve an initial discharge capacity of 0.57 Li/Fe at the same rate. We suspect that irradiation of the sample during the *in-operando* XAS measurement contributed to a lower lithium insertion capacity.[27, 28] **Figure 4.12.a** presents a contour plot of the XANES region with respect to measurement time where it is observed that the Fe K-edge shifts to lower binding energy during lithiation and then reversibly shifts back to its pristine binding energy upon de-lithiation. A shift to a lower binding energy during

lithiation is consistent with the reduction of Fe^{3+} to a mixed valence state of Fe^{3+} and Fe^{2+}. Upon de-lithiation, the mixed valence state is oxidized back to Fe^{3+}. Because the binding energy shift is reversible, *in-operando* XAS also does not explain the poor capacity retention of MIL-101(Fe) (**Figure 4.10**).

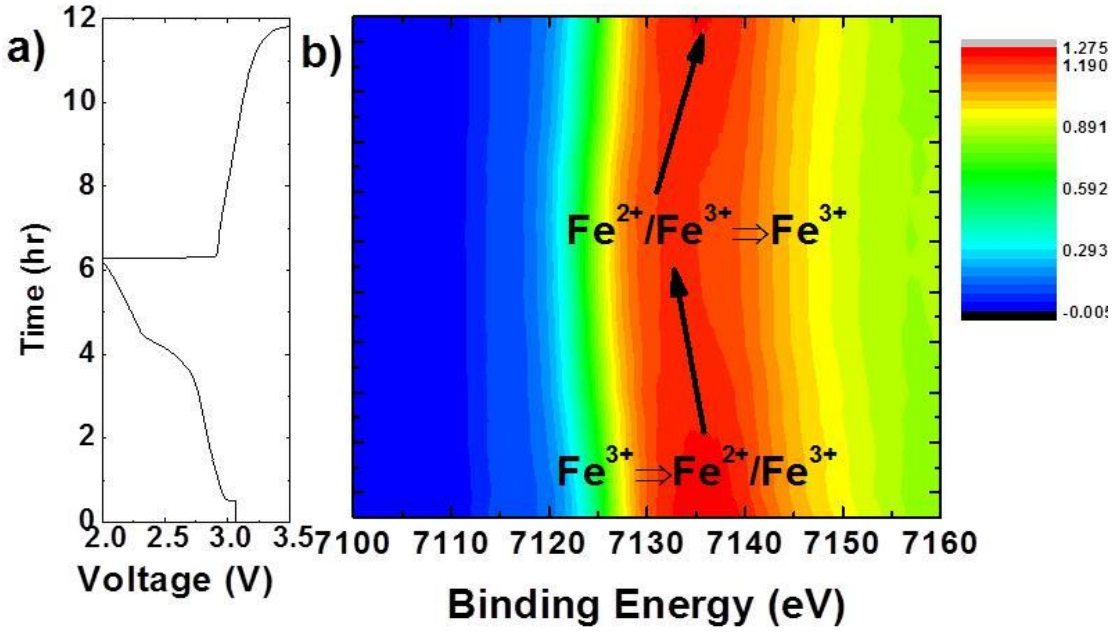

Figure 4.12. *In-operando* and *ex-situ* XANES of MIL-101(Fe). a) Voltage profile with respect to the *in-operando* XAS scanning time. b) The contour plot of the *in-operando* XAS XANES region versus time indicates a reversible change in the Fe oxidation state.

Unlike the *in-operando* XAS or PXRD experiments, the results of our *ex-situ* XAS experiment help describe the time dependent capacity fade mechanism. **Figure 4.13** presents a comparison between the *in-operando* and *ex-situ* XANES spectra of MIL-101(Fe) in its pristine, lithiated, and de-lithiated states. The time between electrode preparation and *ex-situ* XAS measurement was 3-4 days. Our first observation was that

the spectra intensities near the Fe K-edge were always lower for the *in-operando* samples. This can be explained by the fact that the *in-operando* samples were thicker than the *ex-situ* samples such that more signal was lost to self absorption.[29, 30] More importantly, the K-edge of the lithiated *ex-situ* sample did not shift to a lower binding energy as it did for the lithiated *in-operando* sample. This result indicates that the Fe^{3+}/Fe^{2+} mixed valence state formed upon lithiation is not stable over longer times. For this reason, the Fe^{3+}/Fe^{2+} mixed valence state can be observed only using *in-operando* XAS.

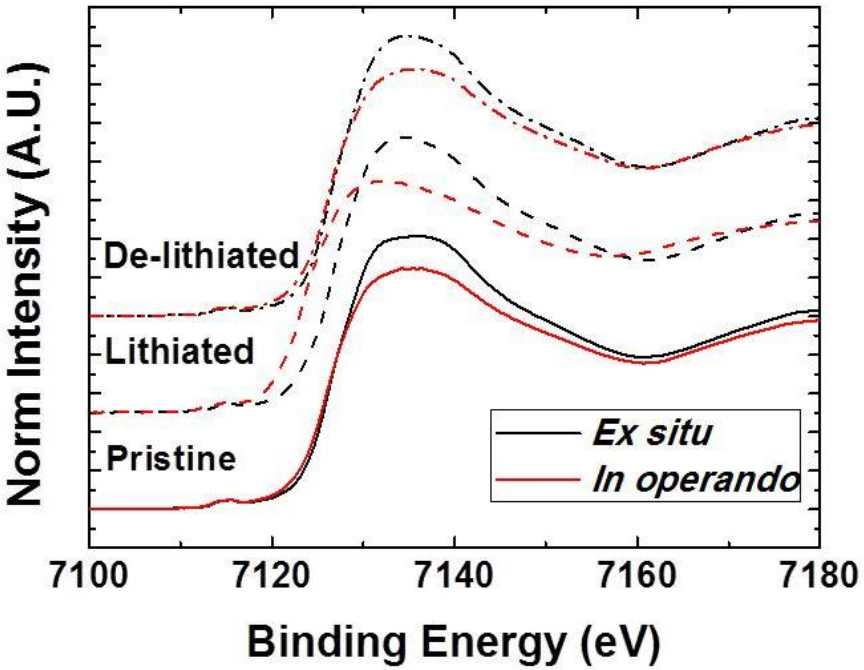

Figure 4.13. Comparison of the *in-operando* (red) and *ex-situ* (black) XAS XANES spectra. The Fe K-edge of the *ex-situ* lithiated sample does not shift to a lower binding energy that indicates the presence of a time dependent fade mechanism.

A contour plot of the *in-operando* XAS experiment Fourier transformed EXAFS spectra is provided in **Figure 4.14.** The Fourier transform of the EXAFS region is

correlated to the radial distribution of nearest neighbor atoms about Fe. The nearest neighbor atoms for Fe are observed at approximately 1.5 Å. In the pristine state, the three Fe ions of the SBU are coordinated with 17 O and one Cl nearest neighbor. The intensity of the spectrum at 1.5 Å decreases upon lithiation and then increases again upon de-lithiation. We attribute the variability of intensity to a reversible change in the coordination environment of the nearest neighbors. Cl^- ions are known to be labile[31] and scatter X-rays more intensely than O^{-2} ions. With this in mind, it may be possible that for each Fe, one O atom from an electrolyte solvent molecule replaces Cl^- ion upon full lithiation.

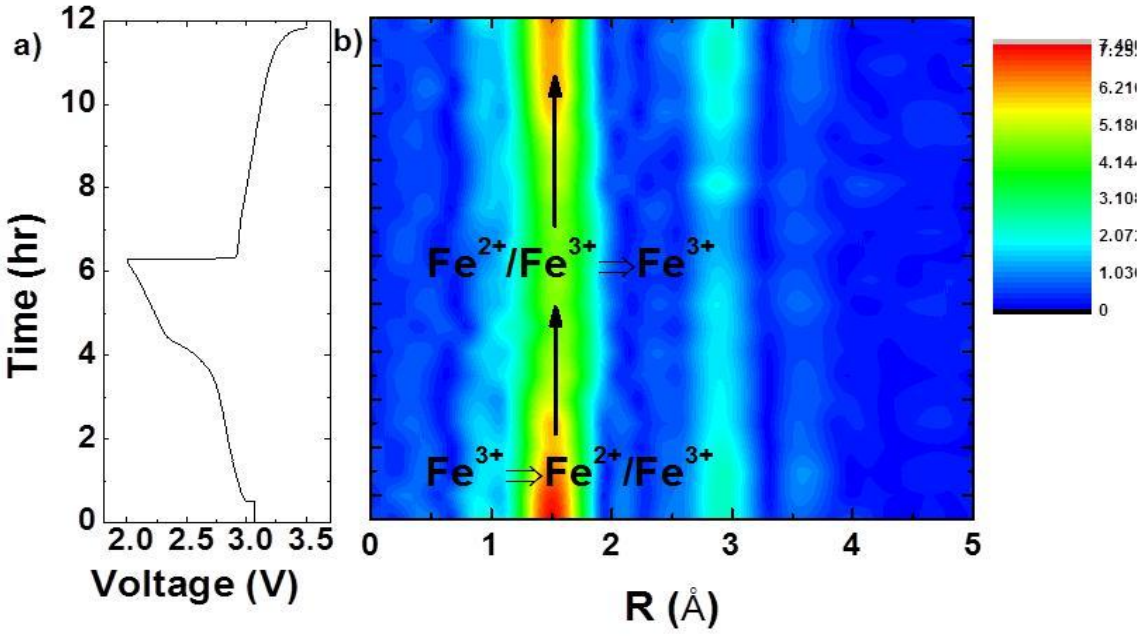

Figure 4.14. Fourier transformed EXAFS region of the *in-operando* XAS data. a) Voltage profile with respect to the *in-operando* XAS scanning time. b) Contour plot of the EXAFS region versus time that indicates a reversible change in Fe coordination during cycling.

To gain further insight into the EXAFS results, electronic structure calculations on the MIL-101(Fe) SBU were performed. A simplified SBU model (Trimer, Figure 4.3.a) was used in the calculations. Similarly to the model provided in **Figure 4.1.a**, the SBU model includes the three Fe centers, but replaces the benzene groups with methyl groups in order to reduce the computational cost. An additional model (TrimerDMC, Figure 4.3.b) has been also investigated. In this second model, the axial Cl has been replaced by a carboxylate group, coordinated to the Fe center via one oxygen atom from the carbonyl group. Both models have been used to evaluate the changes in the free energy associated with incremental reduction of the metal centers.

Because there are different reduction centers in the two models, all possible combinations were calculated (**Figure 4.15 and Table 4.1**). In **Figure 4.15**, blue and green dots are used to simply represent the electronic structure of Fe. The calculated free energy of the reduced SBUs was found to be largely independent of the particular Fe center reduced. The first electron reduction of Fe (one green dot, one Fe center reduction Fe^{3+}/Fe^{2+}) required -3.13 eV for the Trimer model and -6.46 eV for the TrimerDMC model. In all four cases one electron reduction is associated with a negative ΔG indicating that both models strongly prefer to exist in a reduced state. These results indicate that the reduction of the MIL-101(Fe) SBU is twice as favorable when a DMC molecule is coordinated to the iron metal center, and that Cl^- coordination can slow down the reduction process. Furthermore, the second electron reduction (2 green dots, two Fe center reductions Fe^{3+}/Fe^{2+}) requires -3.36 eV for the Trimer model and -9.00 eV for the TrimerDMC model. In both cases, addition of a second electron provides with further

stabilization on the system. However, the reduced TrimerDMC model is much more stable than the Trimer model. This allows us to conclude that substituting Cl^- for a DMC molecule makes the MIL-101(Fe) MOF much more prone to a two electron reduction, results that can be correlated with the changes in the PXRD peak intensities with cycling (**Figure 4.11**).

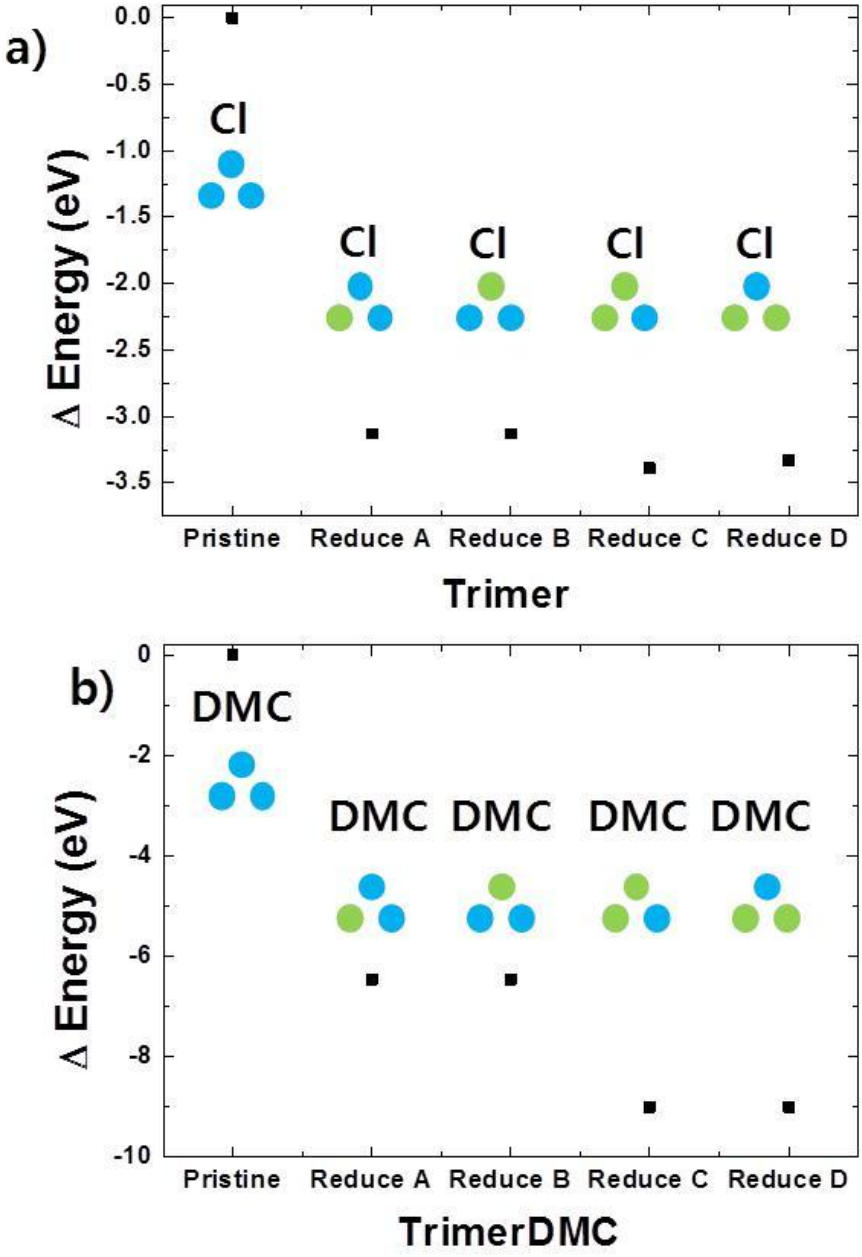

Figure 4.15. Gibbs free energies relative to the respective pristine state are shown for the a) Trimer and b) TrimerDMC model and its reduced forms. Insets: Oxidation state of Fe for the respective reduced states are illustrated in simple dots. Blue dots are Fe^{3+} and green dots are Fe^{2+}.

Table 4.1. List of computation conditions and their respective results. HS has all three Fe spins up. BS1 has only Fe1 spin state down. BS2 has only Fe1 spin state down. BS3 has only Fe1 spin state down.

Model	Reduction stat	Spin State	Energy (keV	Total Spin (S^2)	Decontaminated Energy (keV)
Trimer	Pristine	HS	-152.7917767	63.7724	N/A
		BS1	-152.7919557	13.6159	-152.7917838
		BS3	-152.7918162	13.7084	-152.7917854
	Reduce A	HS	-152.7949151	56.0435	N/A
		BS1	-152.7950053	15.9146	-152.7949196
		BS2	-152.7950653	10.8916	-152.7949218
		BS3	-152.7949871	10.9323	-152.7949183
	Reduce B	HS	-152.7949152	56.0435	N/A
		BS1	-152.7950593	10.8878	-152.7949216
		BS3	-152.7946393	15.9733	-152.7949014
	Reduce C	HS	-152.7951707	48.7842	N/A
		BS1	-152.7952647	12.6672	-152.7951759
		BS2	-152.7952107	8.6362	-152.7951727
		BS3	-152.7951166	48.7854	-152.7951166
	Reduce D	HS	-152.7951853	12.6638	N/A
		BS1	-152.7951113	8.6112	-152.7951163
		BS3	-152.7951878	12.7043	-152.7951205
TrimerDMC	Pristine	HS	-149.6101776	63.7702	N/A
		BS1	-149.6103224	13.6399	-149.6101834
		BS3	-149.6103053	13.6504	-149.6101827
	Reduce A	HS	-149.6166378	56.0555	N/A
		BS1	-149.6166383	15.918	-149.6166378
		BS2	-149.6167581	10.8877	-149.6166431
		BS3	-149.6167601	10.884	-149.6166432
	Reduce B	HS	-149.6166361	56.0554	N/A
		BS1	-149.6168128	10.8838	-149.616644
		BS3	-149.6166971	15.9284	-149.6166392
	Reduce C	HS	-149.6191745	48.7758	N/A
		BS1	-149.6192814	12.6601	-149.6191804
		BS2	-149.6193124	8.6136	-149.6191813
		BS3	-149.6192338	12.6815	-149.6191778
	Reduce D	HS	-149.6191745	48.7758	N/A
		BS1	-149.6192368	12.6614	-149.6191779
		BS3	-149.6193094	8.6088	-149.6191812

4.4. Discussion

MIL-101(Fe) as-synthesized, has an octahedron particle morphology **(Figure 4.16)**. The particles size range in the 2 μm and less. Since MIL-101(Fe), due to the BDC organic linkers acting as nodes, have low electrical conductivity. To compensate for the low electrical conductivity, 30 wt% Super-P conductive carbon is mixed with the MIL-

101(Fe). To enhance the carbon to MIL-101(Fe) contact, the two powders are ball milled together. Here, one may be concerned that MIL-101(Fe) crystal structure may be destroyed due to the intensive physical or mechanical energy applied during the ball milling process. To justify that the MIL-101(Fe) crystal structure is uncompromised, PXRD is taken after the various ball milling conditions (**Figure 4.17**). As expected, at high RPM, the crystal structure does completely collapse. However, at low RPMs, 200 RPM and 100 RPM, the overall crystal structure integrity is maintained. In going forward with the electrochemical reactions, 100 RPM condition is chosen.

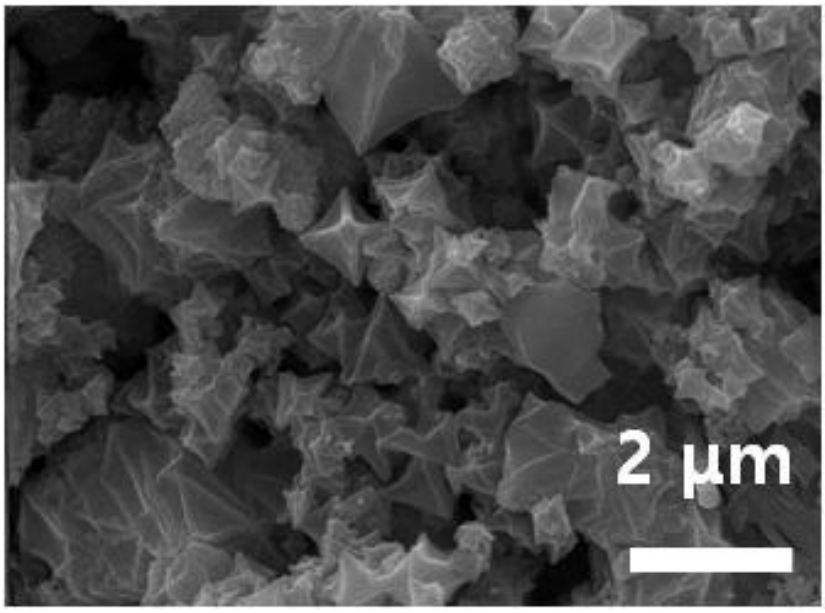

Figure 4.16. SEM image of the as-synthesized MIL-101(Fe).

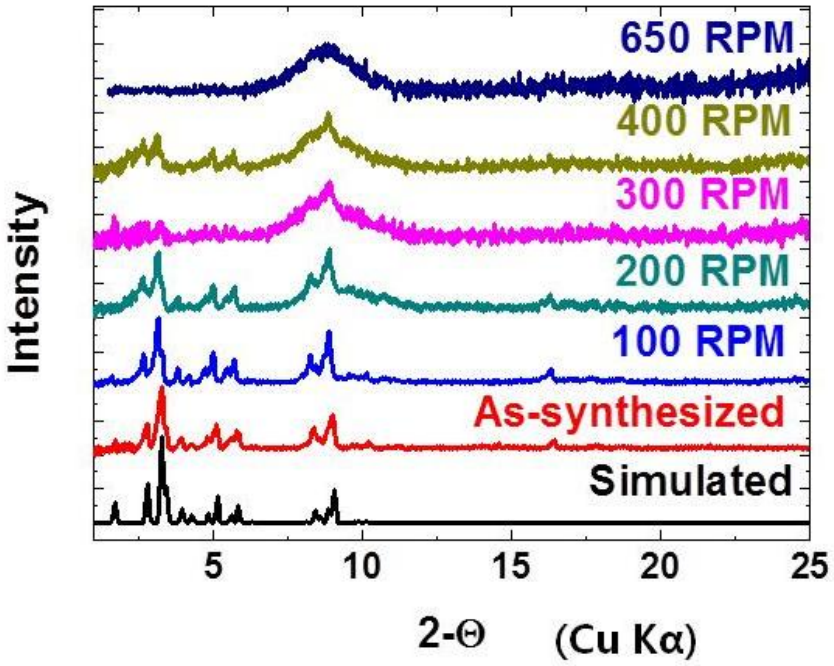

Figure 4.17. PXRD of the MIL-101(Fe) before and after various states of ball milling conditions.

Relaxation of Fe^{2+} to Fe^{3+} will result in the irreversible accumulation of Li^+ ions in MIL-101(Fe). As more Li^+ ions accumulate, MIL-101(Fe) loses potential Li^+ ion insertion sites and empty Li^+ site energy drastically increases for future cycles. Computational work on MIL-53(Fe) supports this notion.[25] As the sites fill up, the energy required for additional Li^+ insertion will eventually surpass the free energy of Fe^{3+} reduction. It is the constant accumulation of Li^+ ions that cause the capacity of MIL-101(Fe) to rapidly fade.

MIL-101(Fe) was lithiated with roughly 0.6 Li/Fe when discharged down to 2.0 V. Compared to MIL-53(Fe), one of the previous MOFs which showed most promise in LIB, MIL-101(Fe) had a higher voltage cut-off by 0.5 V. Such advancement may be due to the fact that MIL-101(Fe) has larger pores than MIL-53(Fe). Li^+ can be solvated by either

two (174.5 Å^3) or four (350 Å^3) DMC molecules.[34] Only MIL-101(Fe) has large enough pores and pore windows to allow solvated Li^+ to diffuse in and out of the material (**Figure 4.1.b**).

Five reduction peaks were observed in differential capacity (dQ/dV) plot (figure 4.8). In MIL-53(Fe), lithium insertion process primarily involves two reactions. The first is a kinetically limited solid-solution reaction. The second is a two-phase reaction.[34] Like MIL-53(Fe), it is expected that the lithiation of MIL-101(Fe) also proceeds with a series of solid-solution reactions followed by a series of two phase reactions. Evidence of solid-solution and two phase reaction are provided by ex-situ EXAFS (figure 4.7). No clear change in Fe coordination during lithiation to 2.5 V suggests a solid solution reaction, while a change in Fe coordination during lithiation from 2.5 V to 2.0 V suggests a two phase reaction (**Figure 4.14 and Figure 4.7**).

In the PXRD results, some irreversible structural changes were observed to occur at lower d-spacing (**Figure 4.8**). To further diagnose the diffraction patterns, the three synchrotron PXRD patterns were profile matched with Fd-3m cubic symmetry (**Figure 4.18, Figure 4.19, and Figure 4.20**).[134] Overall, the peaks matched well with some exceptions in the lower d-spacing. Three peaks in which did not match well in the cubic symmetry were near 9.7, 9.6, and 9.1 Å. The impure peak observed near 9.7 Å started to disappear upon lithiation and completely disappeared upon de-lithiation. Comparing PXRD result of as-synthesized material and the pristine which had been ball milled with Super-P (SP) the conductive carbon additive, the peak near 9.7 Å, was a product of ball milling SP and the MOF together (**Figure 4.21**). A new peak near 9.6 and 9.1 Å appeared as 9.7 Å peak disappeared. Since the ball milled SP is known to have irreversible

electrochemical reaction, these peak can be attributed to the decomposition of SP during electrochemical test.[135] Regardless of the impurities, the irreversibilities were not related to the cubic MIL-101(Fe) framework.

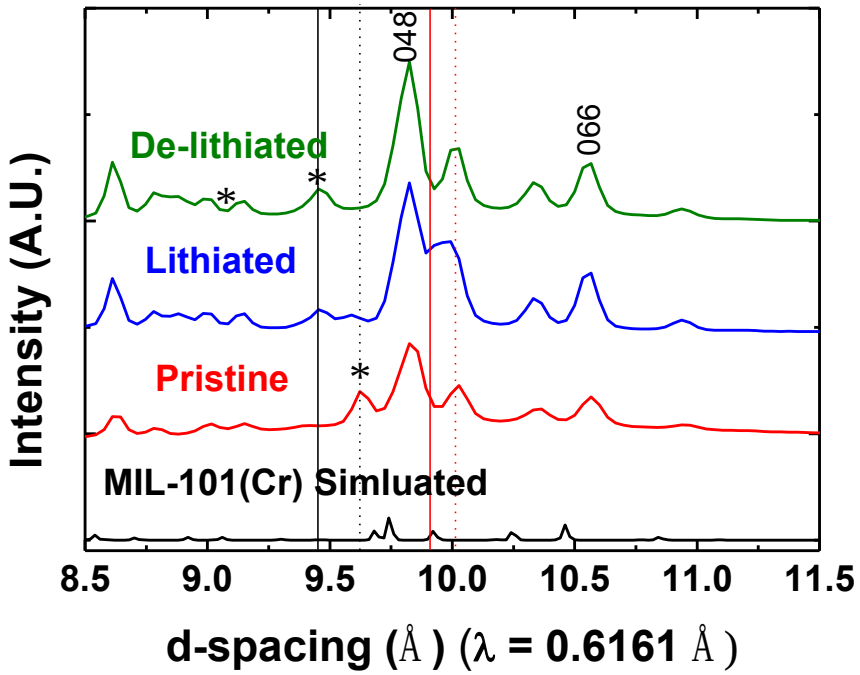

Figure 4.18. Lower d-spacing PXRD of MIL-101(Fe) at its pristine, lithiation and de-lithiated states. Irreversible peak disappearance and appearances are labeled with "*" sign.

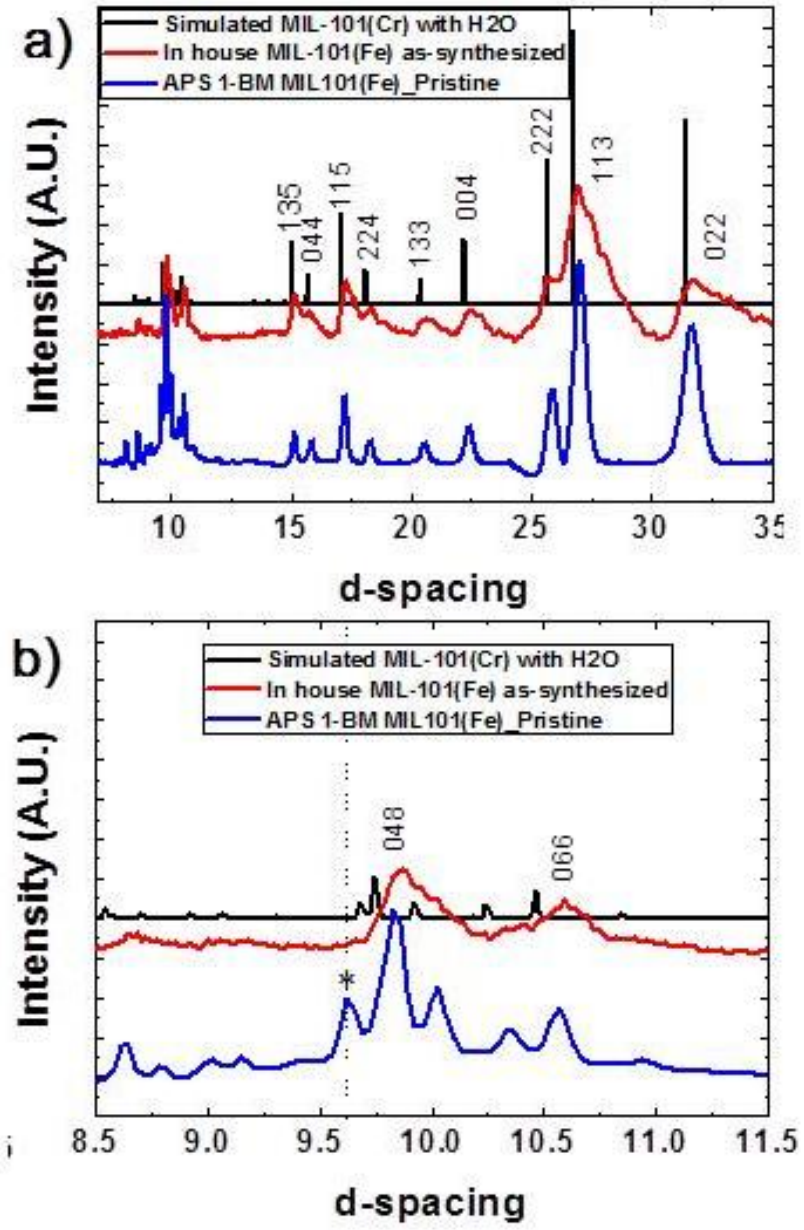

Figure 4.19. a) PXRD comparison of MIL-101(Fe) at its as-synthesized state, electrode (pristine) state, and simulated state. b) Lower d-spacing PXRD of a). The as-synthesized PXRD pattern is collected using a Bruker D8 Advance diffractometer at 40 KV, 40 mA for Cu Kα (λ=1.5418 Å), with scan speed of 0.1 sec/step, a step size of 0.02◦ in 2θ and a 2θ range of 1.0 to 55°. The experimental backgrounds were corrected using Jade 5.0 software package. The pristine PXRD pattern is collected from APS 1-BM using synchrotron source as described in this paper. A secondary phase near 9.7 Å d-spacing is labeled with "*".

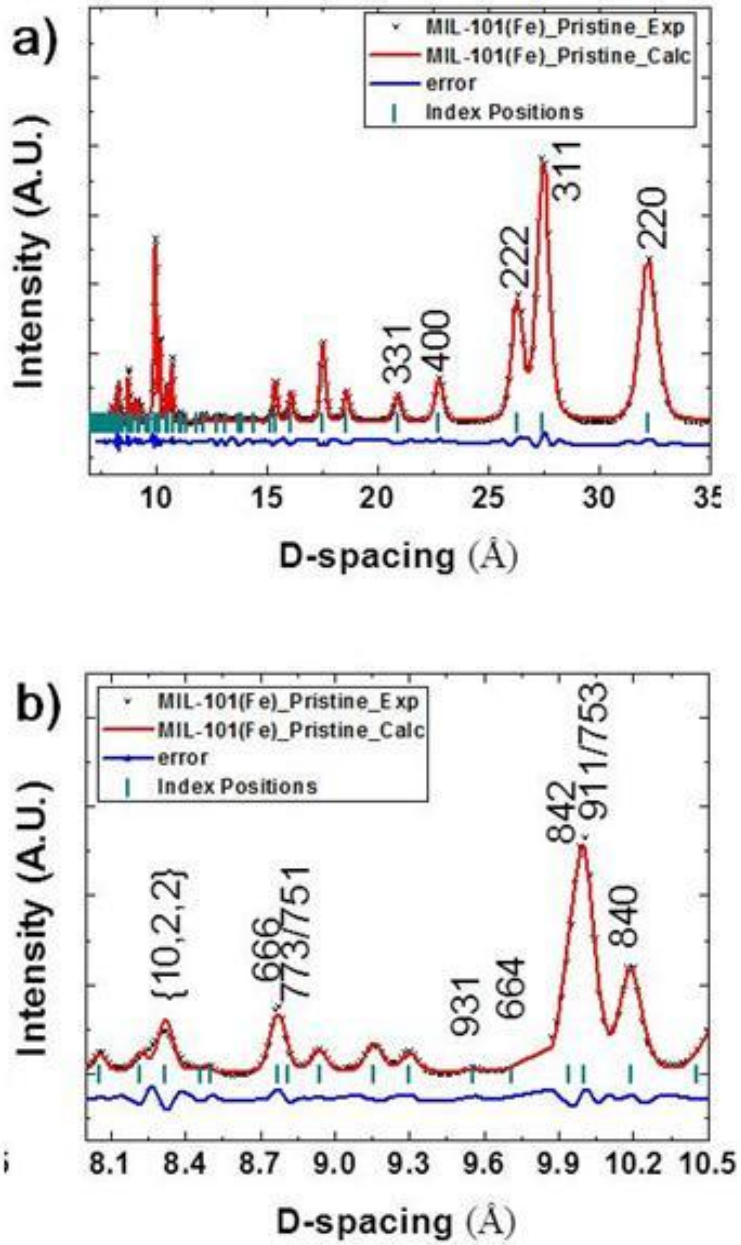

Figure 4.20. a) Profile matched MIL-101(Fe) pristine synchrotron PXRD pattern. b) Lower d-spacing PXRD of a). Regions associated with the secondary phase were excluded from the fit.

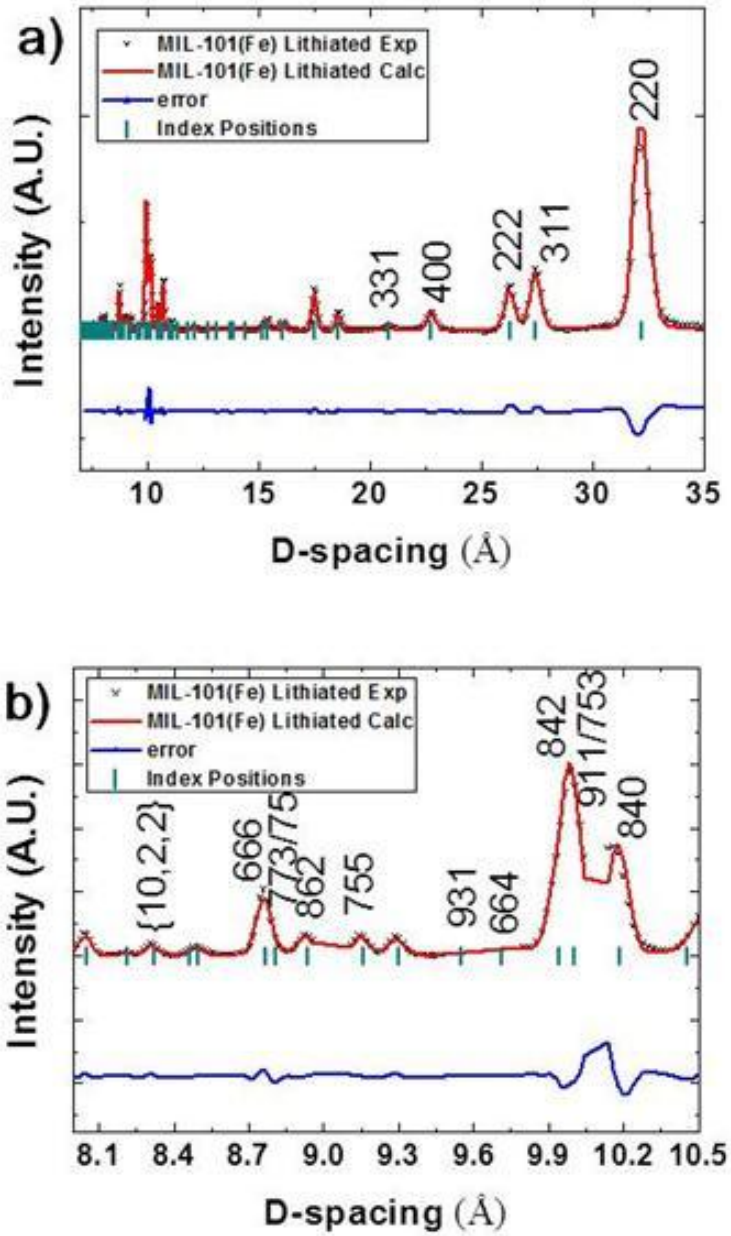

Figure 4.21. a) Profile matched MIL-101(Fe) lithiated synchrotron PXRD pattern. b) Lower d-spacing PXRD of a). Regions associated with the secondary phase were excluded from the fit.

In the higher d-spacing, there are increases in intensity for some peaks including the (022) peak. The increased peaks reversibly decreased in intensity after the de-

lithiation. To comprehend this phenomenon, some diffraction patterns were simulated (**Figure 4.22**). A MIL-101(Cr) was simulated from the reported crystal information file (CIF). The CIF contains oxygen atoms from solvent molecules. After deleting the oxygen atoms from solvent molecules, PXRD pattern was simulated again. Clearly, a decrease in intensity of (022) peak was observed for desolvated PXRD simulation. The same trend was observed when Cr was changed to Fe. Upon lithiation, electrolyte solvent molecules will be co-intercalating with Li^+. We suspect that when the Li^+ are intercalating inside the MOF, the solvent molecules will also intercalate. Therefore, the reversible peak intensity changes are likely due to electrolyte solvent molecules intercalating in the MOF.

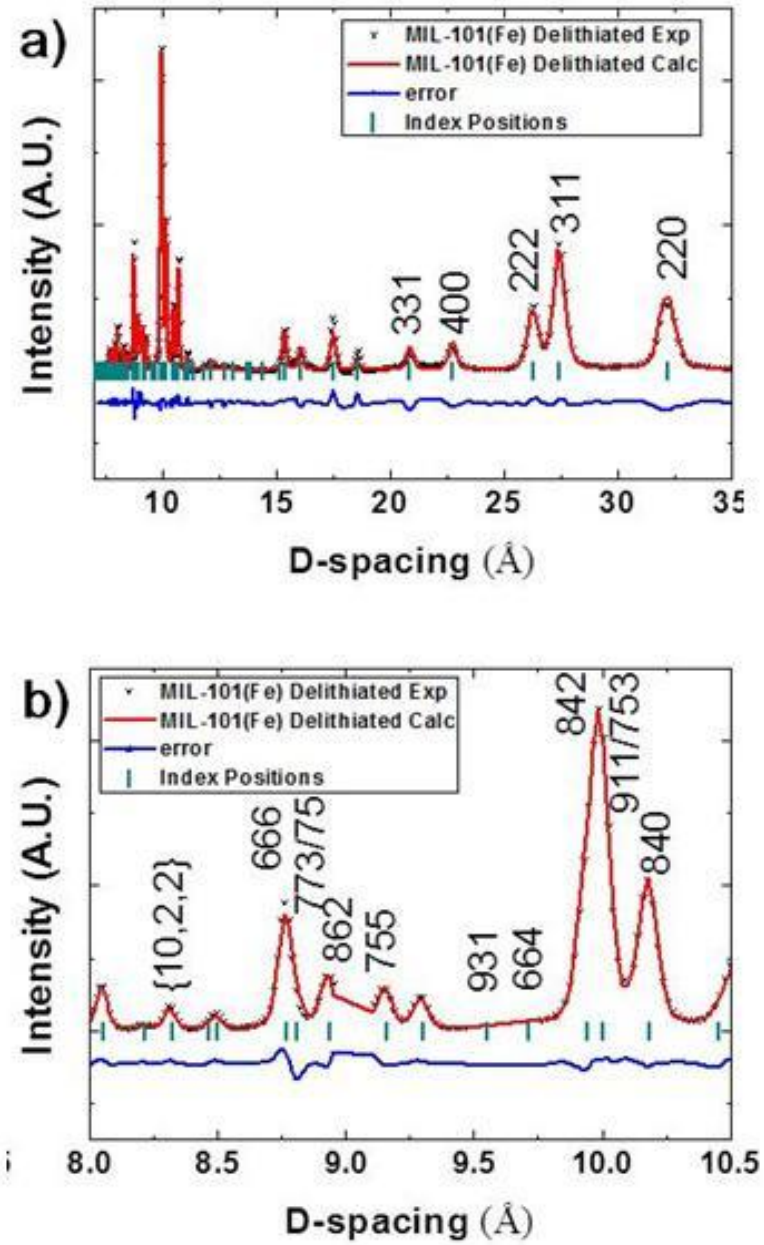

Figure 4.22. a) Profile matched MIL-101(Fe) de-lithiated synchrotron PXRD pattern. b) Lower d-spacing PXRD of a). Regions associated with the secondary phase were excluded from the fit.

Table 4.2. Profile matching parameters for MIL-101(Fe) synchrotron PXRD patterns.

MIL-101(Fe)	**a (Å)**	χ^2	**Space Group**	**Lamda (Å)**	**Excluded regions (Å)**
Pristine	89.781(3)	1.014	Fd-3m	0.6168	~9.5-9.7
Lithiated	89.687(3)	2.179	Fd-3m	0.6168	~8.8-8.9,~9.3-9.7, ~9.9-10.0
De-lithiated	89.690(2)	0.3262	Fd-3m	0.6168	~8.8-8.9, ~9.3-9.7

The main difference among the synchrotron sourced PXRD is the relative intensity of the 022 peak (**Figure 4.11**). Based on the Gaussian 09 computation and the EXAFS results, the guest molecules may be entering the pores. To test this phenomenon, the PXRD pattern of the 022 peak is simulated with water as guest molecules within the pores and without (**Figure 4.23**). It is clear that when there are guest molecules orderly trapped inside the pores of MIL-101(Fe), the 022 peak intensity decreases. This implies that when the MIL-101(Fe) electrode is lithiated, the guest molecules enter with the Li^+. This causes the changes in relative intensity changes.

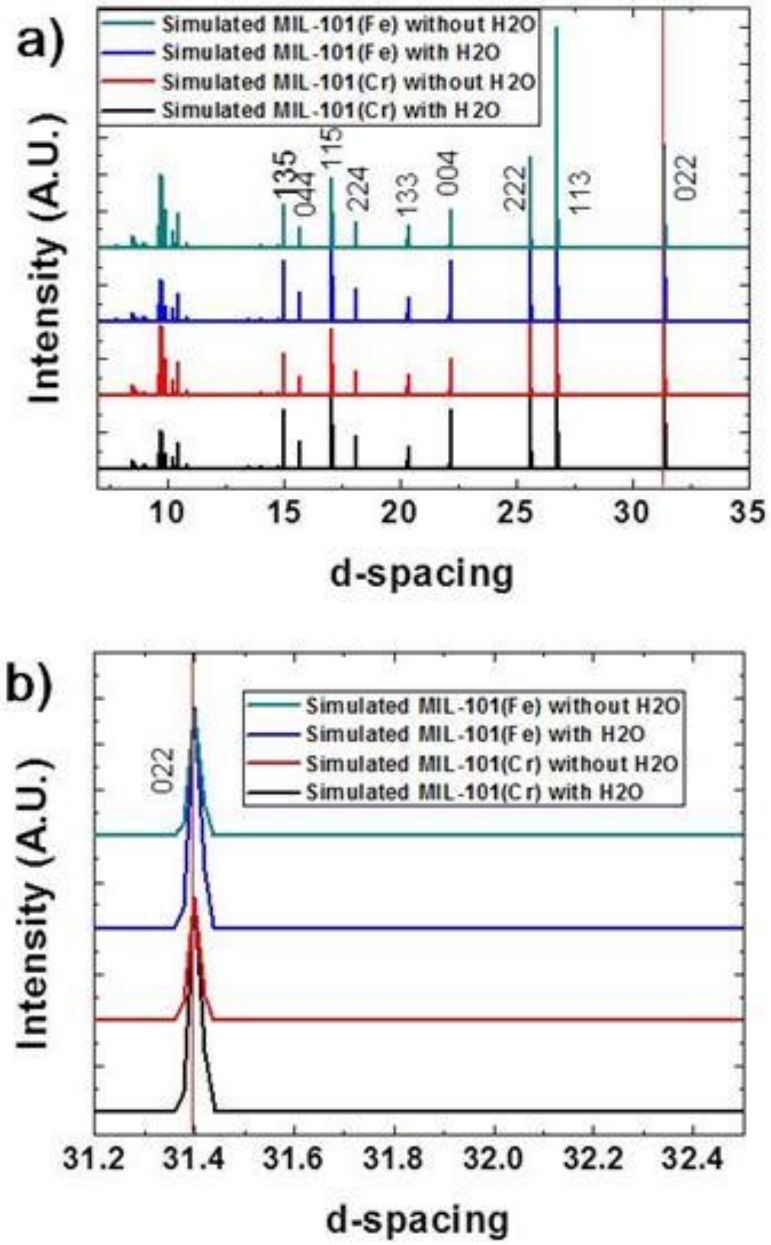

Figure 4.23. a) Simulated PXRD patterns using solvated MIL-101(Cr), desolvated MIL-101(Cr), solvated MIL-101(Fr), and desolvated MIL-101(Fe). b) Higher d-spacing PXRD of a). One of the intensity changing peaks (022) is labeled with solid red line.

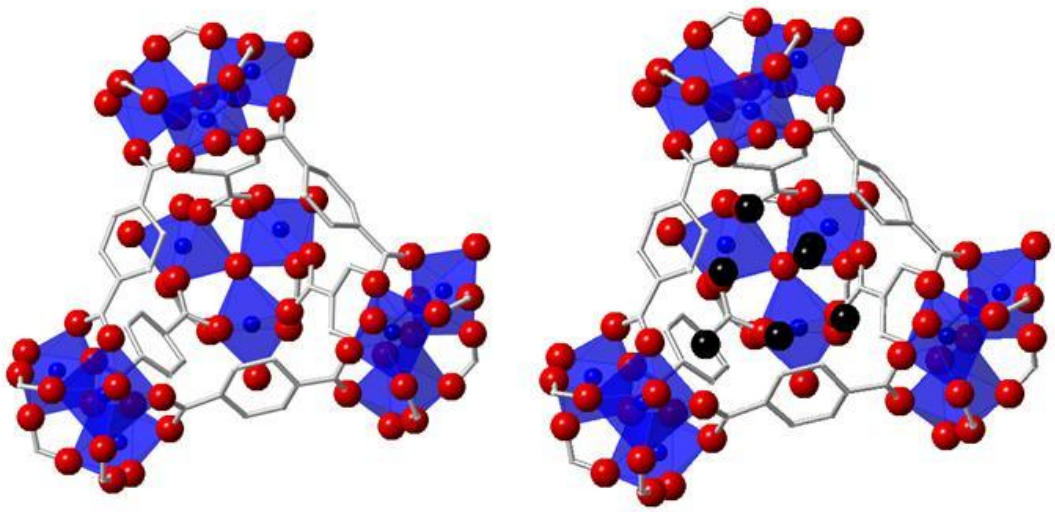

Figure 4.24. Left: the crystal structure of MIL-101(Fe) without H_2O guest molecules and Right: the crystal structure of MIL-101(Fe) with H_2O guest molecules used for PXRD simulation

In addition to the *in-operando* EXAFS, we conducted an *ex-situ* EXAFS experiment (**Figure 4.6 and Figure 4.7**). *Ex-situ* EXAFS spectra were collected after the MIL-101(Fe) MOF electrode was reduced to 2.5 V and again after the electrode was further reduced to 2.0 V. Although the first neighbor peak intensity was identical for the pristine and the 2.5 V sample, there is a reduction in the first neighbor peak intensity for the 2.0 V sample. When the electrode was oxidized back to 3.5 V, the first neighbor peak did not completely regain intensity. The *ex-situ* EXAFS data thus provide further support for our computational results suggesting that Cl^- ions may be irreversibly replaced by DMC molecules in order to decrease the free energy of Fe site reduction.

A major point provided from the electronic structure calculations is the significant difference observed in the free energy profiles associated to the changes in the axial coordination sphere of the iron metal center. Different coordination spheres lead to different behaviors towards reduction, thus affecting the recycling efficiency of the

material. The resulting electron density of the trimer and trimerDMC models (**Figure 4.25**). Because a Cl^- ion can be more easily detached from the coordination sphere. As observed in **Figure 4.10**, a longer rest time between the lithiation and de-lithiation reduces the coulombic efficiency. This temporal effect can be associated with Cl^- ligand lability. After lithiation, the Cl^- ligand can dissociate from the Fe center, and with longer times, the anion can diffuse further away from the metal center. This may have detrimental effects on the electrochemical performance since MIL-101(Fe) will not regain its pristine structure after de-lithation. One way to try to avoid such irreversible change is to switch Cl^- to F^- to strengthen the bond between Fe-F. However this will require the use of HF. Other possible ways to improve the reversibility of the MIL-101(Fe) redox would be to improve the stability of its reduced SBU. To stabilize the SBU, one can alter the electronic structure of SBU. Many studies have demonstrated different pathways to alter the electronic structure via ligand functionalization,[136] by increasing the conjugation on the system.[9] In addition, one can replace the ligands with other redox active organic molecules such as benzoquinones,[137] organic radicals,[26, 138, 139] or oxocarbons.[136]

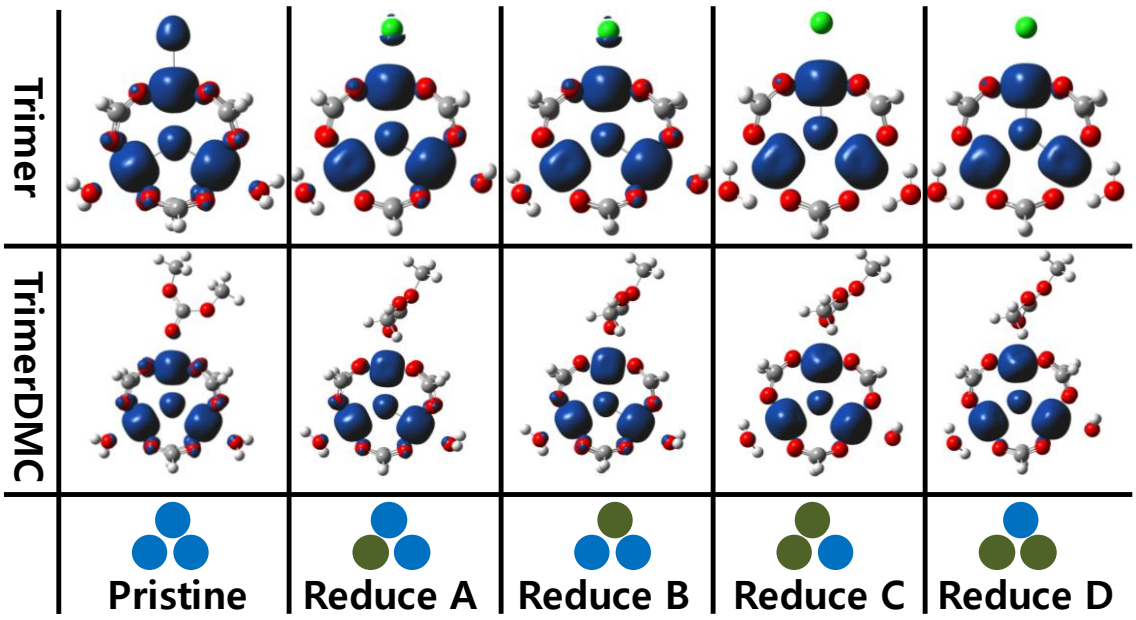

Figure 4.25. Spin densities of the respective calculations. First row shows the results obtained from the Trimer model. Second row shows the results obtained from the TrimerDMC model. Spin density, oxygen, carbon, and hydrogen atoms are colored blue, red, grey, and white, respectively. Third row describes the electronic structure of the calculation. The three circles represent Fe nuclei. Blue means trivalent and olive means divalent.

4.5. Conclusion

In this work, the MIL-101(Fe) MOF was tested as an electrode for use in lithium ion batteries. The redox chemistry (Fe^{2+}/Fe^{3+}) was found to not be completely reversible. We characterized the decay mechanism using *ex-situ* and *in-operando* XAS measurements. The Fe^{2+} oxidation state was not observed from *ex-situ* experiments. The temporal dependency of Fe^{2+} observation indicates the importance of *in-operando* experiments. The computational results indicate that significant energy differences can be expected between the pristine and reduced forms of MIL-101(Fe). This is ascribed to the axial ligand coordinated to the Fe^{3+} metal centers. Our study thus suggests that an

appropriate functionalization of the MIL-101(Fe) SBUs can improve the reversibility of the Fe^{2+}/Fe^{3+} redox reaction.

Chapter 4, in part, is a reprint of the material "MIL-101(Fe) as a lithium-ion battery electrode material_ a relaxation and intercalation mechanism during lithium insertion" as it appears in the Journal of the Material Chemistry A, Jaewook Shin, M. Kim, J. Cirera, S. H. Chen, G. Halder, T. A. Yersak, F. Paesani, S. M. Cohen and Y. S. Meng, 2015, 3, 4738. The dissertation author was the primary investigator and author of this paper.

Chapter 5. Relaxation of ZnO on Bismuth Species Towards Rechargeable Zn-based Aqueous Battery

5.1. Introduction

Rechargeable or secondary batteries have become an essential part of everyday life. A battery is the most efficient way of storing energy because it does not need an external conversion mechanism.[4] While the need for a low-cost battery is rising, LIBs dominate the secondary battery in the market even though the material synthesis for a LIB is energy intensive and expensive.[23-26] LIBs utilize ceramic oxides and highly ordered graphite, which require high temperature synthesis and organic electrolytes, which are flammable and require expensive casing (**Figure5.1**).[2] One attractive option to lower the cost of energy storage is to design secondary batteries with aqueous electrolyte. Zn anodes are a promising aqueous battery material because they are nontoxic, earth abundant, low-cost, and energy dense resource.[140] Utilizing Zn anode also raises the working voltage due to its low reduction voltage, thus applying a rechargeable Zn anode can dramatically drop the cost of secondary batteries.[141]

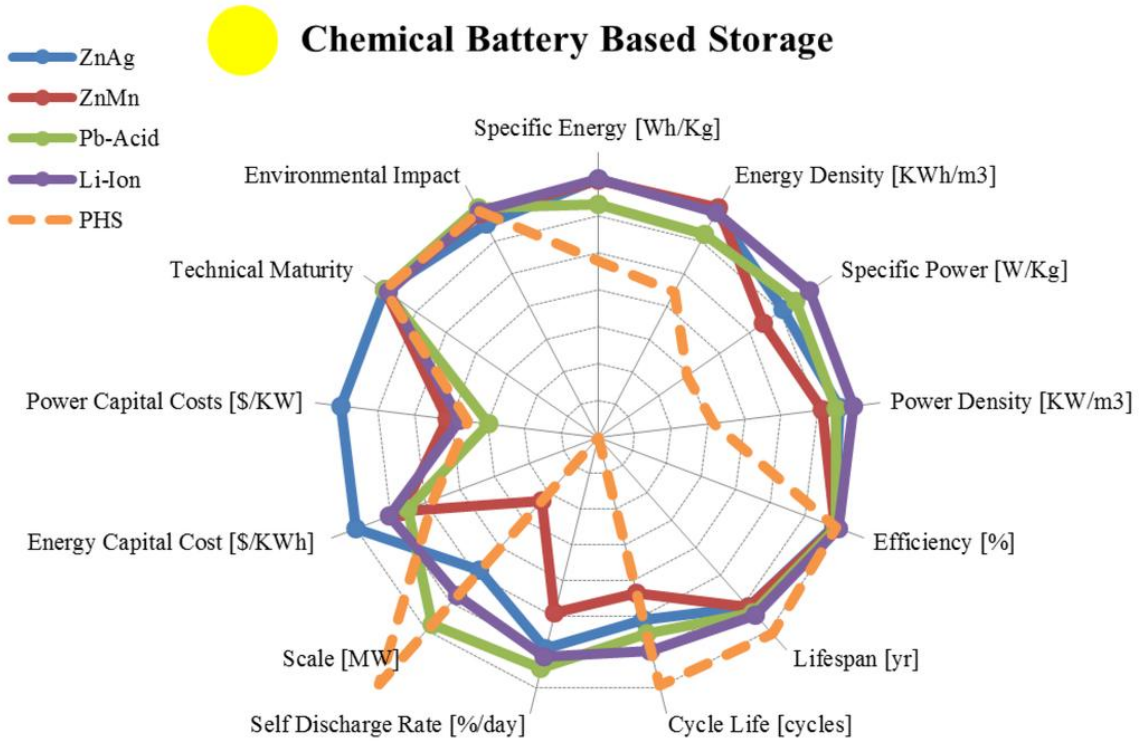

Figure 5.1. Comparing chemical energy storage in typically batteries using normalized and logarithmically plotted average data.[2]

Zn anodes are one of the oldest electrochemical electrodes dating back to the batteries invented by Alexssandro Volta in the 1800s, yet commercial rechargeable Zn anode implementation is scarce because the Zn anode suffers from a critical intrinsic issue. It has been long discovered that when Zn oxidizes (or discharges), zincate ions are formed and relax to ZnO.[142] The problem is that the zincate ions are soluble in aqueous alkaline electrolyte. When the zincate ions are formed, the ions detach from the Zn surface and dissolve in the electrolyte. Eventually the Zn particles lose the electrical connections rendering the anode no longer rechargeable. As Zn anode is a promising

anode for both alkaline batteries[141, 143] and the metal-air batteries,[140, 144, 145] resolving the rechargeability with Zn anode is beneficial to the field of electrical energy storage.

To overcome this issue, there are numerous reports utilizing various methods including composite, electrolyte modification, and nanostructuring.[146-150] Among them, the composite addition of Bi_2O_3 is notable for its simplicity and effectiveness. Some reports show that Bi_2O_3 significantly improves the cycling performance of the Zn anode, however much of the literatures suggest that enhanced cycle performance is due to the advanced electrical conductivity.[150, 151] Moser et al. observed Bi metal formation through *in situ* powder X-ray diffraction (PXRD) and concluded that the Bi metal further increased the conductivity.[151] However, it is difficult to argue that Bi_2O_3 is the most effective additive to elevate the electrical conductivity. Bi_2O_3 exhibits p-type electronic conductivity in room temperature, but it is heavy and not easy to obtain high surface area.[152] Using Bi_2O_3 as a conductive additive makes the whole electrode too heavy without providing much electrical connection. A more optimum choice to increase the conductivity is to employ simple conductive carbon with high surface area. But it is known that the benefit of Bi_2O_3 surpasses that of the carbon.[153] Therefore, a more comprehensive understanding of the mechanism of a Zn and Bi_2O_3 composite electrode is needed. This paper proposes that when the zincate ions are formed, the ions are deposited onto the surface of bismuth species, which allows the Zn anode to be rechargeable. The authors prove this with various characterizations of the composite electrode at different states of electrochemical cycles.

5.2. Experimental Section

Composite electrode mass ratio*:* For the Zn electrode without additives, Zn (96.4 wt%) and polyvinylidene fluoride (PVDF) (3.6 wt%) was utilized. For the Zn electrode with Super-P (SP) additive, Zn, (86.0 wt%) SP, (10.4 wt%) and polyvinylidene fluoride (PVDF) (3.6 wt%) was utilized. For the Zn electrode with ZnO additive, Zn, (86.0 wt%) ZnO, (10.4 wt%) and polyvinylidene fluoride (PVDF) (3.6 wt%) was utilized. For the Zn electrode with Bi_2O_3 additive, Zn, (86.0 wt%) Bi_2O_3, (6.2 wt%) and polyvinylidene fluoride (PVDF) (3.6 wt%) was utilized. For the Zn electrode with all the additives, Zn, (69.4 wt%) SP, (10.4 wt%) ZnO, (10.4 wt%) Bi_2O_3, (6.2 wt%) and polyvinylidene fluoride (PVDF) (3.6 wt%) was utilized. For the Ag electrode, Ag_2O (Alfa Aesar) (80.0 wt%), SP (12.0 wt%), and polyvinylidene fluoride (PVDF) (8.0 wt%) was utilized.

Cell fabrication: All inks were prepared by first, preparing polyvinylidene fluoride (PVDF) solution. PVDF solution is made with dissolving 1 g of PVDF (MTI, EQ-Lib-PVDF) in 10 ml of n-methyl-2-pyrrolidone (NMP) (MTI EQ-Lib-NMP). The PVDF was dissolved over night after vortex mixing and sonication. Then the appropriate amount of PVDF solution was added to the composite powder. The mass ratio of the composite powder and the PVDF is illustrated in supplementary information. The active electrode area was 0.7 cm X 0.9 cm and the distance between the electrodes were kept at 2 mm. Electrode patterns were designed in AutoCAD (Autodesk, San Rafael, CA) and outsourced for fabrication on stainless steel through-hole 12 inch framed stencils (Metal Etch Services, San Marcos, CA). A conductive carbon ink (ERCON E3449) was printed

as a carbon based current collector layer on a polyethylene terephthalate (PET) film. On the current collector layer, the respective electrodes were printed. The printings were performed employing an MPM-SPM semiautomatic screen printer (Speedline Technologies, Franklin, MA). For the three-electrode cell electrochemical experiments, the Zn electrode was taped to a glass slide in between two strips of Zn foils (Sigma-Aldrich 356018). The two strips of Zn foils were utilized as a counter electrode and a reference electrode. Then the gel based electrolyte was prepared with polyacrylic acid. [154] The electrolyte was extruded onto the three-electrodes via syringe.

Electrochemical tests: The electrochemical tests were conducted with Arbin electrochemical cycler channels. All the electrochemical cycling tests were conducted with galvanostatic discharge at 4 mA cm^{-2} current density and constant current constant voltage charge at 2 mA cm^{-2} current density and constant voltage hold for 20 mins at -0.3 V vs. Zn/Zn^{2+} for three-electrode cells and 2.05 V vs. Zn/Zn^{2+} for a full-cell. The three-electrode cells were cycled in -0.3 - 0.4 V Zn/Zn^{2+} range and the full-cell is cycled in 0.8 - 2.05 V Zn/Zn^{2+}. The three-electrode cells were cycled with a capacity limit of 1 mAh cm^{-2}.

PXRD: Pristine sample is the Zn + Bi_2O_3 electrode. The soaked sample is the pristine sample soaked in electrolyte for the same time as oxidized sample (45 minutes). The oxidized sample is the pristine sample after electrochemical oxidation (discharge). Both the soaked sample and the oxidized sample were washed with running D.I. water and soaked in the D.I. water overnight. Upon washing, the electrode was dried in 60 ℃ for 3 hours. All the PXRD data were collected at ambient temperature on a Bruker D8

Advance diffractometer at 40 kV, 40 mA for Cu K_α (λ = 1.5418 Å), with a scan speed of 1 s/step, a step size of 0.05° in 2θ, and a 2θ range of ~10-80°.

Raman spectroscopy: The Raman samples were prepared the same way as the PXRD samples. The Raman spectra were taken with Renishaw InVia Raman microscope, with the laser excitation source of 514 nm, the magnification of 20x, the power of 0.1%, and three accumulations of 30 seconds. For the oxidized sample, ten different spots were examined to confirm the consistent results.

Scanning electron microscopy/energy dispersive X-ray spectroscopy (SEM/EDS): The SEM/EDX samples were prepared the same way as the PXRD samples. After drying, the electrodes were scrapped off from the PET substrate and ground in agate mortar and pestle. The electrode powder was then loaded onto a SEM holder with a carbon adhesive tape. The images and the EDS mapping were taken using 10 kV energy source using the FEI/Phillips XL30 ESEM.

X-ray photoelectron spectroscopy (XPS): The electrode samples were prepared in the same way as the PXRD samples. Then the electrodes were adhered to a Si wafer with carbon tape. The baseline powders were also adhered to a Si wafer with carbon tape. XPS was performed using a Kratos AXIS Supra with Al anode source operated at 15 kV. The chamber pressure was $<10^{-8}$ Torr during all measurements. High resolution spectra were calibrated using the hydrocarbon C1s peak at 284.8 eV. Fitting was performed using CasaXPS software using a Shirley-type background.

5.3. Results

The three-electrode system of various Zn cells was electrochemically cycled (**Figure 5.2**). When the electrode only contains Zn, the cell cycled for only 8 times with a small capacity, followed by a rapid capacity failure. With the addition of Super-P (SP), a conductive carbon additive, the capacity retention exponentially decays in the first ten cycles, gradually decreases until 40 cycles, and finally has no capacity after 50 cycles. By including ZnO, the electrode cycles for only two times and outputs no capacity. When added with Bi_2O_3, the capacity exponentially decays for the first three cycles but increases back to 1 mAh cm^{-2} over the next 12 cycles. This Zn electrode with Bi_2O_3 additive is referred to as the Bi_2O_3 electrode. With the addition of all three additives, the capacity remains at 1 mAh cm^{-2} for at least 50 cycles. Bi_2O_3 compared to SP, increases in capacity after the exponential decay and after 15 cycles, the capacity retention stays mostly at 1 mAh cm^{-2}. Although adding all three additives improves the capacity retention, it is worthwhile to understand the role of Bi_2O_3 to form strategies to further enhance the rechargeability.

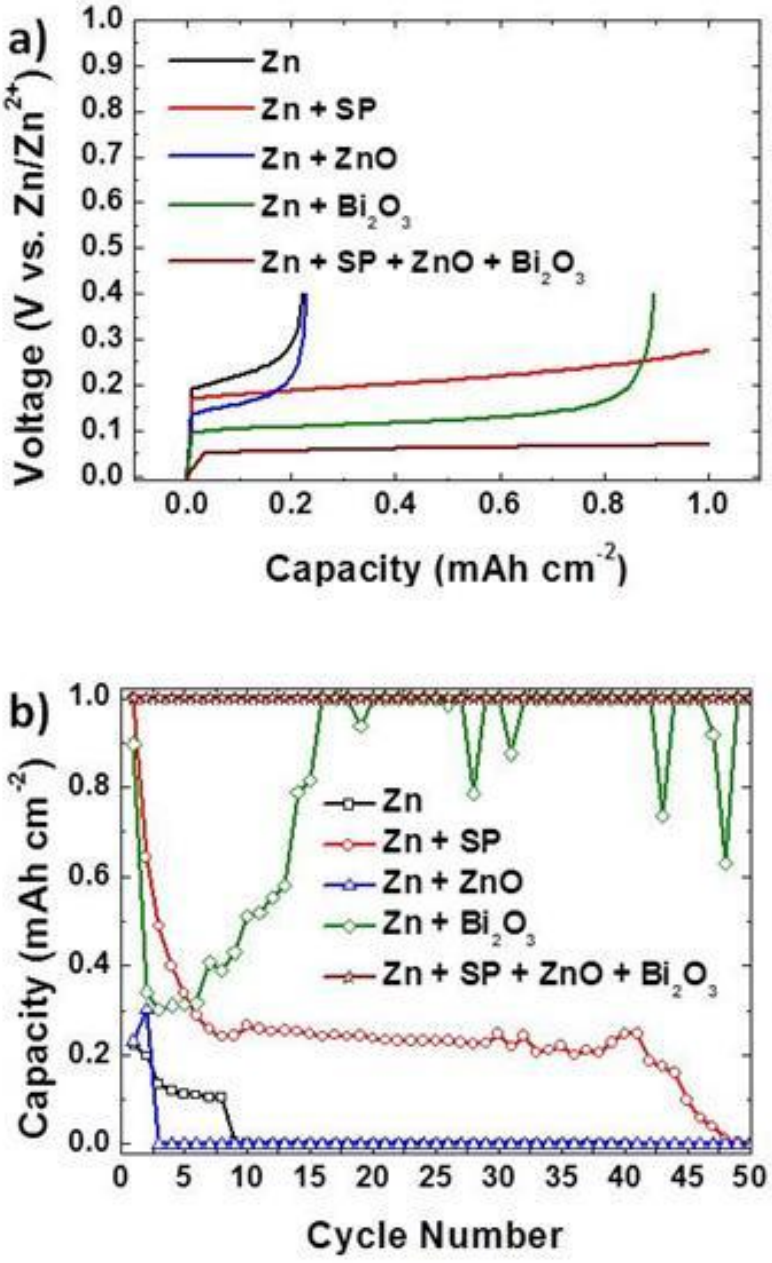

Figure 5.2. a) First discharge voltage profile and b) discharge cycle retention of various Zn electrode electrochemically cycled in a three-electrode cell. All electrodes contain PVDF as the polymer binder but PVDF is omitted for clarity. All electrodes are cycled at current density of 4 mA cm^{-2} and a capacity limit of 1 mAh cm^{-2}.

Since the Zn oxidizes to form ZnO crystals, PXRD of the Bi_2O_3 electrode is obtained at various states (**Figure 5.3**). In the pristine electrode, there are clear reflections from both Zn metal and Bi_2O_3. After being soaked in the electrolyte, the Bi_2O_3 reflections disappear, but reflections corresponding to Bi metal appear. To confirm the absence of Bi_2O_3 reflections, same mass amount of Zn and Bi_2O_3 is mixed and soaked in the electrolyte. It shows the absence of Bi_2O_3 and Bi metal-like reflections (**Figure 5.4**). The Bi_2O_3 is reduced without electrochemical bias. The Zn and Bi_2O_3 particles separately in the electrolyte do not form a new crystal phase (**Figure 5.5 - 5.7**). A new phase is only formed when Zn is present with the Bi_2O_3 in the electrolyte.

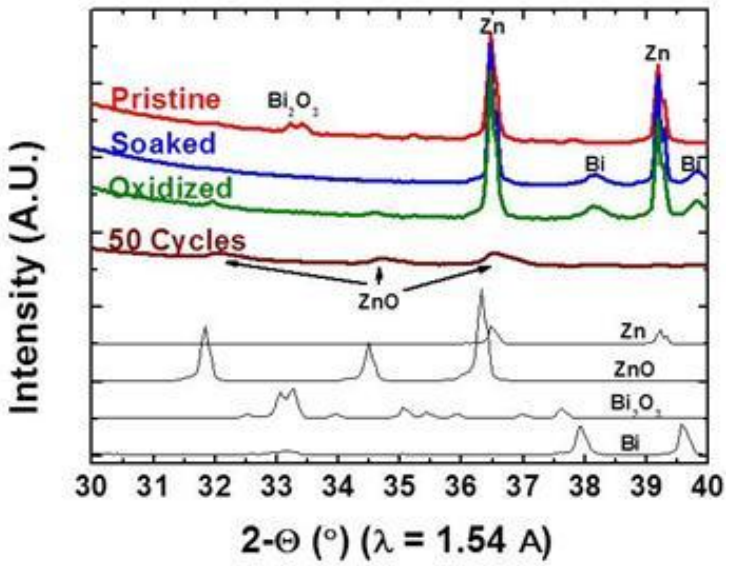

Figure 5.3. PXRD of the Bi_2O_3 electrode at various states in color and raw materials in black. The pristine sample is the Bi_2O_3 electrode after curing. The soaked sample is the Bi_2O_3 electrode after soaking in the electrolyte. The oxidized sample is the Bi_2O_3 electrode after first electrochemical oxidation or discharge.

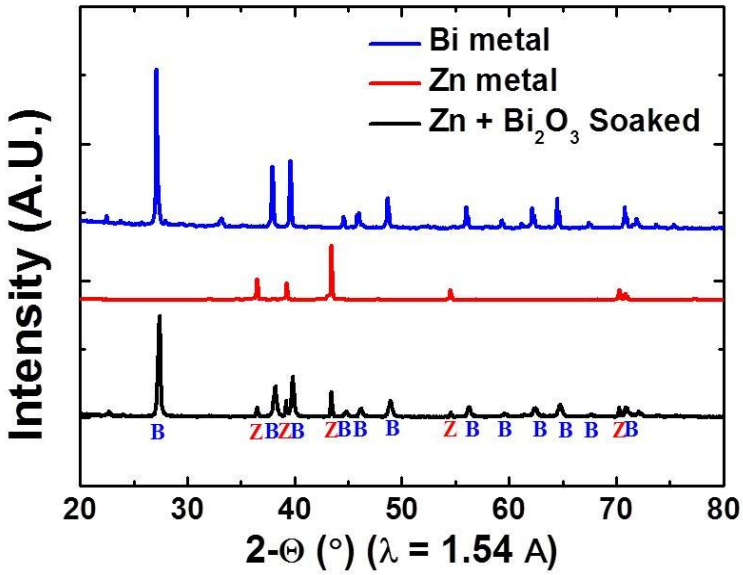

Figure 5.4: Same mass of Zn and Bi_2O_3 particles are mixed and soaked in the electrolyte. PXRD is obtained after soaking, the Bi_2O_3 reflections are completely vanished and only Zn and Bi metal reflections are present.

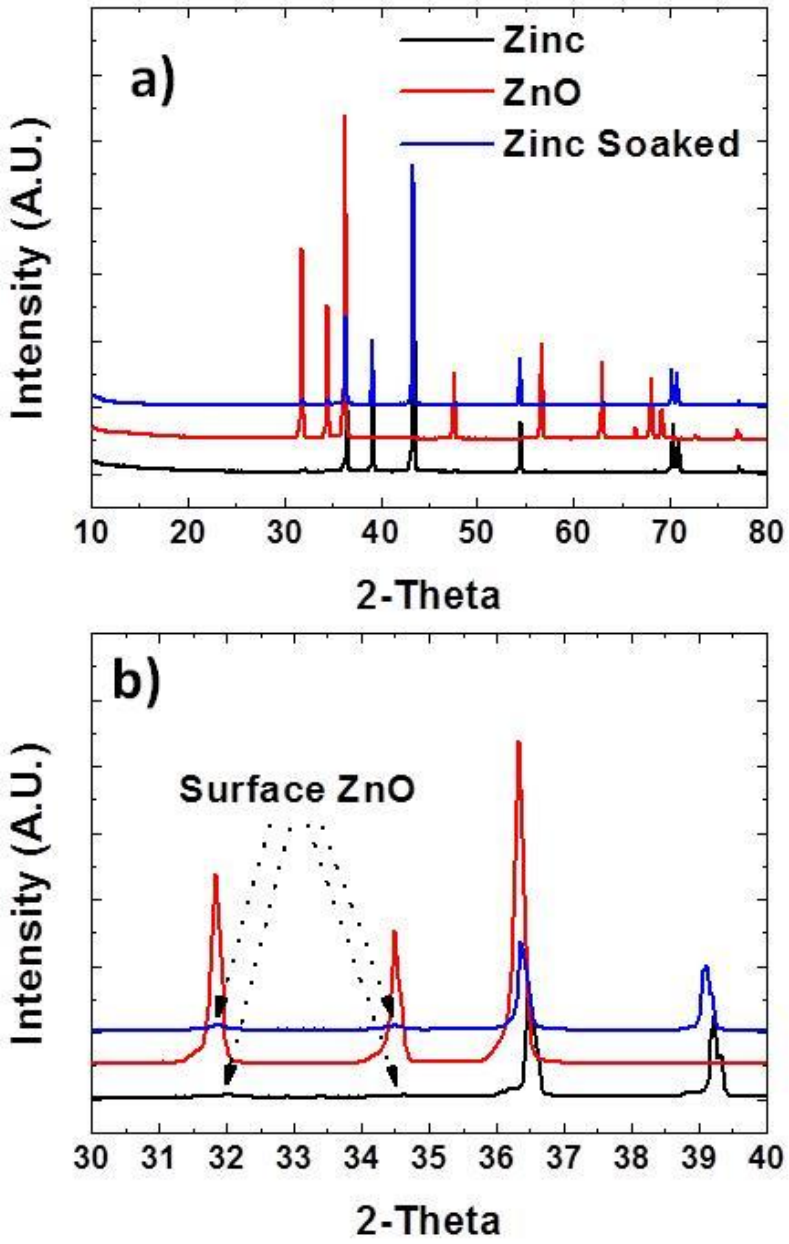

Figure 5.5. a) Wide range and d) narrow range of PXRD of Zn particle soaked in the electrolyte. The electrode samples contain PVDF polymer binder.

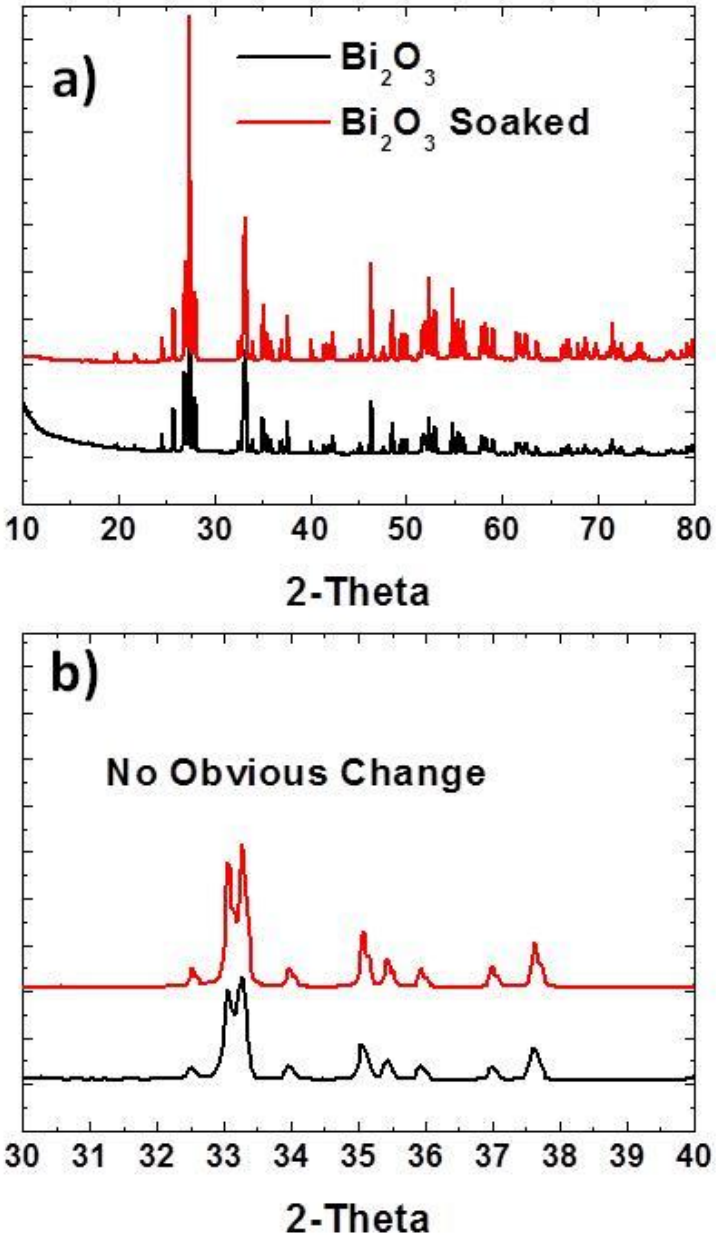

Figure 5.6. a) Wide range and b) narrow range of PXRD of Bi_2O_3 particle soaked in the electrolyte. The electrode samples contain PVDF polymer binder.

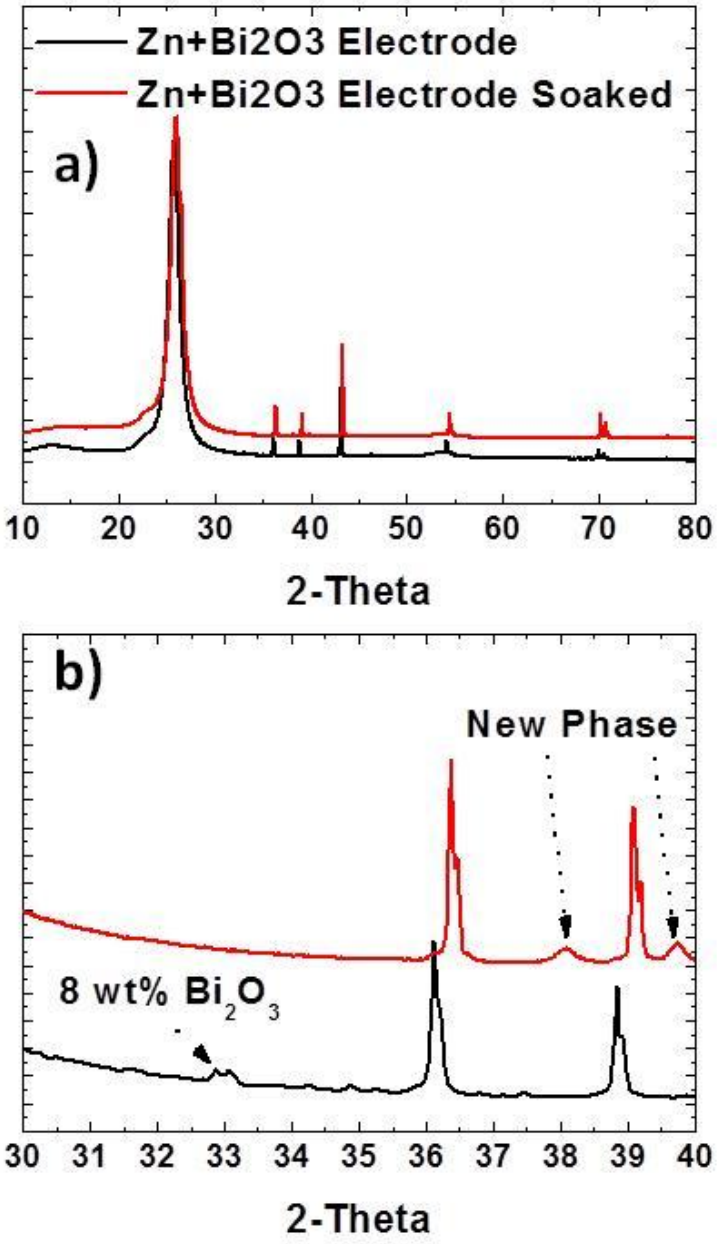

Figure 5.7. a) Wide range and b) narrow range of PXRD of Zn + Bi_2O_3 electrode soaked in the electrolyte. The electrode samples contain PVDF polymer binder.

After 50 cycles, the ZnO reflections become obvious but the Zn and Bi metal-like reflections vanish. This suggests that the Bi metal-like species is actively involved during

the electrochemical cycling, however the ZnO growth is not very clear upon first oxidation. To elucidate the electrochemical reaction that occurs in the Bi_2O_3 electrode, Raman spectra are obtained before and after the electrochemical oxidation reaction (**Figure 5.8**). Before the electrochemical reaction, the pristine electrode only shows the typical Bi_2O_3 vibration modes. Upon oxidation reaction, the Bi_2O_3 vibration modes disappear, similar to the Bi_2O_3 reflections in PXRD, and only two broad peaks appear near 440 cm^{-1} (E_2 (High) mode) and 565 cm^{-1} (A_1 (longitudinal optical or LO) mode). These two peaks indicate ZnO formation. The E_2 (High) mode is typically an intense and sharp signal originated from the vibrational motion of oxygen atoms in the ZnO.[155] The low intensity and the broadening imply a disorder in the crystal structure.[155, 156] The disorder can be a result of lattice mismatching from relaxation, reconstruction, structural imperfection, and adsorbed impurities.[157] A_1 (LO) mode is typically a low intensity signal from c-face ZnO. The enhancement of this signal is due to the Raman resonance effect.[158] The observed resonance effect is most likely due to ZnO that is not nucleated as an isolated compound but rather deposited on a conductive substrate/surface. The Raman signal may be contributed by the passivation ZnO layer on the Zn metal or on the Bi metal-like species. Further experiments are conducted to identify the exact location of the ZnO.

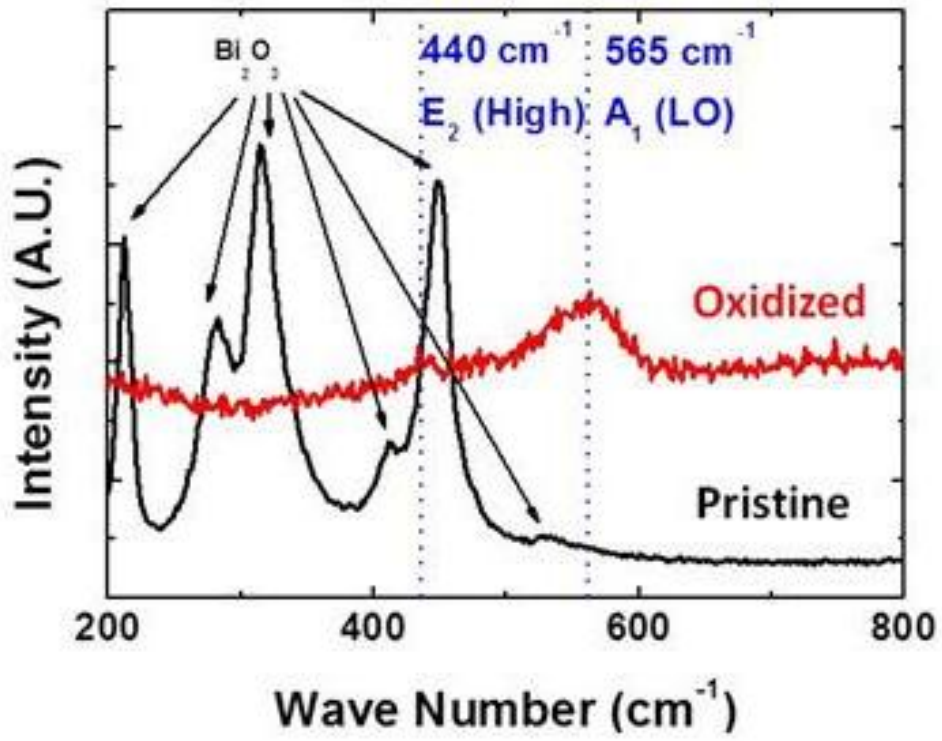

Figure 5.8. Raman spectra of the Bi_2O_3 electrode at pristine and oxidized (first discharged). The pristine sample is the Bi_2O_3 electrode after curing. The soaked sample is the Bi_2O_3 electrode after soaking in the electrolyte. The oxidized sample is the Bi_2O_3 electrode after first electrochemical oxidation or discharge.

The Raman spectra suggests that the ZnO is formed on a conductive surface, yet it is not clear whether the ZnO observed in Raman is a passivation layer on the Zn metal or on the surface of the bismuth species. SEM images along with the EDS mapping are collected after oxidation. Pristine Bi_2O_3 particles are about 2 μm in size. EDS mapping of a 2 μm particle shows that this particle is composed of both zinc atoms and bismuth atoms (**Figure 5.9**). This mapping suggests that the ZnO is deposited on the surface of the bismuth species. Furthermore, EDS mapping of a particle after 50 cycles also exhibit

both Zn and Bi (**Figure 5.10**). Unlike after the first oxidation, this particle is about 8 μm and the concentration of the Zn is much higher than that of Bi. The growth of the particle size and the change in atomic concentration clearly indicate that the ZnO continues to grow on the surface of the bismuth species over prolonged cycles.

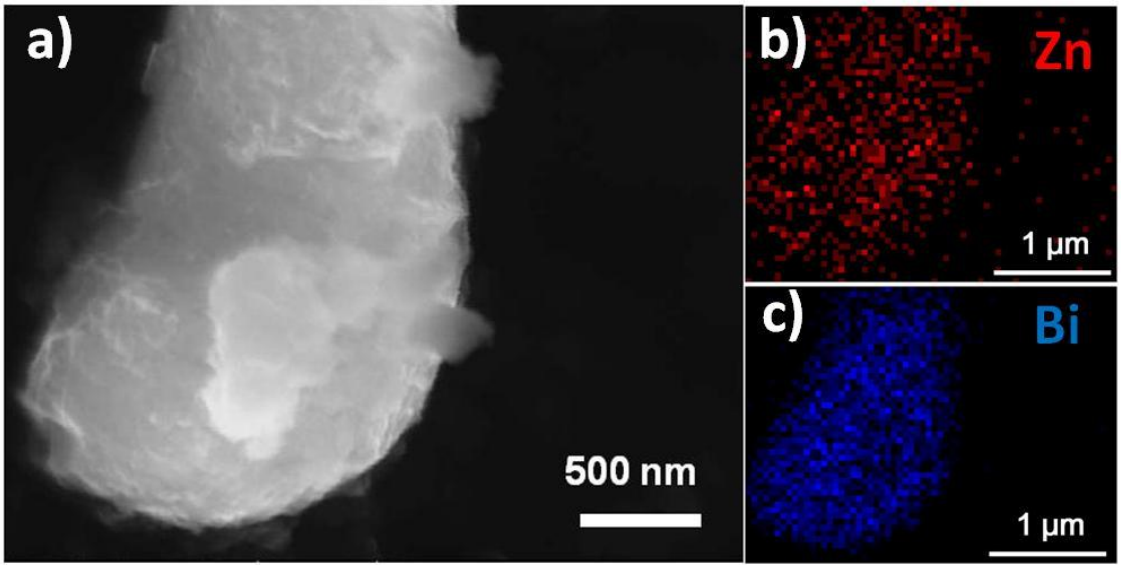

Figure 5.9. a) SEM image of the bismuth species after oxidation. b) EDS mapping of Zn $K\alpha_1$ and c) Bi $M\alpha_1$. The EDS mapping is performed on the same particle as the SEM image (a).

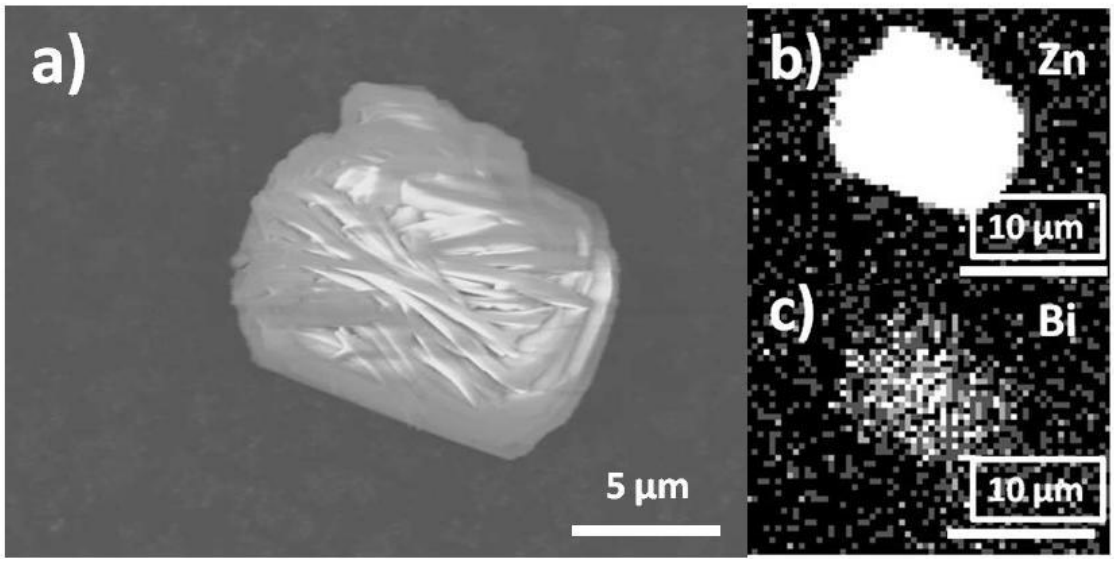

Figure 5.10: a) SEM image of the bismuth species after 50 cycles. b) EDS mapping of Zn $K\alpha_1$ and c) Bi $M\alpha_1$. The EDS mapping is performed on the same particle as the SEM image (a).

To confirm the ZnO deposition on the bismuth species, XPS is collected for the pristine, electrolyte soaked, and oxidized electrode. The survey scans are provided to ensure the absence of electrolyte salt or other impurities (**Figure 5.11**). The pristine electrode contains Zn metal and Bi_2O_3 with respective surface passivation layers (**Figure 5.12**).[159-161] After being soaked in electrolyte, the Zn metal peak shifts to lower binding energy indicative of the Zn alloying.[162] In the Bi 4f spectra, the Bi_2O_5 passivation layer disappears and a Bi metal peak appears. The absence of Bi_2O_5 and the presence of Bi metal support the hypothesis that the Zn reduces the bismuth species. Furthermore, compared to the Bi metal baseline spectrum, the spectrum of the soaked sample is much broader. This is likely due to the Bi-Zn alloying.

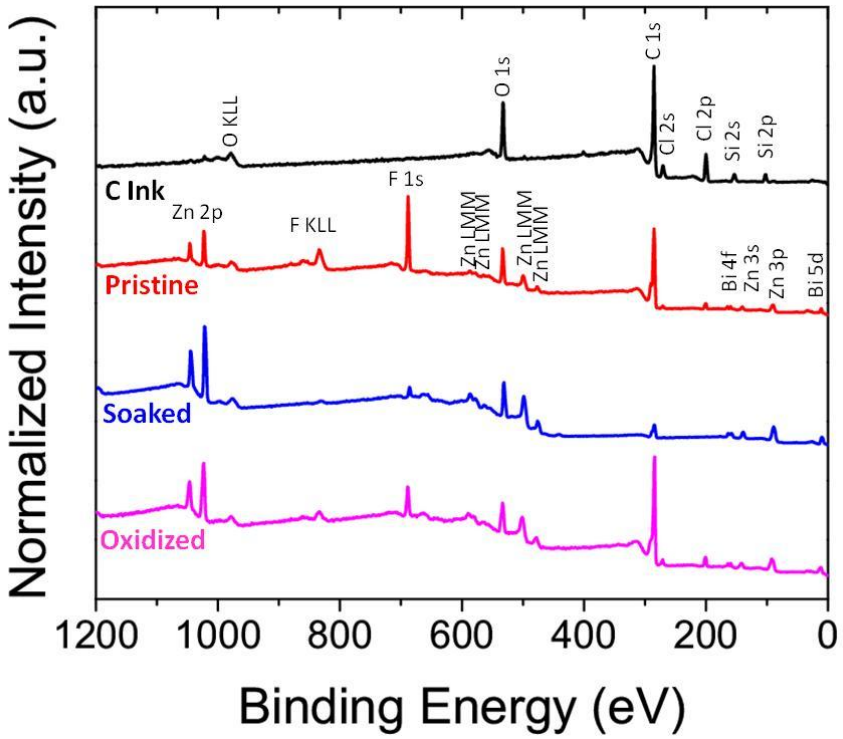

Figure 5.11. Survey scans of the Bi_2O_3 electrode. All the samples are in the form of electrodes printed on a PET substrate. The pristine sample is the Bi_2O_3 electrode after curing. The soaked sample is the Bi_2O_3 electrode after soaking in the electrolyte. The oxidized sample is the Bi_2O_3 electrode after first electrochemical oxidation or discharge.

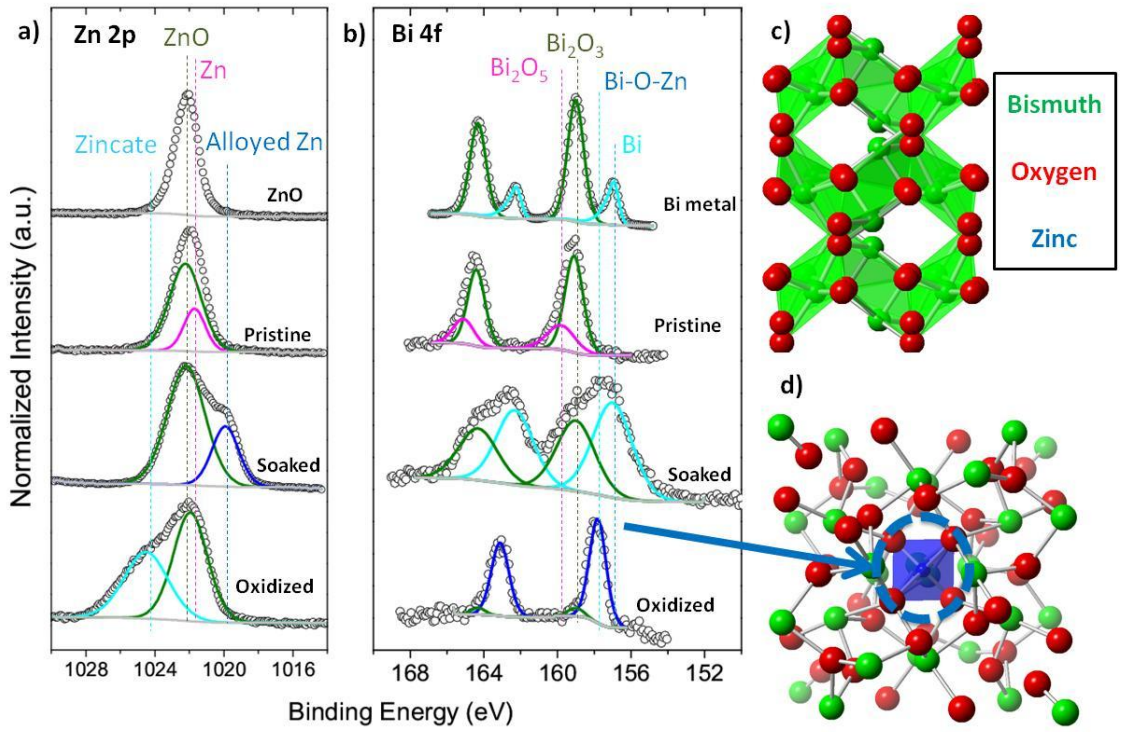

Figure 5.12. a) Zn 2p and b) Bi 4f XPS of the Bi_2O_3 electrode at various states along with ZnO and Bi metal as baseline materials. Crystal structure of c) α-Bi_2O_3 and d) $Bi_{38}ZnO_{58}$. Green: Bismuth, Red: Oxygen, and Blue: Zinc. In d) $Bi_{38}ZnO_{58}$, the Zn site is partially occupied by Zn and Bi.

Upon oxidation, the Zn alloy peak disappears and zincate peak appears. This suggests that the alloyed Zn is electrochemically active to form zincate ion. As mentioned earlier, the zincate ion is soluble in aqueous electrolyte. Thus the formation of zincate ion leads the active material loss because the ZnO is developed in the electrolyte disconnected from the electrode. However, the presence of zincate peak implies that the zincate ion is well bound to the electrode even after the rigorous washing. In the Bi 4f spectra, upon oxidation, the Bi metal peak disappears and a new peak appears in between

Bi_2O_3 and Bi metal peaks. Since the Bi^{2+} is unstable and undergoes disproportionation reaction, this new peak most likely originates from some Bi^{3+}/Zn^{2+} compound.[163]

It is clear that Bi_2O_3 provides the vital assistance in prolonging the cyclability of the Zn anode. However, the Bi_2O_3 added electrode suffers from a rapid decay in the retention during the first few cycles. By adding the three additives (Bi_2O_3, SP and ZnO), the cycling performance of the three-electrode cell noticeably improves (**Figure 5.2.b**). ZnO is required to match the extra charging capacity of the Ag_2O cathode.[20] With this anode, a Zn-Ag full-cell is constructed (**Figure 5.13**). The Zn anode behaves as the Zn/Zn^{2+} redox couple and the Ag cathode behaves as the AgO/Ag_2O and Ag_2O/Ag redox couples. There are largely two plateaus in both charge and discharge corresponding to these two redox couples. First discharge curve dominantly consists of Ag_2O/Ag redox behavior because at the beginning, Ag electrode mostly contains Ag_2O. The full-cell is fully functional even with the high discharging current of 4 mA cm^{-2}. To the best of our knowledge, among Zn-based printable batteries, 4 mA cm^{-2} of discharge current density in this work is among the highest[20, 30-35] and for printable batteries, the highest current density to date is 1.4 mA cm^{-2}.[20] During discharge, a consistent high power output of about 5 mW cm^{-2} is achieved. The capacity of the full-cell is above 1.2 mAh cm^{-2} (**Figure 5.13**). Gaikwad et al. achieved about 3.5 mAh cm^{-2}, but their battery is not rechargeable.[164] Among the rechargeable printable batteries, the highest capacity is 1.2 mAh cm^{-2}.[20] Although the cycling retention degrades only after 6 cycles, this is attributed to the decay in the cathode (**Figure 5.14**). The bare Zn anode's poor cycling performance

originates from the large crystal transformation during the electrochemical reaction and the Ag cathode also undergoes a significant crystal transformation.[20]

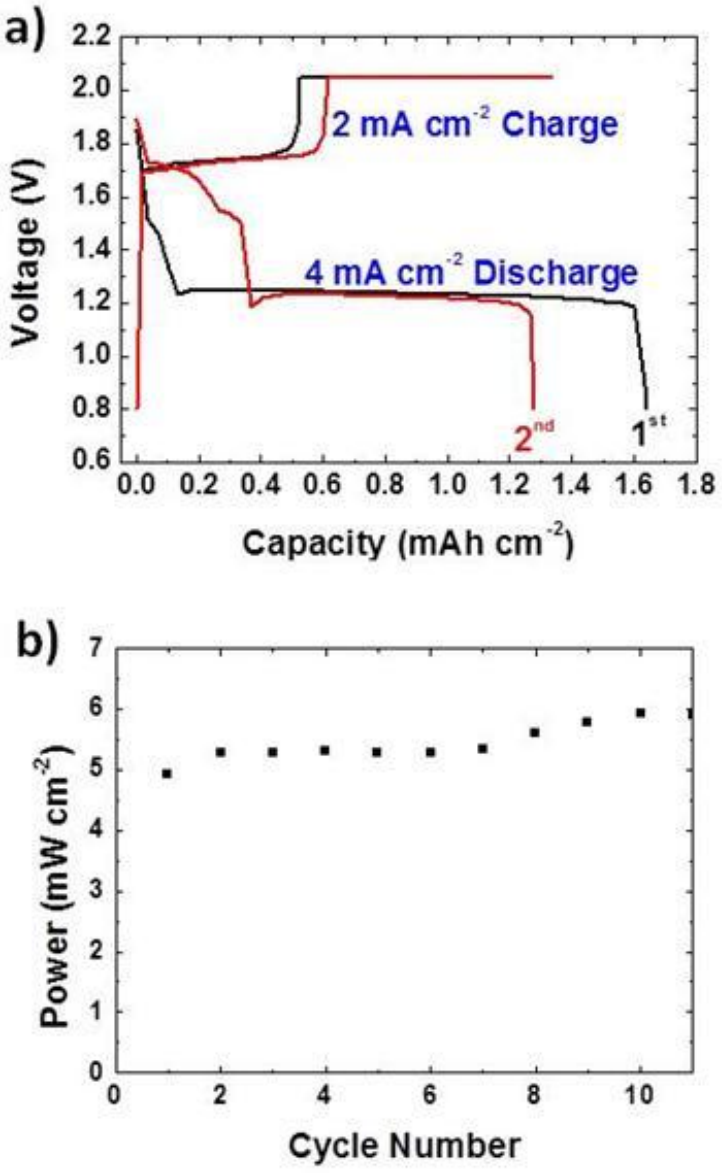

Figure 5.13. a) Voltage profile and b) power density of Zn-Ag full-cell battery performance with all the additives added in the Zn anode. The full-cell is cycled with current density at 4 mA cm^{-2} without a capacity limit.

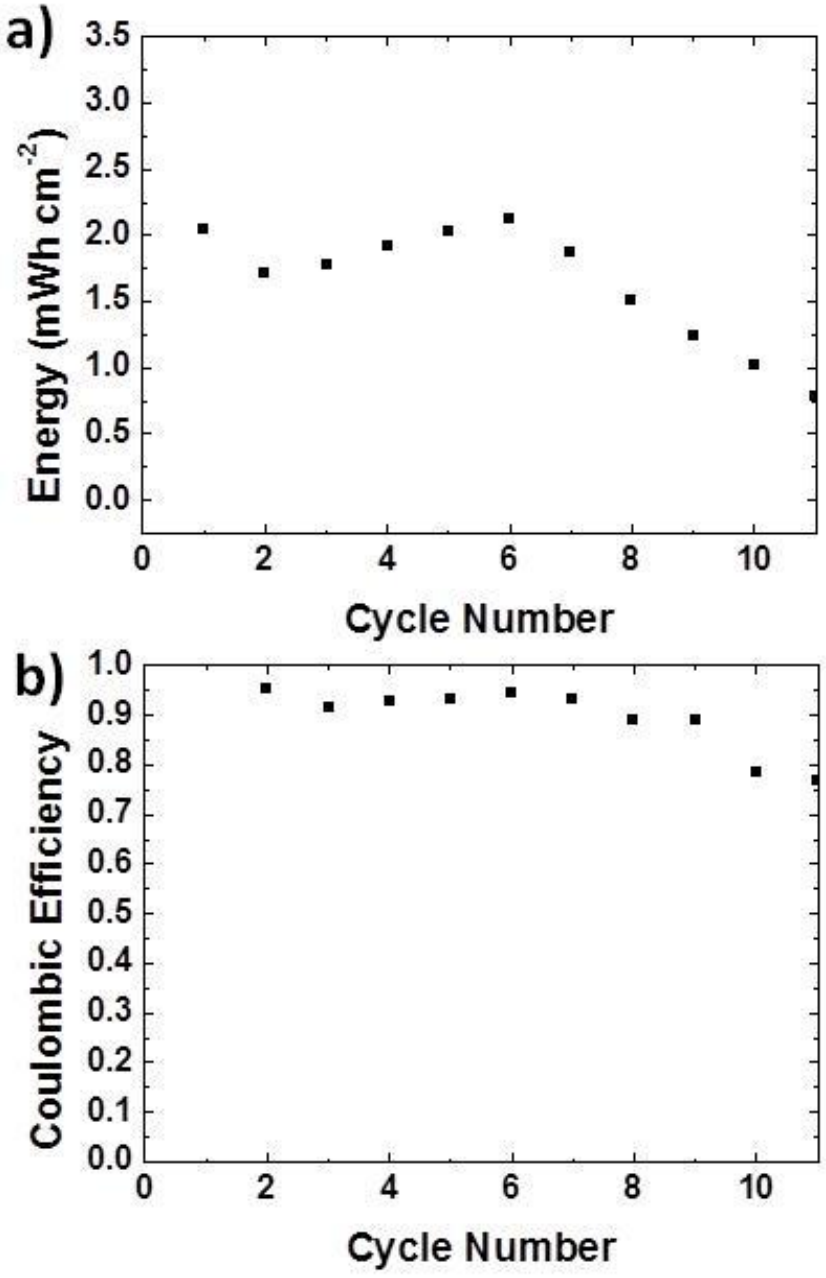

Figure 5.14. a) Energy density and b) coulombic efficiency of Zn-Ag full-cell battery performance with all the additives added in the Zn anode. The full-cell is cycled with current density at 4 mA cm^{-2} without a capacity limit.

5.4. Discussion

The Zn particles are conductive itself, yet when Zn starts to oxidize, the Zn surface gets etched away, losing the electrical connections and eventually no capacity is given off, as shown in **Figure 5.2**. Conductive additive is needed even though the Zn particles are conductive. Utilizing Zn plates bypasses such issue; however, Zn plates suffer from dendritic deposition of ZnO.[165] It is reported that the composite electrodes exhibit higher energy density due to its higher surface area and porosity compared to those of the plates.[166, 167] Both SP and the Bi_2O_3 are conductive additives and they provide electrical connection. Compared to Bi_2O_3, the SP electrode decays in capacity more slowly. This is attributable to the fact that SP has much greater surface area than Bi_2O_3, making it capable of maintaining a better network of electrical connection. However, the SP electrode eventually uses up the electrical network and does not give off capacity. The Bi_2O_3 electrode has low retention between first and 15^{th} cycle. Given the high rate cycling, the low retention of the Bi_2O_3 electrode is most likely due to the delay in the relaxation of zincate ions into ZnO. Lastly, ZnO additive is insulating. Although it helps giving extra capacity at the second cycle by reducing to Zn metal during the first reduction/charge, it does not allow stable electrical conductivity.

The PXRD and XPS results suggest the reduction of Bi_2O_3 into a Zn-Bi alloy. Although Zn is kinetically stable in aqueous electrolyte, it is not thermodynamically stable because Zn has lower reduction potential compared to hydrogen. Zn anode in aqueous electrolyte oxidizes, which is called self-discharge.[168, 169] Self-discharging can be suppressed by the presence of bismuth species.[168, 169] The amount of H_2 gas evolution is

suppressed with the presence of Bi_2O_3 (**Figure 5.15**). The H_2 gas evolution is the result of water molecule breaking down due to the Zn oxidation and H_2O reduction in other words: self-discharge. Besides the hydrogen, Bi^{3+} also has higher reduction potential than Zn. The Bi^{3+} reduces to form Bi^{2+} or Bi metal to oxidize the Zn and after reducing to Bi^{2+}, the Bi^{2+} undergoes disproportionation reaction to develop Bi metal.[29] Bi metal-like reflections have been formed and reported in the literature.[151]

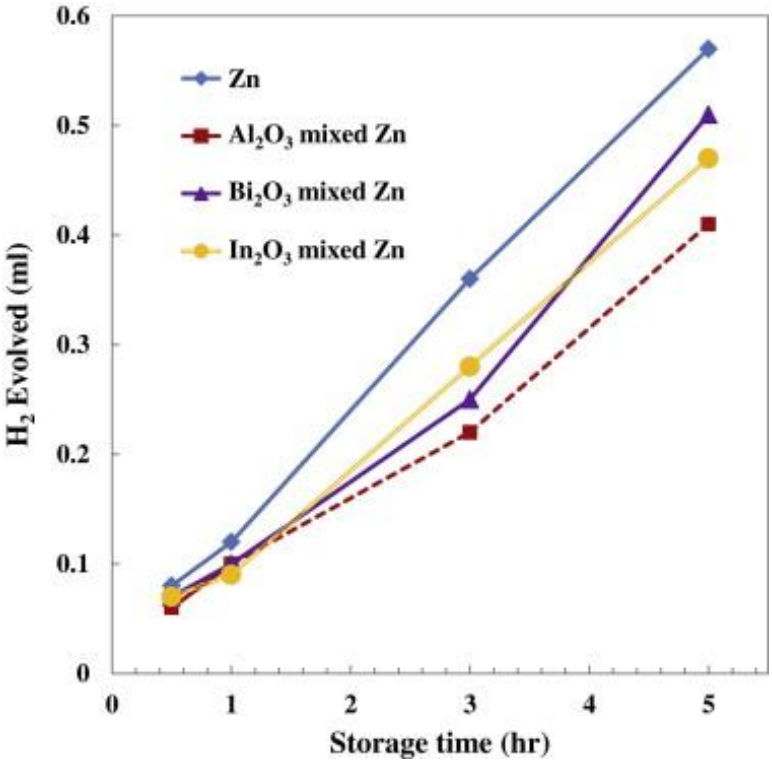

Figure 5.15. Volumetric measurement of hydrogen spontaneously evolved on the surface of Zn gel anode at 60 ℃. [39]

In the XPS results, a Bi^{3+}/Zn^{2+} mixed phase is found. A phase diagram of the Bi_2O_3 and ZnO mixture suggest that there are various mixed compound variations

available (**Figure 5.16**). At the room temperature, monoclinic α-Bi_2O_3 phase is stable and all the Bi^{3+} coordination environments are distorted half-octahedron: [BiO_5E] (E denotes an unshared electron pair) (**Figure 5.17**). At higher temperature, a body-centered cubic (BCC) γ-Bi_2O_3 is the stable phase and some Bi^{3+} coordination environments are tetrahedron: [BiO_4].[41] Furthermore, in the presence of Zn^{2+}, the BCC phase is stable at the room temperature.[170-172] $Bi_{38}ZnO_{58}$, part of the sillenite family, is a BCC phase with the tetrahedron coordination environment. Although it is hard to conclude that $Bi_{38}ZnO_{58}$ is formed, but we can be certain that a new phase with [BiO_4] local bonding has formed.

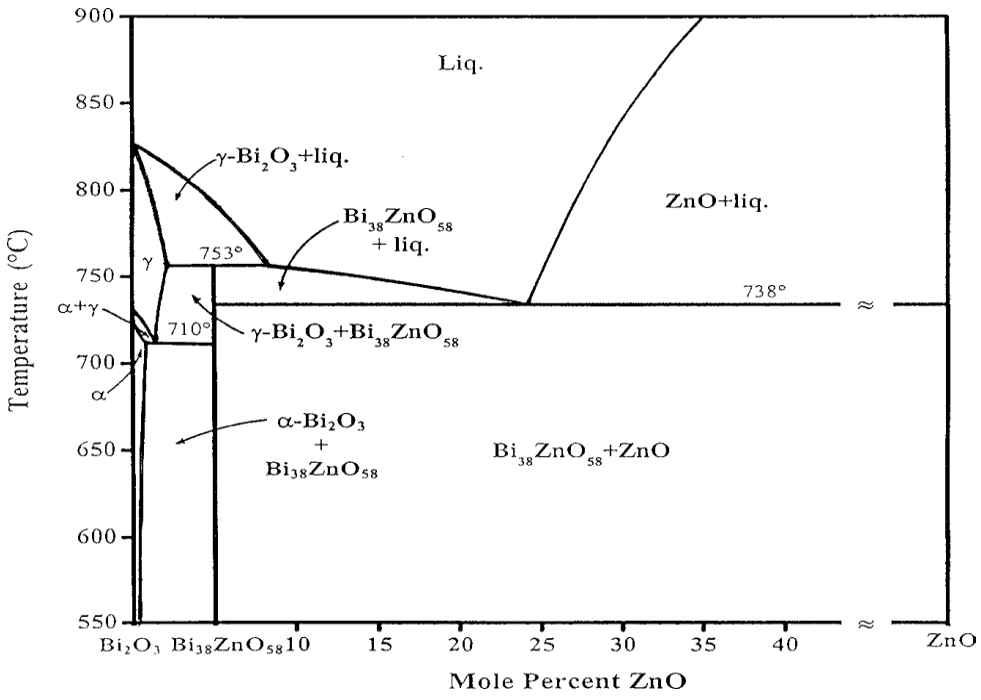

Figure 5.16. Phase diagram of the Bi2O3 and ZnO. [43]

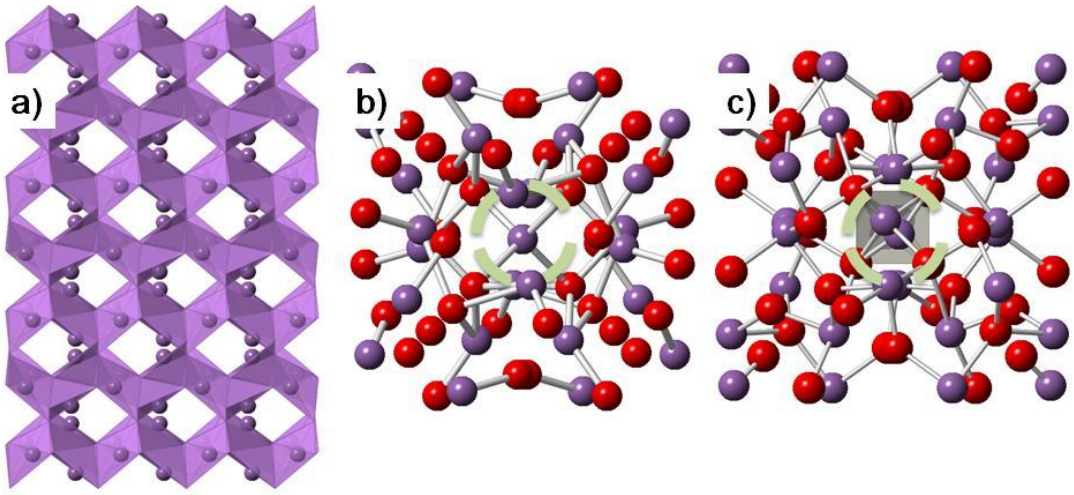

Figure 5.17. Crystal structures of a) α-Bi_2O_3,b) γ-Bi_2O_3, and c) $Bi_{38}ZnO_{58}$. Light purple: bismuth, Red: oxygen, grey: zinc, and dashed circle indicates the site in which the tetrahedral coordination exists.

The improvement of the rechargeability of the Bi_2O_3 electrode over time is related to the deposition of ZnO rather than conductivity. While this work describes various bismuth species involved during the cycling process, the zincate ions deposit on the surface of the bismuth species regardless of the bismuth species. Based on the findings of this study, a possible reaction mechanism is proposed in **Figure 5.18**. Without the Bi_2O_3 additive, the Zn particles in the electrode upon oxidation, form zincate ions. The zincate ions are dissolved into the electrolyte and into ZnO. Since ZnO is not on the electrode where electron pathways are, this electrode is not fully rechargeable. By adding Bi_2O_3, the zincate ions deposit on the surface of the bismuth species and relax into ZnO on the bismuth species, making this electrode rechargeable.

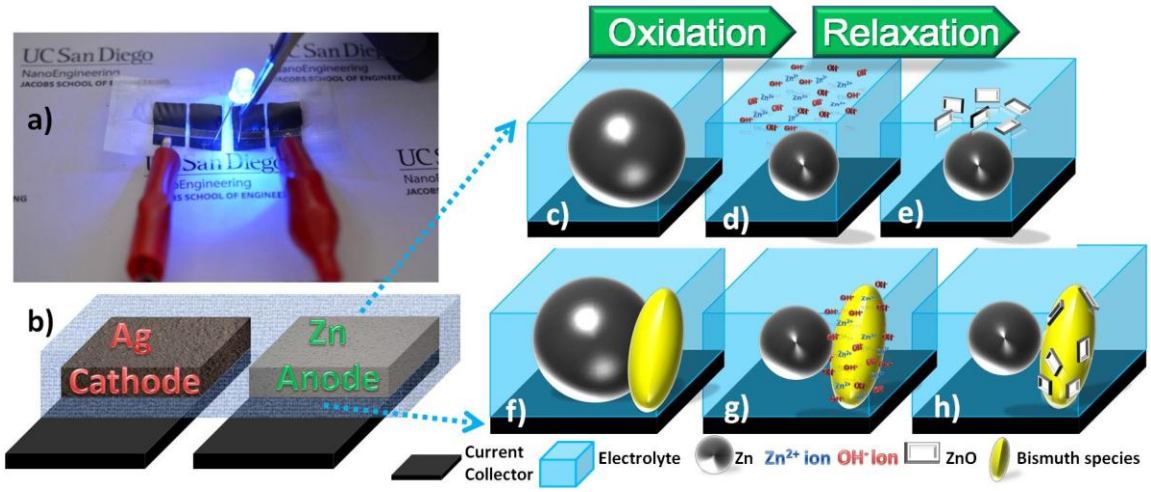

Figure 5.18. a) Two Zn-Ag full-cells lighting up an LED. b) A conceptual image illustrating the full-cell configuration. Schematics illustrating possible reaction mechanisms for the Zn electrode (c-e) and the Zn with Bi_2O_3 additive electrode (f-h). In the scheme, the phase transformation of bismuth species, PVDF polymer binder, and polyurethane sealing are omitted for clarity.

5.5. Conclusion

Various additives are mixed into the Zn electrodes and their electrochemical performances are presented. Among the additives, Bi_2O_3 is the critical additive in improving the cycle life of the Zn electrode. Through carefully characterizing the Bi_2O_3 containing Zn electrode, we gained the comprehensive mechanistic role of Bi_2O_3. Firstly, upon oxidation, the zincate ions are formed and deposited on the surface of the bismuth species. Secondly, the zincate ions relax into ZnO on the bismuth species. The electrode is fully rechargeable because the electrical connection is retained for the ZnO. Notable additional phenomena were discovered in this work. The Zn-Bi alloy and the new Bi^{3+}/Zn^{2+} mixed oxide phases were found. Although the exact crystal structure of these phases is unknown, the identification of the phases can be achieved through series of

computational modeling and experimental investigation. Nevertheless, the benefit of adding Bi_2O_3 is previously assumed to be in conductivity, however this work confirms that the vital role of Bi_2O_3 is providing surfaces for the ZnO to deposit. This work clearly defines the mechanistic role of Bi_2O_3 in the Zn electrode. The findings in this work can potentially help gaining a better understanding on the large crystal transformation systems such as conversion systems in LIBs.

Chapter 5, in part, is a reprint of the material “Relaxation of ZnO on Bismuth Species Towards Rechargeable Zn-based Aqueous Battery” as it appears in the Physical Chemistry Chemical Physics, Jaewook Shin, R. J.-M. You, J. Lee, R. Kumar, L. Yin, J. Wang, and Y. S. Meng,, 2016, accepted manuscript. The dissertation author was the co-primary investigator and author of this paper.

Chapter 6. Selecting functional additives for composite electrode

6.1 Introduction

It is clear that most of the active electrode materials cannot serve as a perfect electrode alone.[173, 174] First of all, to make a film of electrode out of powder of active materials require binders to bind the particles together. Many active electrode materials lack electrical conductivity.[175-179] As a common practice, the conductive carbon additive is added into the active material and binder mix. Aside from these common issues, there are material specific bottlenecks, especially in the conversion materials. To solve the material specific bottlenecks, additional functionality must be added.

As mentioned in chapter 5 of this dissertation, Zn, undergoes a zincate dissolution. In the literature some solutions exist to solve such issue.[180] A custom made separator composed of nylon non-woven cloth coated with poly(vinyl alcohol) containing boric acid is utilized as a Zn-Ni battery.[181] This separator is able to block the zincate ions from diffusing from the Zn electrode to the Ni electrode (**Figure 6.1**). In the materials level, there are several ways to achieve functionality in an electrode: composite additive, electrolyte additive, coating, doping, etc. However, many methods require high cost fabrication techniques or extra fabrication steps.

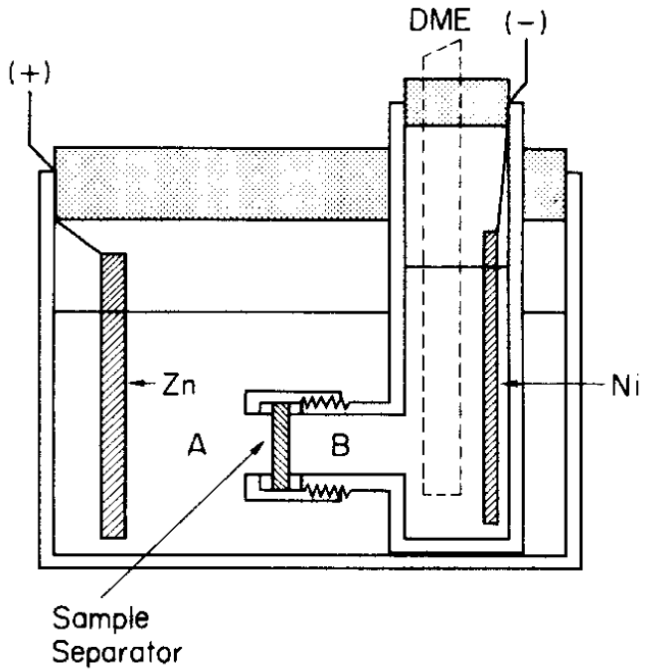

Figure 6.1. Electrolytic cell to determine Zn^{2+} penetration quantity: A: 8M KOH + 0.5M ZnO (initial), B: 8M KOH.[181]

To accomplish a low cost electrode, the fabrication cost must be low and method simple. One of the cheapest and simplest method to add functionality is by adding composite additives.[173, 174] Most of the composite electrodes are already being mixed with carbon additive. The composite additive method only requires that one add the additive during the preexisting mixing step. However, even though the fabrication process is simple, many materials still suffer from the unknown solution to their respective bottlenecks. Especially, with all conversion type materials, dissolution of the active material is a major issue.[182] As described in earlier chapters, a functional additive that can absorb the active material and maintain the electrical connection is one of the major keys to solving the issue. In many cases of conversion type materials, the optimum functional additive is not clear. Here, we propose a simple and quick experiment to screen various

composite additive candidates for the conversion type materials.

6.2. Experimental details

All reagents are used without further purification.

Zn^{2+} deposition on Bi_2O_3: 0.6 g of Bi_2O_3 (Alfa Aesar) was immersed in a 12 ml of aqueous 6 M $Zn(NO_3)_2$ (Sigma Aldrich) solution. After soaking overnight, the solute was filtered and washed with copious amount of water. The soaking, filtering, and washing were repeated three times.

Zn^{2+} deposition on Bi: 0.6 g of Bi (Alfa Aesar) was immersed in a 12 ml of aqueous 6 M $Zn(NO_3)_2$ (Sigma Aldrich) solution. After soaking overnight, the solute was filtered and washed with copious amount of water. The soaking, filtering, and washing were repeated three times.

Cu^{2+} deposition on NiO: 0.6 g of NiO (Alfa Aesar) was immersed in a 18 ml of aqueous 0.5 M $Cu(SO_4)$ (Sigma Aldrich) solution. After soaking overnight, the solute was filtered and washed with copious amount of water. The soaking, filtering, and washing were repeated three times.

Mn^{2+} deposition on Bi_2O_3: 0.6 g of Bi_2O_3 (Alfa Aesar) was immersed in a 12 ml of aqueous 2 M $Mn(NO_3)_2$ (Sigma Aldrich) solution. After soaking overnight, the solute was filtered and washed with copious amount of water. The soaking, filtering, and washing were repeated three times.

Scanning electron microscopy/energy dispersive X-ray spectroscopy: The SEM/EDX samples were all powder samples. The powder sample is sprinkled on a strip of carbon adhesive tape and inert air is blown to the tape to remove excess powder. The

images and the EDS mapping were taken using 10 kV energy source using the FEI/Phillips XL30 ESEM.

6.3. Results and discussion

6.3.1. Zn^{2+} deposition on Bi_2O_3

To simulate the presence of Bi_2O_3 particle composite additive in the Zn electrode, the Bi_2O_3 particle is immersed in the Zn^{2+} containing solution. When Zn is oxidized, the zincate ions are dissolved into the electrolyte, Zn^{2+} solution simulates the electrolyte solution after Zn oxidation reaction. From the previous chapter, the Bi_2O_3 allows the zincate ions to adhere on its surface. The morphology of the Bi_2O_3 surface has completely changed after soaking the particles in the Zn^{2+} solution (**Figure 6.2**). The pristine Bi_2O_3 surface is smooth and has about 1 - 2 μm particle size distribution. After the soaking, the surface has became rough with smaller particles surrounding the larger particles. To further confirm the Zn^{2+} deposition on the Bi_2O_3 surface, EDS mapping has been collected (**Figure6.3**). The Bi_2O_3 particle after soaking in 12 ml of aqueous 6M $Zn(NO_3)_2$ solution is used to observe the presence of Bi and Zn. The elemental distribution is homogeneously distributed.

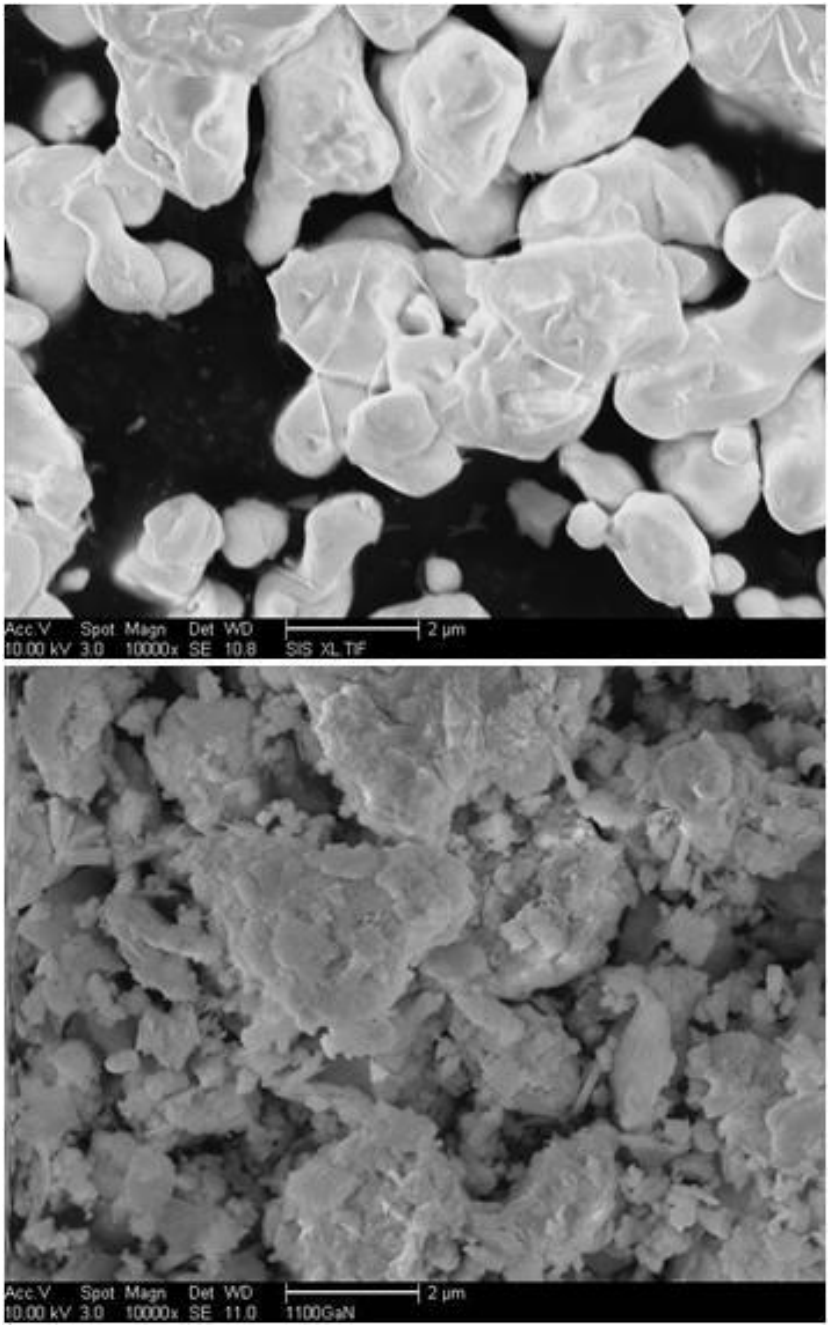

Figure 6.2. SEM images of Top: pristine Bi_2O_3 particle and bottom: Bi_2O_3 particle after soaking in 12 ml of aqueous 6M $Zn(NO_3)_2$ solution.

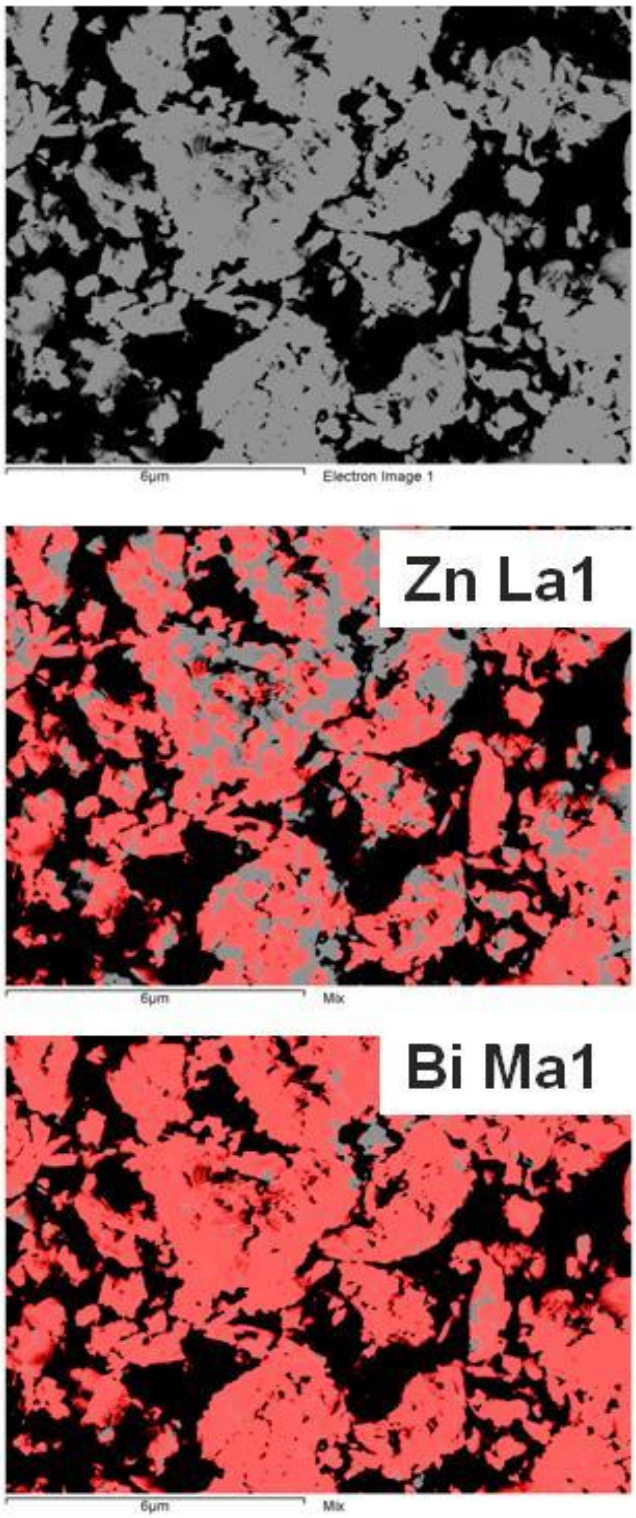

Figure 6.3. Bi_2O_3 particle after soaking in 12 ml Of aqueous 6M $Zn(NO_3)_2$ solution. Top: SEM image of the EDS site. Middle: EDS mapping using the Zn $L_{\alpha 1}$ data. Bottom: EDS mapping using the Bi $M_{\alpha 1}$ data

6.3.2. Zn^{2+} deposition on Bi

In the previous chapter, the Bi_2O_3 additive has shown that it forms Bi metal phase in the presence of Zn metal. To make sure that Bi_2O_3 additive in fact allows the Zn^{2+} deposition, Bi metal is also soaked in the Zn^{2+} containing solution. The morphology of the Bi surface has completely changed after soaking the particles in the Zn^{2+} solution (**Figure 6.4**). The pristine Bi surface is smooth and has about 20 - 30 μm particle size distribution. After the soaking, the surface has become rough with smaller particles surrounding the larger particles. To further confirm the Zn^{2+} deposition on the Bi surface, EDS mapping has been collected (**Figure6.5**). The Bi particle after soaking in 12 ml of aqueous 6M $Zn(NO_3)_2$ solution is used to observe the presence of Bi and Zn. The elemental distribution is homogeneously distributed.

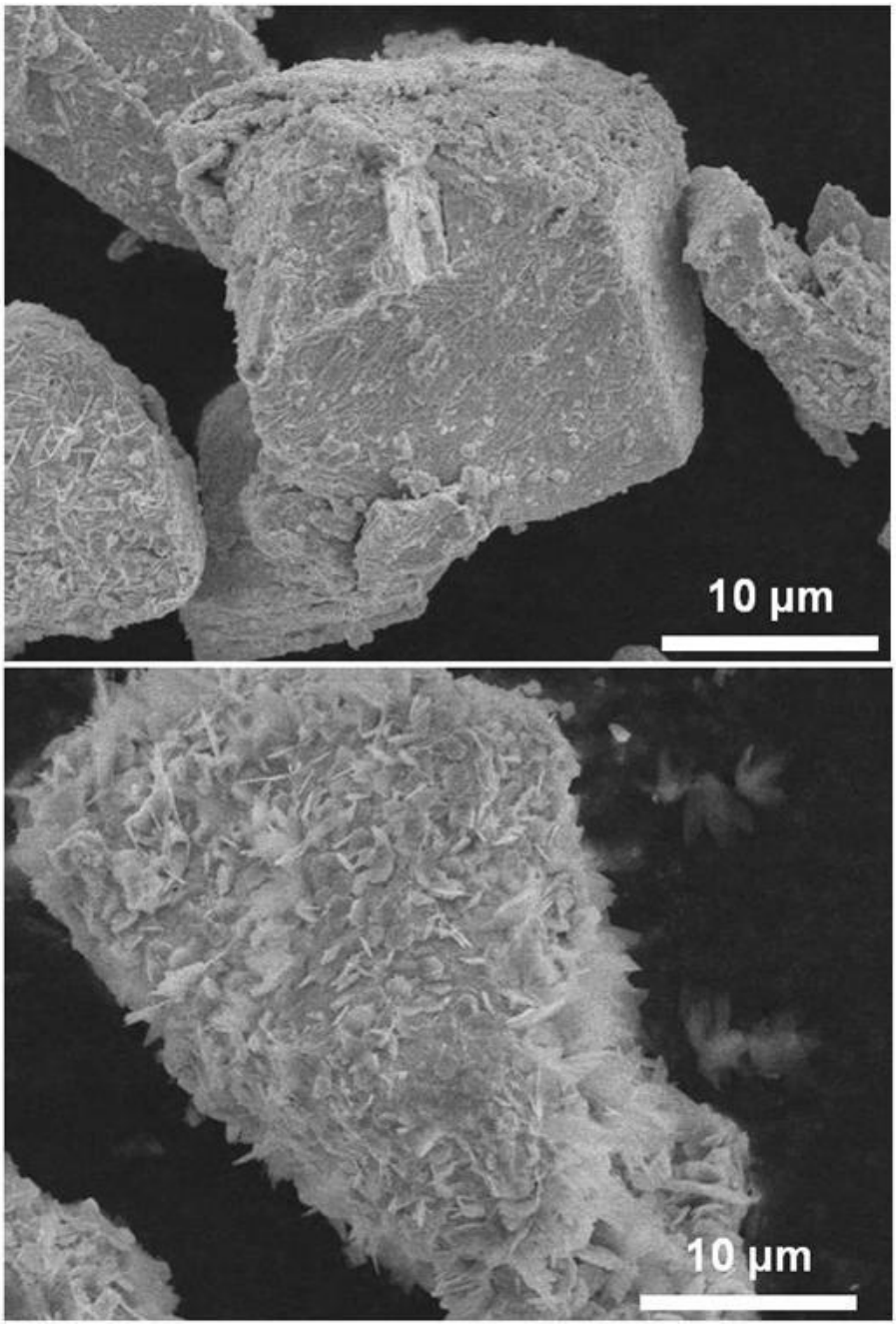

Figure 6.4. SEM images of Top: pristine Bi particle and bottom: Bi particle after soaking in 12 ml of aqueous 6M $Zn(NO_3)_2$ solution.

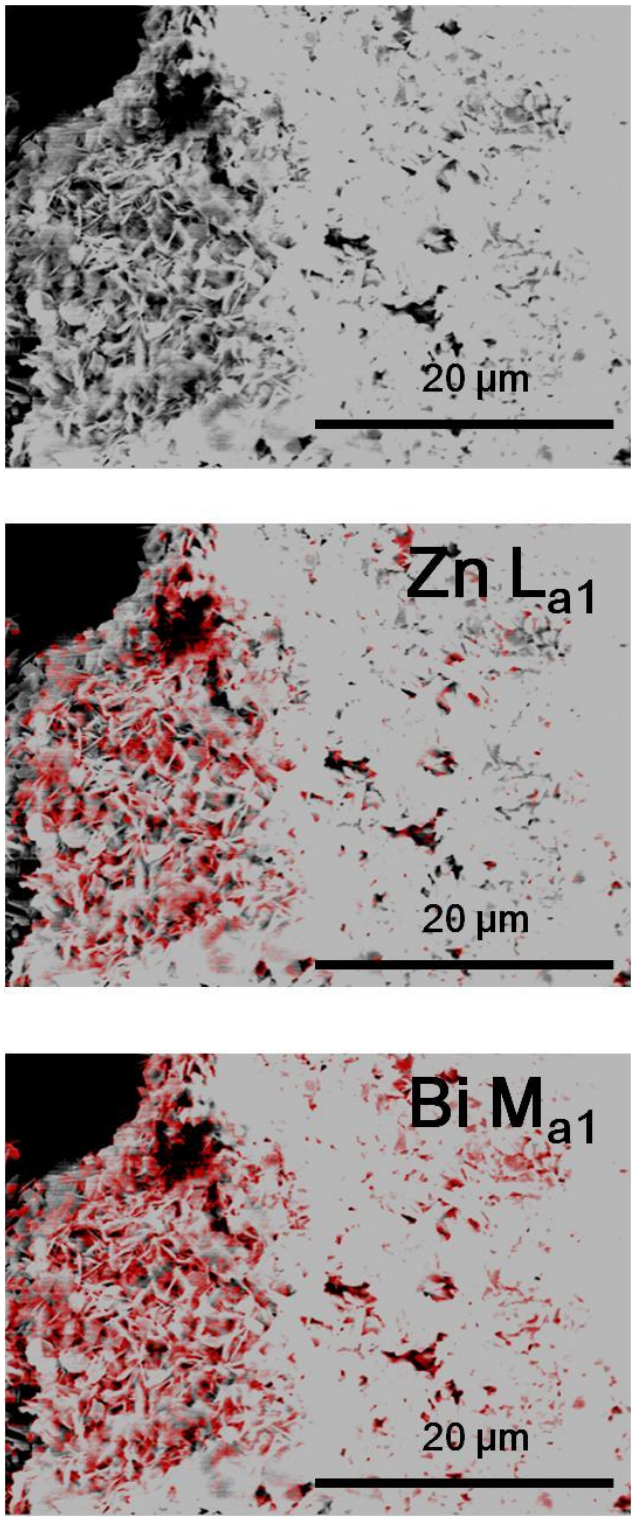

Figure 6.5. Bi particle after soaking in 12 ml Of aqueous 6M $Zn(NO_3)_2$ solution. Top: SEM image of the EDS site. Middle: EDS mapping using the Zn $L_{\alpha 1}$ data. Bottom: EDS mapping using the Bi $M_{\alpha 1}$ data

6.3.3. Cu^{2+} deposition on NiO

This simple soaking experiment with SEM observation is proven itself to be able to demonstrate the Zn^{2+} deposition phenomenon. Now that this simple experiment has proven its potential to display the deposition function of an additive, this test is applied in a different conversion type system. CuF_2 is another conversion type system in which its cycling performance benefits from NiO additive.[183] Similarly to the Zn electrode's case, the comprehensive mechanistic role of NiO additive is unclear. CuF_2 when lithiated produces Cu metal and LiF. Delithiating reproduces CuF_2. During these processes, nucleation reactions are involved and Cu^{2+} dissolves into the electrolyte. Cu^{2+} dissolution reduces the amount of active material. The NiO composite additive may be assisting to keep the Cu^{2+} ions from dissolving out into the electrolyte. To test this hypothesis, NiO is soaked into the 18 ml of aqueous 0.5 M $Cu(SO_4)$ solution. Upon collecting, the morphology of the NiO surface has completely changed. (**Figure 6.6**). The pristine NiO surface is smoother and has various particle size distribution. After the soaking, the surface has became rough with smaller particles surrounding the larger particles. To further confirm the Cu^{2+} deposition on the NiO surface, EDS mapping has been collected (**Figure 6.7**). The NiO particle after soaking in 18 ml of aqueous 0.5M $Cu(SO_4)$ solution is used to observe the presence of Cu and Ni. The elemental distribution is homogeneously distributed.

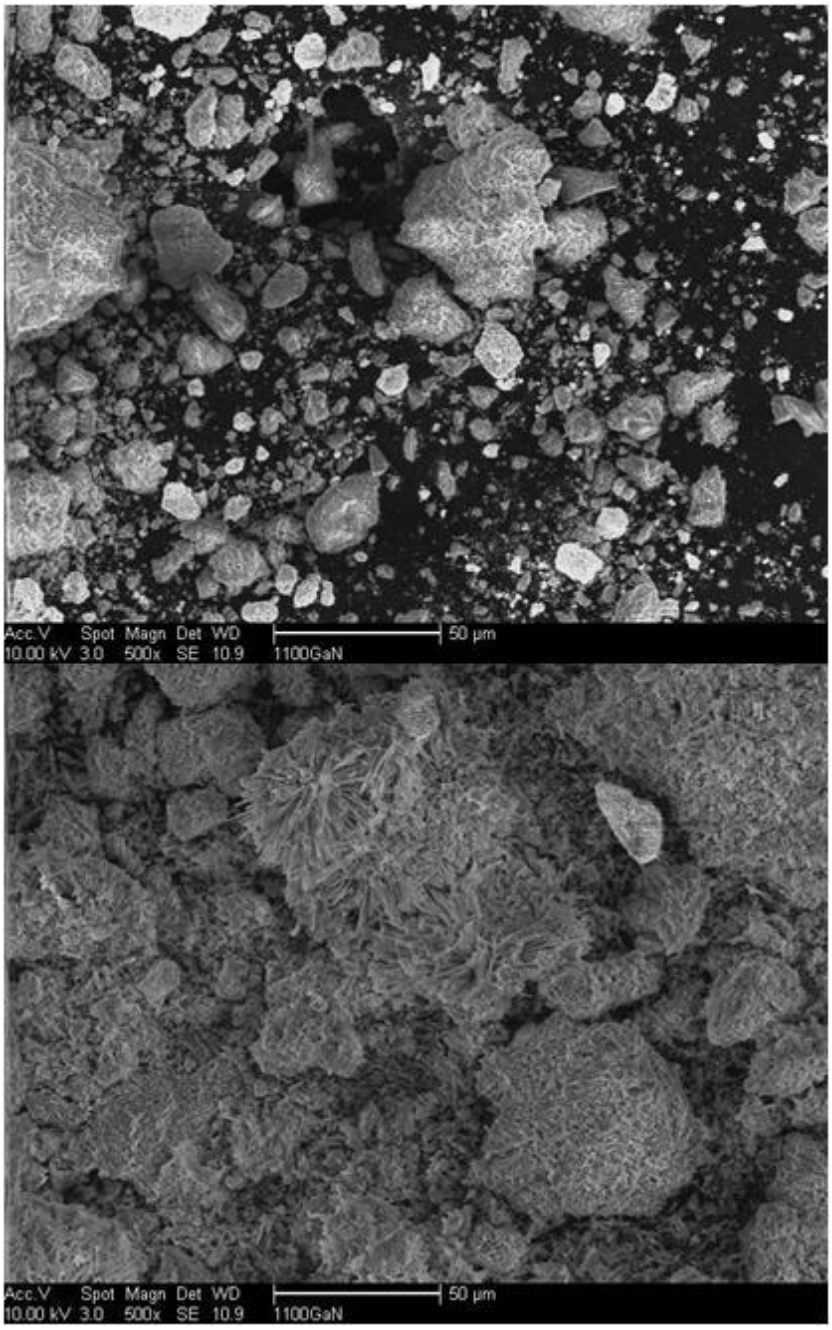

Figure 6.6. SEM images of Top: pristine NiO particle and bottom: NiO particle after soaking in 18 ml of aqueous 0.5M $Cu(SO_4)$ solution.

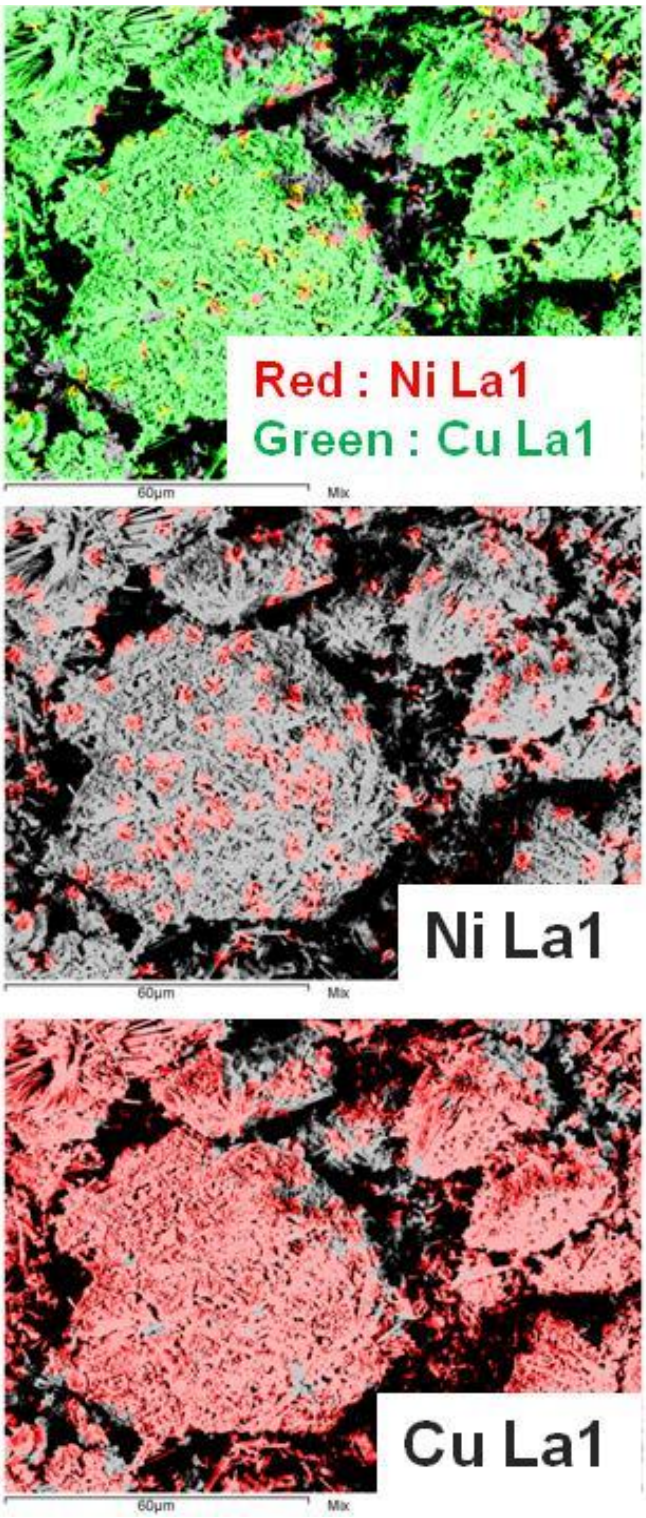

Figure 6.7. NiO particle after soaking in 18 ml of aqueous 0.5M $Cu(SO_4)$ solution. Top: SEM image of the EDS site. Middle: EDS mapping using the Ni $L_{\alpha 1}$ data. Bottom: EDS mapping using the Cu $L_{\alpha 1}$ data

6.3.4. Mn^{2+} deposition on Bi_2O_3

Utilizing MnO_2 in an electrochemical system alkaline battery has a long history. Since it was first commercialized in 1940s, MnO_2/Zn alkaline chemistry has been widely applied to operate household goods as well as small portable devices.[184] Recently, adopting alkaline batteries into grid-scale EESS is emerging especially in load leveling and stabilizing intermittent renewable energy from solar and wind power.[185] MnO_2 in alkaline batteries has several advantages: low cost, high energy density, and safety. For example, MnO_2/Zn alkaline battery has a capital cost of $ 90-140 per kWh.[141] Theoretical energy density of MnO_2 reaction is 308 Wh kg^{-1} and the chemistry of MnO_2 alkaline battery is relatively safe as it operates under aqueous media.[143] While most other alkaline battery materials are predominantly primary batteries (non-rechargeable) by nature, MnO_2 is recently considered as a secondary battery (rechargeable). However, MnO_2 after reduction goes through several crystal reconstruction as well as dissolution. After one electron reduction, α-MnOOH and γ-MnOOH phases are formed. Upon two electron reductions, $Mn(OH)_2$ phase is formed. While going through the phase transformations, the Mn^{3+} can dissolve into the electrolyte. In addition, $Mn(OH)_2$ phase is highly soluble due to Mn^{2+} having ionic bond. Recently, Bi_2O_3 composite has shown to improve the cycle ability of MnO_2.[186]

Again, the mechanistic role of Bi_2O_3 in MnO_2 battery is not well described. To see if the role of Bi_2O_3 is related to the Mn^{2+} dissolution, the simple soaking test is conducted. To test this hypothesis, Bi_2O_3 is soaked into the 12 ml of aqueous 2M $Mn(NO_3)_2$ solution. Upon collecting, the morphology of the Bi_2O_3 surface has completely

changed. (**Figure 6.8**). The pristine Bi_2O_3 surface is smoother and has various particle size distribution. After the soaking, the surface has became rough with smaller particles surrounding the larger particles. To further confirm the Mn^{2+} deposition on the Bi_2O_3 surface, EDS mapping has been collected (**Figure 6.9**). The Bi_2O_3 particle after soaking in 12 ml of aqueous 2M $Mn(NO_3)_2$ solution is used to observe the presence of Mn and Bi. The elemental distribution is homogeneously distributed.

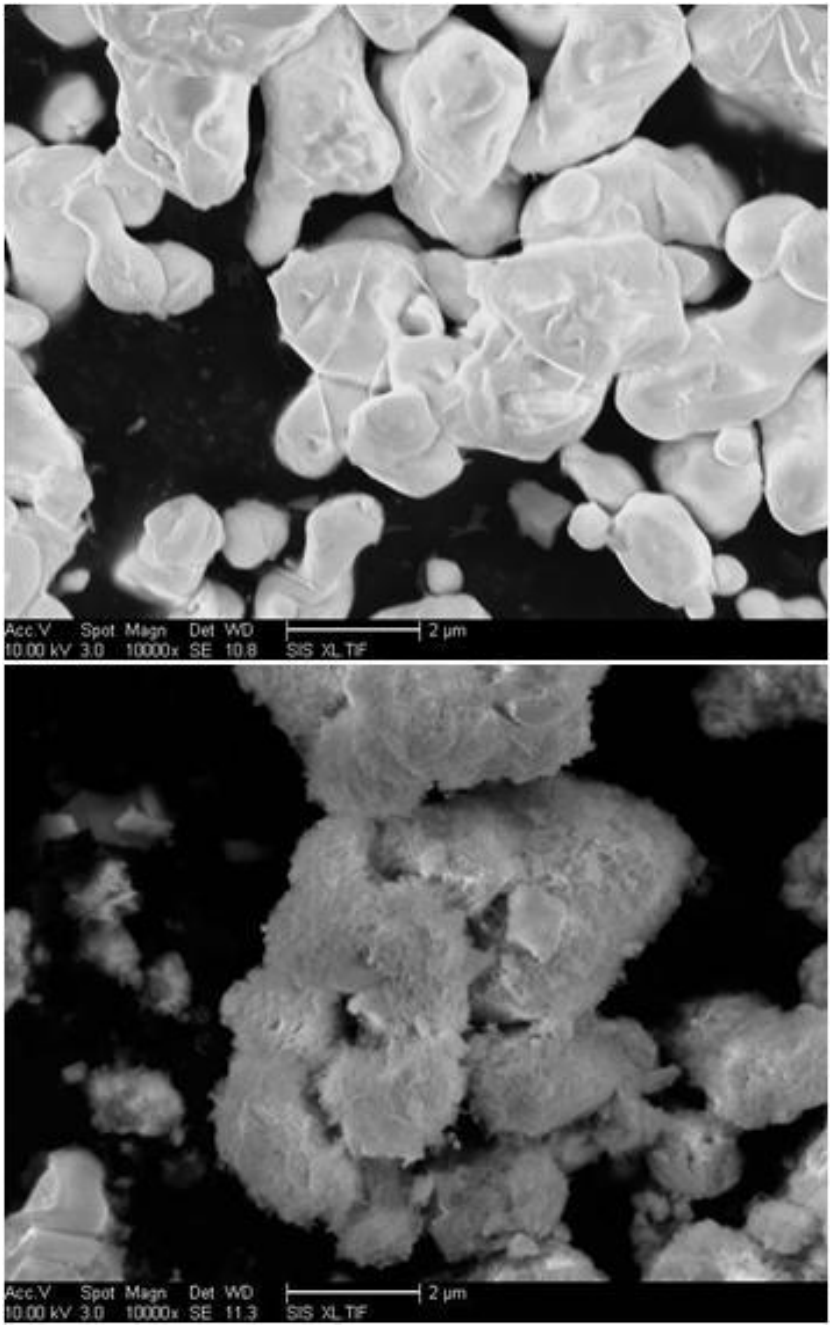

Figure 6.8. SEM images of Top: pristine Bi_2O_3 particle and bottom: Bi_2O_3 particle after soaking in 12 ml of aqueous 2M $Mn(NO_3)_2$ solution.

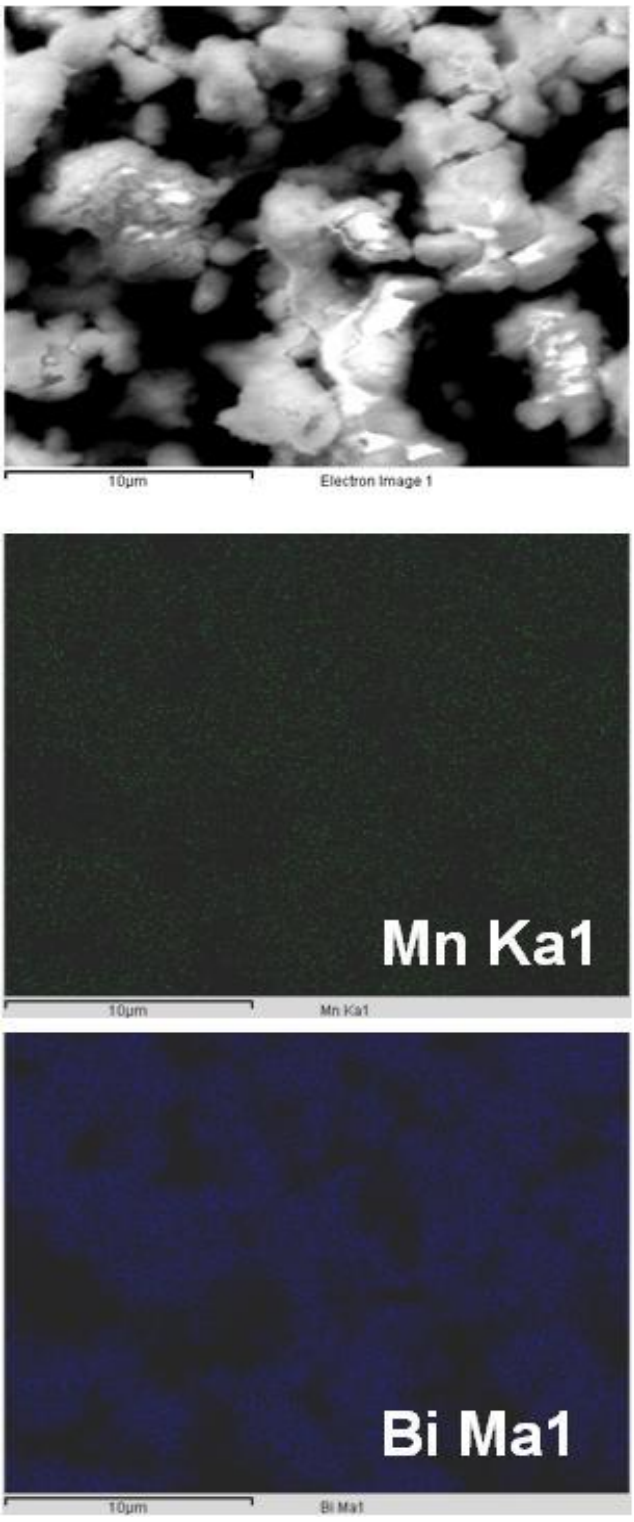

Figure 6.7. Bi_2O_3 particle after soaking in 12 ml Of aqueous 2M $Mn(NO_3)_2$ solution. Top: SEM image of the EDS site. Middle: EDS mapping using the Mn $L_{\alpha 1}$ data. Bottom: EDS mapping using the Bi $M_{\alpha 1}$ data

6.4. Conclusion

There is a great energy density incentive for being able to utilize the conversion type electrode materials. One of the biggest hurdles for these materials is the dissolution problem of the intermediate phase. Since the intermediate phase is soluble in electrolyte, the electrode material is lost. In the previous chapter, functional composite additive that can deposit the dissolved ions is introduced. This functionality should be utilized in wide range of conversion electrodes. However it is too time consuming to test all candidates in the battery system as fabrication and the electrochemical testing are time consuming. A simple soaking test is proposed to identify the promising functional composite additive candidate for a respective system. This test can potentially save time and research cost as well as allow for higher energy density energy storage devices.

Chapter 6, in part, is a reprint of the material “Relaxation of ZnO on Bismuth Species Towards Rechargeable Zn-based Aqueous Battery” as it appears in the Physical Chemistry Chemical Physics, Jaewook Shin, R. J.-M. You, J. Lee, R. Kumar, L. Yin, J. Wang, and Y. S. Meng,, 2016, accepted manuscript. The dissertation author was the co-primary investigator and author of this paper.

Chapter 7. Future aspects

MnO_2, a conversion type cathode material

MnO_2 battery has a promising but uneasy future ahead. One of the major difficulties in installing an EESS is the cost of the materials. For a large scale EESS, the material cost should be low, such as water for the hydroelectric. MnO_2 is a promising candidate in terms of the cost. Manganese is the 12th most abundant element in the Earth's crust;[187] it is a significant component in soil[188-190] thus, making it one of the cheapest materials available. However, MnO_2 has intrinsic lack of conductivity and dissolution problem those hinder its commercialization. Since EESS is in dire need of improvement, MnO_2 system is proposed to be studied.

The electrochemical activities of MnO_2 have been reported for more than a century. The old MnO_2 system deserves to gain the spotlight because of its complexity. Even though the system has been studied for decades, recent development of characterization techniques and knowledge broadened the understanding of MnO_2 system and left rooms to improve. First of all, MnO_2 does not refer to one material. It is necessary to understand that there are a few polymorphs of MnO_2 and they should be considered differently.[191, 192] Due to the difference in crystal structure of the MnO_2, a redox reaction kinetic is completely disparate.[193] There are six polymorphs of manganese dioxide discussed in the literature: (1) α-MnO_2 (2 X 2 tunnel or hollandite), (2) β-MnO_2 (1 X 1 tunnel or pyrolusite), (3) R-MnO_2 (2 X 1 tunnel or Ramsdellite), (4) γ-MnO_2 (mix of 2 X 1 and 1 X 1 tunnels or nsutite), (5) δ-MnO_2 (layered or birnessite), and (6)

λ-MnO_2 (3-dimensional pores or spinel) (**Figure 7.1**). The polymorphs have distinctive atomic arrangements those result in various types of pores or tunnels within the crystal structure. Due to the distinctive crystal structure, the selectivity towards different ions or electron transfer kinetics is immense. Since most EESS utilizes ions in the electrolyte and electron transfer kinetics on the electrode surface, it is expected that the crystal structure and the applications are closely related. Each EESS has their own mechanisms of ions and electron transfer, so depending on the crystal structure of the MnO_2, different EESS is associated.

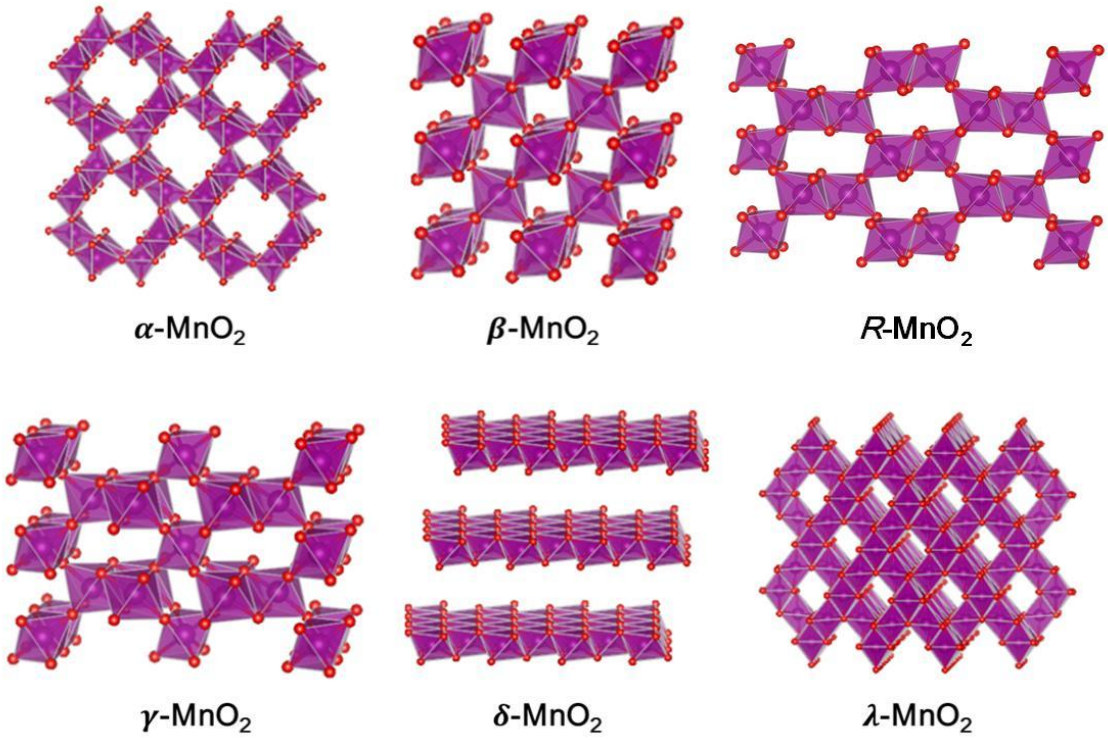

Figure 7.1. Crystal structures of MnO_2 polymorphs (Mn: magenta and O: red). The structure of γ-MnO_2 consists of an intergrowth between 1 X 1 and 2 X 1 tunnels. The ratio of 1 X 1 tunnel over 1 X 1 and 2 X 1 tunnels is called Pr (0% < Pr < 100%).[194] The shown γ-MnO_2 compound has Pr = 50%. Water molecules and guest cations are omitted for clarity.

There are four major types of EESS in which MnO_2 has been utilized: alkaline battery, LIB, supercapacitor, and metal-air battery (MAB). All EESS in discussion focus on aqueous electrolyte systems because of their low cost compared to their counterpart, organic electrolyte systems. Great interest in these systems has exponentially grown over the years (**Figure 7.2.a**). Especially, the alkaline battery system has the longest history among the four systems with almost an order of magnitude more papers published than the other three systems. On the other hand, although the supercapacitor system has the shortest history, myriad papers are published on supercapacitor every month these days.

The other two systems have fewer publications, yet they are accumulating research papers as many as that of the supercapacitor and still have faster rate of publications than that of the alkaline battery. Mostly due to the low cost nature of MnO_2, it has been utilized in cathode materials. As mentioned earlier, the crystal structure has the great effect on the performance of EESS depending on the mechanism. The four EESS have distinctive mechanisms, which fill different areas on the Ragone plot (**Figure 7.2.b**). The alkaline battery has high energy, but low power whereas the supercapacitor has high power and low energy. The LIB sits in the middle of the two and the metal-air has a wide range of energy, but narrow power. In the large-scale energy storage, the power required by the consumers varies throughout the day. It is vital to have complimentary EESS to be able to charge/discharge in a wide range of energy and power. EESS with lower power but higher energy is favored in the hour range of fluctuation and EESS with higher power but lower energy is suitable in the minute range of fluctuation. In the real world with a dynamic range of the fluctuation, a combination of MnO_2 systems with varying performance will complement each other.

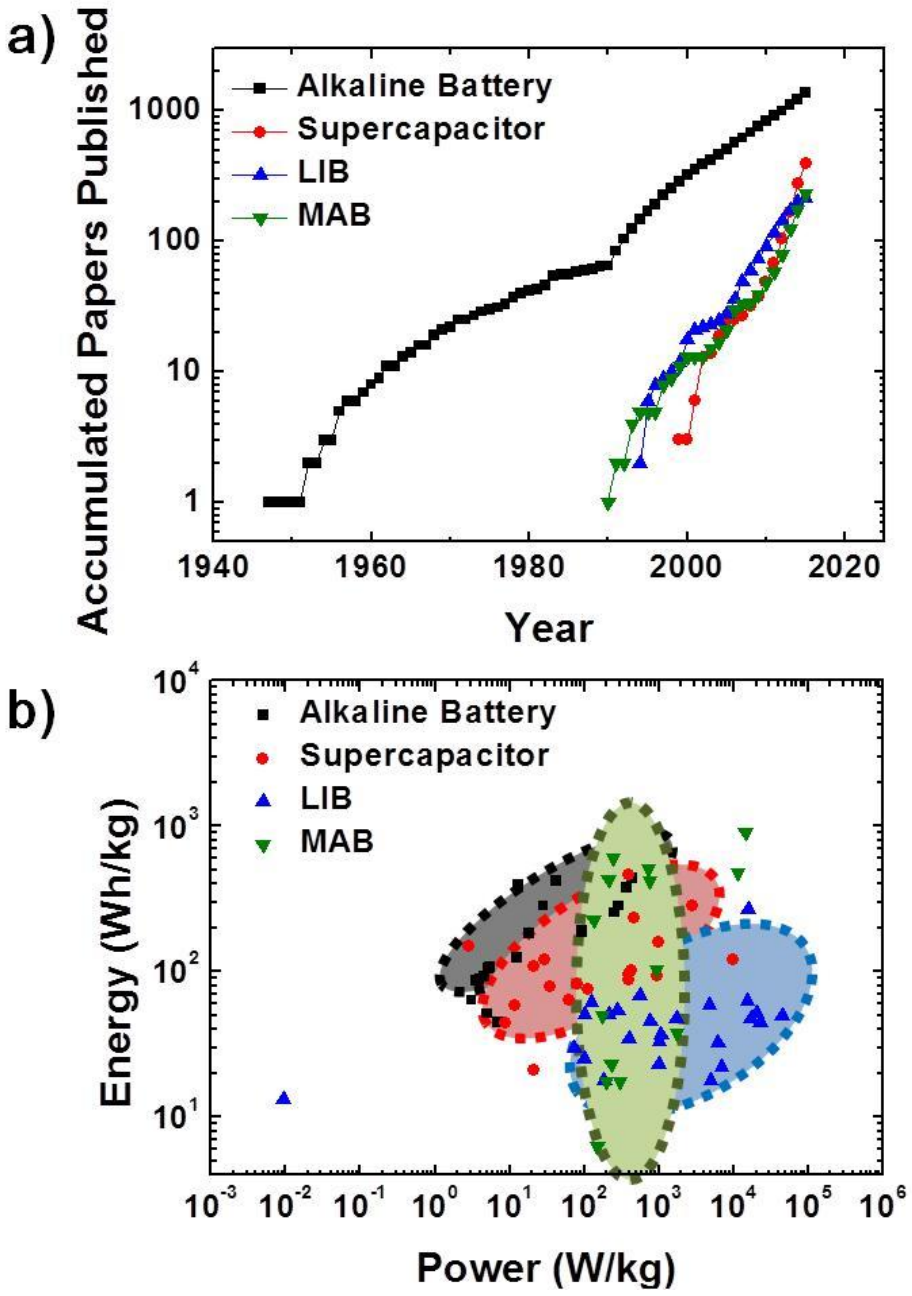

Figure 7.2. a) Accumulated papers (articles and review) published on various EESS systems. Source: Web of Science database. b) A Ragone plot comparing alkaline battery, LIB, supercapacitor, and metal-air battery that utilize manganese dioxide. Source: Web of Science database. Data is updated on November 2015.

In order to develop methods for commercializing MnO_2 systems, it is essential to understand the mechanisms.[195, 196] Owing to its longest history, the alkaline systems have extensive comprehension of additive's function and benefits. Based on Minakshi's work, it is clear that the optimum use of the additives can dramatically boost the performance of the EESS.[197] Unlike the alkaline system, the other three systems have a quite short history. Although they are showing fast growth, much of the mechanism is not fully explained. Probing the mechanism provides efficient ways to achieve optimum conditions for the best performance.[196] It is necessary to devise suitable tools to examine the change happening in MnO_2. Finding out the exact change of MnO_2 phase and products of side reaction during the electrochemical cycling is imperative to develop optimum MnO_2. Much of the characterization tools are invented in the ORLB field. One of the main differences between the ORLB and the four EESS systems is the electrolyte. Because the dry organic electrolyte is used in the ORLB, it often requires special experimental set-ups to avoid air contamination.[123] The four EESS systems adopt aqueous electrolytes and the samples can be exposed to the air, the experimental design is easier than ORLB.

As mentioned earlier, the polymorphic crystal structure has a vital influence on the MnO_2 mechanism. Unfortunately, in some literature, even the pristine material is not properly identified before moving on to the electrochemical tests. The exact crystal structure needs to be recognized to enable pursuing further mechanism studies ahead.[123, 198] Due to the presence of water molecules, hydronium ions, and alkali metal ions in the tunnels of the porous structures, a simple PXRD is not a sufficient tool to solve the crystal structure.[199-201] In case of γ-MnO_2, which is a mixture of β-MnO_2 and R-MnO_2,[202]

the phase boundary between the two phases is difficult to observe. In many cases, the PXRD result needs to be combined with other complementary techniques: ND, the XAS, and the magic angle spinning nuclear magnetic resonance (MAS-NMR).[201, 203-205] The combination of these techniques determines both the long range ordering and short range ordering to obtain the exact crystal structure of the pristine material.

Once the pristine material has been clearly identified, the electrochemical test needs to be conducted. In EESS, the energy is stored in the form of electrons, one should monitor the change in electronic structure and/or magnetic property of the material.[69, 71, 204, 206-208] Characterizing these properties in an electrochemical test helps defining the mechanism. In an electrochemical cell, this is not a simple task because the material's properties change sometimes when the material is extracted from the electrochemical cell. In this case, an *in situ* cell must be constructed to collect the material property with the electrochemical property.[125] Compared to ORLB, constructing this type of *in situ* cells is much easier for the aqueous electrolyte systems. In case of a supercapacitor, the electrochemical test only takes few minutes and the self-discharge starts to occur almost immediately. By the time the sample property is measured, the material relaxes into a different state.[209] For this case, an *operando* measurement is required because it determines the material property during the electrochemical test. While *ex situ* measurements mostly observe thermodynamically stable products, *operando* measurements can observe kinetically stable products as well. Various conditions of characterizations should be employed to construct a solid mechanism.

Based on thorough interpretation of the mechanism, numerous methods can be

applied to improve the electrochemical performance. The routes that are discussed in this review are additives, coating/deposition, and doping/defect; exploring these routes requires screening.[210] Since screening every possible solutions can take too much time and effort, first principles high-throughput computation methods should be utilized to screen promising materials.[211, 212] In order to perform the high-throughput screening, different traits of the potential property need to be established. Fortunately, these properties would have been identified from constructing the comprehensive mechanism. Through considering these parameters, the new materials can be proposed minimizing the unnecessary syntheses.[212, 213]

Chapter 7, in part, is currently being prepared for submission for publication of the material "Manganese Based Oxides as Electrode Materials in Energy Storage Devices: A Review" The dissertation author was the primary investigator and author of this paper.

Chapter 8. Summary

8.1. MIL-101(Fe) as LIB electrode material

The current commercially available LIB material cost is too high to be implemented into the grid scale energy storage. To combat the cost issue, MIL-101(Fe) is synthesized via the low cost and quick microwave synthesis. MIL-101(Fe), similar to MIL-53(Fe) and MIL-68(Fe), undergoes quasi reversible Fe^{2+} and Fe^{3+} redox reaction. The amount of Fe usage is only about 60% while maintaining the intercalation reaction scheme rather than the conversion type reaction. Particularly with MIL-101(Fe), a surprising phenomenon occurs with respect to the rate of electrochemical cycling. The retention decreases when there is a rest step in between the lithiation and delithiation step. A longer rest step leads to lower the retention. To investigate this issue, PXRD is conducted to ensure that the crystal structure is not collapsing. Although MIL-101(Fe) undergoes only the pure intercalation reaction, the retention suffers from a time dependent electrochemical reaction. To confirm the Fe^{2+} and Fe^{3+} redox reaction, XAS is collected. When XAS is measured several days after the device operates only Fe^{3+}, the pristine oxidation state of MIL-101(Fe) can be achieved. On the contrary, when the XAS is measured during the device operation, Fe^{3+} to Fe^{2+} reduction and Fe^{2+} to Fe^{3+} reversible oxidation can be observed. This time dependent oxidization change suggests that when MIL-101(Fe) is lithiated or reduced, there are a kinetically stable product and a thermodynamically stable product. The kinetically stable product is the Fe^{2+} containing phase and the thermodynamically stable product is the Fe^{3+} containing phase. To identify the thermodynamically stable phase, Gaussian code is adopted to compute the electronic

structure of Fe containing oxo-tricluster. EXAFS suggests that there is a change in coordination environment with Fe. The electronic state computation concludes that the coordination altered tricluster is more stable at the reduced state. Furthermore, in all the reduced states, the electron density from the Fe^{2+} (the initial state of iteration) becomes closer to that of Fe^{3+} (after the convergence). This suggests that the electron density among the tricluster is shared thermodynamically.

This MIL-101(Fe) case is a study in which a non-conventional LIB electrode material exhibited a conventional intercalation reaction. However, due to the novel crystal structure and thermodynamic stability of MIL-101(Fe), the relaxation phenomenon complicates the lithiation and delithiation process. In order to understand the relaxation phenomenon of MIL-101(Fe), it is best to use the electrode in charge and discharge these type of applications swiftly. If there is limited time between the discharge and charge, the electrode performs much better than when there is ample time.

8.2. Bi_2O_3 as functional composite additive for rechargeable Zn electrode

The current commercially available LIB materials lack energy density to be implemented into the grid scale energy storage. The LIB is constrained by the type of reaction it utilizes. Intercalation reaction provides a high stability in cycling retention. However, this is due to the fact that significant crystal strain is avoided during charge and discharge by adopting only a fraction of the available oxidation states of transition metal. Conversion reaction, on the other hand, employs all the oxidation states available. This causes the complete reconstruction of the crystal structures, which leads to low cycling retention, yet providing the significantly high energy density. The key to successfully employing the conversion reaction is by understanding the main issues and proper

solutions.

Zn electrode is one of the oldest form of battery electrodes mankind has known. Its theoretical energy density and low cost are far beyond those of the conventional LIB electrodes, however, its cycling retention is particularly poor. This is due to the relaxation of Zn when it oxidizes in the electrolyte. When Zn oxidizes, the ZnO is formed, which is a thermodynamically stable phase. As an intermediate, Zn ions are created as a kinetically stable product. The problem is that the Zn ions are soluble in the electrolyte. Since the Zn ions dissolve into the electrolyte, the Zn electrode loses active materials. As cycles go on, the loss of active materials and electrical connections during the process is detrimental to the rechargeable Zn electrode retention. One of the promising methods to solve this issue is adding Bi_2O_3 as a composite additive. This additive has proven to enhance the cycling performance of Zn electrode. However, the mechanistic role of Bi_2O_3 is described as a conductive agent. Literatures describe the benefit of Bi_2O_3 additive as the enhanced electrical connection in the electrode. However, it is difficult to assess that the conductivity solves the Zn dissolution. Dissolution problem is intrinsic to the Zn electrode. Electrical conductivity can be solved with other alternatives at lower cost.

To comprehend the role of Bi_2O_3 in rechargeable Zn electrode, Bi_2O_3 additive has been systematically studied. To test the effect of electrical conductivity, conductive carbon powder is added into the Zn electrode. This electrode yields slightly higher capacity retention than pure Zn electrode, but not enough to be considered rechargeable. Bi_2O_3, however, as an additive, follows similar retention decay in the first few cycles. After a few cycles, the cycling retention improves and maintains stability for at least 30 cycles. It is clear that the electrical conductivity is not the main role of Bi_2O_3 additive.

Bi_2O_3 is further studied with PXRD. Bi_2O_3 in the Zn electrode, after being soaked in the electrolyte, reduces to Bi metal-like crystals. Neither Bi_2O_3 particles nor Zn particles alone does not have this change in the electrolyte, the combination of the two results in this change. A form of interaction between the two particles is expected. The Zn electrode upon oxidation reaction is observed under SEM to identify the changes Bi_2O_3 went through. The surface morphology of the Bi_2O_3 is altered upon oxidation reaction. Furthermore, EDS mapping shows that the Bi_2O_3 particles not only contain the Bi element, but also the Zn element. Raman spectrum also indicates that the ZnO is formed on the Zn electrode, but the ZnO has defects such as lattice mismatching or oxygen deficiency. Zinc and bismuth oxide have certain interaction. XPS is applied to confirm that there is an intermediate Zn-Bi-oxide phase present in the Zn electrode upon oxidation reaction. During the large crystal reconstructions of both Bi_2O_3 and Zn, an intermediate phase is created on the surface of the bismuth species. This species becomes the source of further ZnO deposition on the conductive bismuth species maintaining the electrical contact as well as redox activity.

Zn is a conversion type battery material. Two electrons are involved in its redox reaction. During the redox, the Zn has the major dissolution problem that can be resolved by the Bi_2O_3 composite additive. This is a case where relaxation phenomenon causes the deterioration of the electrode integrity whereas an additive is utilized to bypass and solve the issue.

8.3. A simple soaking experiment to propose functional composite additive

The conversion type materials have higher energy density than the intercalation type materials but lack rechargeability due to their dissolution problem during the redox

reaction. Thermodynamically the phase transformation during redox reaction is straightforward, however, intermediate phases get involved kinetically. The kinetically stable products are soluble in the electrolyte. The dissolution of the intermediate phase leads to a loss of active materials. The Bi_2O_3 and the Zn study demonstrated that the conversion materials benefit from adding a functional additive to retain the active material on the surface of the electrode. However, it is difficult to test all the candidates in a battery. Electrode fabrication requires optimizing which requires multiple trial and error.

To speed up this process, a simple soaking experiment to determine the additive's functionality is demonstrated. First, Bi_2O_3 and Bi metal are both soaked in the Zn^{2+} solution. These two tests confirmed that the Bi_2O_3 and Bi metal surface has deposition property with Zn^{2+} ions. Another example of this case is the NiO additive effect on CuF_2 electrode. Adding NiO enhances the CuF_2 cycleability, yet the comprehensive role of NiO is still unknown. The same simple soaking test is conducted with the NiO powder and Cu^{2+} containing solution. NiO has deposition property with the Cu^{2+} ions. To further expand on the practical use of this test, MnO_2 system is applied. The MnO_2 system is also a conversion type system in which the Mn^{2+} dissolution is a major concern. Bi_2O_3 composite additive was utilized in the past without a proper justification, however, Bi_2O_3 has deposition property with Mn^{2+} ions as well.

While the first two cases are offered to probe the importance and mechanism of the relaxation phenomenon, this case is dedicated to the future aspects. MnO_2 is a complex system in which multiple phase transformations exist. A simple test is necessary to simplify the problem and solve multiple issues one by one.

References

1. Dunn, B.; Kamath, H.; Tarascon, J. M., Electrical Energy Storage for the Grid: A Battery of Choices. *Science* **2011,** 334, (6058), 928-935.

2. Sabihuddin, S.; Kiprakis, A. E.; Mueller, M., A Numerical and Graphical Review of Energy Storage Technologies. *Energies* **2015,** 8, (1), 172-216.

3. *EPRI-DOE Handbook of Energy Storage for Tranmission and Distribution Applications*; EPRI and the U.S. Department of Energy: Palo Alto, 2003.

4. Deane, J. P.; Gallachoir, B. P. O.; McKeogh, E. J., Techno-economic review of existing and new pumped hydro energy storage plant. *Renewable & Sustainable Energy Reviews* **2010,** 14, (4), 1293-1302.

5. Chen, H. S.; Cong, T. N.; Yang, W.; Tan, C. Q.; Li, Y. L.; Ding, Y. L., Progress in electrical energy storage system: A critical review. *Progress in Natural Science* **2009,** 19, (3), 291-312.

6. Agency, I. E. *Worldwide Trends in Energy Use and Efficiency: Key Insights from Iea Indicator Analysis*; Paris, France, 2008.

7. Administration, U. S. E. I. *International Energy Outlook 2013*; Washington, DC, USA, 2013.

8. Xu, B.; Qian, D.; Wang, Z.; Meng, Y. S., Recent progress in cathode materials research for advanced lithium ion batteries. *Materials Science and Engineering R* **2012,** 73, 51-65.

9. Peng, L. L.; Zhu, Y.; Chen, D. H.; Ruoff, R. S.; Yu, G. H., Two-Dimensional Materials for Beyond-Lithium-Ion Batteries. *Advanced Energy Materials* **2016,** 6, (11).

10. Badway, F.; Cosandey, F.; Pereira, N.; Amatucci, G. G., Carbon metal fluoride nanocomposites - High-capacity reversible metal fluoride conversion materials as rechargeable positive electrodes for Li batteries. *Journal of the Electrochemical Society* **2003,** 150, (10), A1318-A1327.

11. Alcantara, R.; Lavela, P.; Tirado, J. L.; Zhecheva, E.; Stoyaneva, R., Recent advances in the study of layered lithium transition metal oxides and their application as intercalation electrodes. *Journal of Solid State Electrochemistry* **1999,** 3, (3), 121-134.

12. Augustyn, V.; Simon, P.; Dunn, B., Pseudocapacitive oxide materials for high-rate electrochemical energy storage. *Energy & Environmental Science* **2014,** 7, (5), 1597-1614.

13. Rozier, P.; Tarascon, J. M., Review-Li-Rich Layered Oxide Cathodes for Next-Generation Li-Ion Batteries: Chances and Challenges. *Journal of the Electrochemical Society* **2015,** 162, (14), A2490-A2499.

14. Ben Yahia, H.; Shikano, M.; Kobayashi, H., Phase Transition Mechanisms in LixCoO2 (0.25 <= x <= 1) Based on Group-Subgroup Transformations. *Chemistry of Materials* **2013,** 25, (18), 3687-3701.

15. Yi, T. F.; Mei, J.; Zhu, Y. R., Key strategies for enhancing the cycling stability and rate capacity of LiNi0.5Mn1.5O4 as high-voltage cathode materials for high power lithium-ion batteries. *Journal of Power Sources* **2016,** 316, 85-105.

16. Yim, H.; Shin, D. W.; Choi, J. W., LiMn2O4-based cathode thin films for Li thin-film batteries. *Journal of the Korean Physical Society* **2016,** 68, (1), 41-53.

17. Chemali, E.; Preindl, M.; Malysz, P.; Emadi, A., Electrochemical and Electrostatic Energy Storage and Management Systems for Electric Drive Vehicles: State-of-the-Art Review and Future Trends. *Ieee Journal of Emerging and Selected Topics in Power Electronics* **2016,** 4, (3), 1117-1134.

18. Gong, C. L.; Xue, Z. G.; Wen, S.; Ye, Y. S.; Xie, X. L., Advanced carbon materials/olivine LiFePO4 composites cathode for lithium ion batteries. *Journal of Power Sources* **2016,** 318, 93-112.

19. Armand, M.; Tarascon, J. M., Building better batteries. *Nature* **2008,** 451, (7179), 652-657.

20. Anthony, F. S., Fuel cells and electrochemical energy storage. *Journal of Chemical Education* **1983,** 60.

21. Tarascon, J.; Armand, M., Issues and challenges facing rechargeable lithium batteries. *Nature* **2001,** 414, (6861), 359-367.

22. Tarascon, J.-M., Towards sustainable and renewable systems for electrochemical energy storage. *ChemSusChem* **2008,** 1, (8-9), 777-779.

23. Pearce, J. M., Thermodynamic Limitations to Nuclear Energy Deployment as a Greenhouse Gas Mitigation Technology. *International Journal of Nuclear Governance, Economy and Ecology* **2008,** 2, (1), 17.

24. Walker, W.; Grugeon, S.; Mentre, O.; Laruelle, S.; Tarascon, J. M.; Wudl, F., Ethoxycarbonyl-Based Organic Electrode for Li-Batteries. *Journal of the American Chemical Society* **2010,** 132, (18), 6517-6523.

25. Walker, W.; Grugeon, S.; Vezin, H.; Laruelle, S.; Armand, M.; Tarascon, J. M.; Wudl, F., The effect of length and cis/trans relationship of conjugated pathway on

secondary battery performance in organolithium electrodes. *Electrochemistry Communications* **2010,** 12, (10), 1348-1351.

26. Nakahara, K.; Iwasa, S.; Satoh, M.; Morioka, Y.; Iriyama, J.; Suguro, M.; Hasegawa, E., Rechargeable batteries with organic radical cathodes. *Chemical Physics Letters* **2002,** 359, (5-6), 351-354.

27. Burkhardt, S. E.; Bois, J.; Tarascon, J. M.; Hennig, R. G.; Abruna, H. D., Li-Carboxylate Anode Structure-Property Relationships from Molecular Modeling. *Chemistry of Materials* **2013,** 25, (2), 132-141.

28. eecfncci FurnaceOverview for furnace. http://www.eec-fncci.org/content-learn-furnace#content-learn-furnace_energy_efficiency

29. Bennett, R., *Process Heating* 1997.

30. Kim, J.; Chen, B. L.; Reineke, T. M.; Li, H. L.; Eddaoudi, M.; Moler, D. B.; O'Keeffe, M.; Yaghi, O. M., Assembly of metal-organic frameworks from large organic and inorganic secondary building units: New examples and simplifying principles for complex structures. *Journal of the American Chemical Society* **2001,** 123, (34), 8239-8247.

31. Deria, P.; Mondloch, J. E.; Karagiaridi, O.; Bury, W.; Hupp, J. T.; Farha, O. K., Beyond post-synthesis modification: evolution of metal-organic frameworks via building block replacement. *Chemical Society Reviews* **2014,** 43, (16), 5896-5912.

32. Mellot-Draznieks, C.; Dutour, J.; Férey, G., Computational design of hybrid frameworks: Structure and energetics of two Me3OF3{-O2C-C6H4-CO2-}(3) metal-dicarboxylate polymorphs, MIL-hypo-1 and MIL-hypo-2. *Zeitschrift Fur Anorganische Und Allgemeine Chemie* **2004,** 630, (15), 2599-2604.

33. Xiaoxia, L.; Fangyi, C.; Shuna, Z.; Jun, C., Shape-controlled synthesis and lithium-storage study of metal-organic frameworks Zn4O(1,3,5-benzenetribenzoate)2. *Journal of Power Sources* **2006,** 160.

34. Férey, G.; Millange, F.; Morcrette, M.; Serre, C.; Doublet, M.-L.; Grenèche, J.-M.; Tarascon, J.-M., Mixed-valence li/fe-based metal-organic frameworks with both reversible redox and sorption properties. *Angewandte Chemie (International ed. in English)* **2007,** 46, (18), 3259-3263.

35. Alexandra, F.; Patricia, H.; Thomas, D.; Christian, S.; Jérôme, M.; Jean-Marc, G.; Mathieu, M.; Jean-Marie, T.; Guillaume, M.; Gérard, F., Synthesis, Structure, Characterization, and Redox Properties of the Porous MIL-68(Fe) Solid. *European Journal of Inorganic Chemistry* **2010,** 2010.

36. An, C. H.; Wang, Y. J.; Li, L.; Qiu, F. Y.; Xu, Y. N.; Xu, C. C.; Huang, Y. N.; Jiao, F.; Yuan, H. T., Effects of highly crumpled graphene nanosheets on the

electrochemical performances of pseudocapacitor electrode materials. *Electrochimica Acta* **2014,** 133, 180-187.

37. Yao, H. R.; Yin, Y. X.; Guo, Y. G., Size effects in lithium ion batteries. *Chinese Physics B* **2016,** 25, (1).

38. Huang, Q. Z.; Wang, Q., Redox-assisted Li+-storage in lithium-ion batteries. *Chinese Physics B* **2016,** 25, (1).

39. Katiyar, R. S.; Singh, G., Advances in Designing High-Energy Cathode Materials for Li-Ion Rechargeable Batteries. *Advanced Nanomaterials for Aerospace Applications* **2015**, 149-178.

40. Li, H.; Balaya, P.; Maier, J., Li-storage via heterogeneous reaction in selected binary metal fluorides and oxides. *Journal of the Electrochemical Society* **2004,** 151, (11), A1878-A1885.

41. Etacheri, V.; Marom, R.; Elazari, R.; Salitra, G.; Aurbach, D., Challenges in the development of advanced Li-ion batteries: a review. *Energy & Environmental Science* **2011,** 4, (9), 3243-3262.

42. Wang, F.; Robert, R.; Chernova, N. A.; Pereira, N.; Omenya, F.; Badway, F.; Hua, X.; Ruotolo, M.; Zhang, R. G.; Wu, L. J.; Volkov, V.; Su, D.; Key, B.; Whittingharn, M. S.; Grey, C. P.; Amatucci, G. G.; Zhu, Y. M.; Graetz, J., Conversion Reaction Mechanisms in Lithium Ion Batteries: Study of the Binary Metal Fluoride Electrodes. *Journal of the American Chemical Society* **2011,** 133, (46), 18828-18836.

43. Cui, Y. H.; Xue, M. Z.; Zhou, Y. N.; Peng, S. M.; Wang, X. L.; Fu, Z. W., The investigation on electrochemical reaction mechanism of CuF2 thin film with lithium. *Electrochimica Acta* **2011,** 56, (5), 2328-2335.

44. Mansour, A. N.; Badway, F.; Yoon, W. S.; Chung, K. Y.; Amatucci, G. G., In situ X-ray absorption spectroscopic investigation of the electrochemical conversion reactions of CuF2-MoO3 nanocomposite. *Journal of Solid State Chemistry* **2010,** 183, (12), 3029-3038.

45. Badway, F.; Mansour, A. N.; Pereira, N.; Al-Sharab, J. F.; Cosandey, F.; Plitz, I.; Amatucci, G. G., Structure and electrochemistry of copper fluoride nanocomposites utilizing mixed conducting matrices. *Chemistry of Materials* **2007,** 19, (17), 4129-4141.

46. Noel, M.; Suryanarayanan, N., Electrochemistry of metals and semiconductors in fluoride media. *Journal of Applied Electrochemistry* **2005,** 35, (1), 49-60.

47. Hua, X.; Robert, R.; Du, L. S.; Wiaderek, K. M.; Leskes, M.; Chapman, K. W.; Chupas, P. J.; Grey, C. P., Comprehensive Study of the CuF2 Conversion Reaction Mechanism in a Lithium Ion Battery. *Journal of Physical Chemistry C* **2014,** 118, (28), 15169-15184.

48. Zheng, Y.; Zhang, P.; Wu, S. Q.; Wen, Y. H.; Zhu, Z. Z.; Yang, Y., First-principles studies on the structural and electronic properties of Li-ion battery cathode material CuF2. *Solid State Communications* **2012,** 152, (17), 1703-1706.

49. Wang, F.; Yu, H. C.; Van der Ven, A.; Thornton, K.; Pereira, N.; Zhu, Y. M.; Amatucci, G. G.; Graetz, J., Ionic and electronic transport in metal fluoride conversion electrodes. *Interfaces and Interphases in Battery Systems* **2012,** 50, (1), 19-25.

50. Wang, Y.; Zhong, W. H., Development of Electrolytes towards Achieving Safe and High-Performance Energy-Storage Devices: A Review. *Chemelectrochem* **2015,** 2, (1), 22-36.

51. Beck, F.; Ruetschi, P., Rechargeable batteries with aqueous electrolytes. *Electrochimica Acta* **2000,** 45, (15-16), 2467-2482.

52. Mokhtar, M.; Talib, M. Z. M.; Majlan, E. H.; Tasirin, S. M.; Ramli, W. M. F. W.; Daud, W. R. W.; Sahari, J., Recent developments in materials for aluminum-air batteries: A review. *Journal of Industrial and Engineering Chemistry* **2015,** 32, 1-20.

53. Guduru, R. K.; Icaza, J. C., A Brief Review on Multivalent Intercalation Batteries with Aqueous Electrolytes. *Nanomaterials* **2016,** 6, (3).

54. Holze, R.; Wu, Y. P., Intrinsically conducting polymers in electrochemical energy technology: Trends and progress. *Electrochimica Acta* **2014,** 122, 93-107.

55. Gao, J.; Shi, S. Q.; Li, H., Brief overview of electrochemical potential in lithium ion batteries. *Chinese Physics B* **2016,** 25, (1).

56. Hussein, A. A.; Batarseh, I., A Review of Charging Algorithms for Nickel and Lithium Battery Chargers. *Ieee Transactions on Vehicular Technology* **2011,** 60, (3), 830-838.

57. Mao, J.; Ma, M. Z.; Liu, P. P.; Hu, J. H.; Shao, G. S.; Battaglia, V.; Dai, K. H.; Liu, G., The effect of cobalt doping on the morphology and electrochemical performance of high-voltage spinel LiNi0.5Mn1.5O4 cathode material. *Solid State Ionics* **2016,** 292, 70-74.

58. Lepage, D.; Sobha, F.; Kuss, C.; Liang, G.; Schougaard, S. B., Delithiation kinetics study of carbon coated and carbon free LiFePO4. *Journal of Power Sources* **2014,** 256, 61-65.

59. Luo, J. Y.; Xia, Y. Y., Aqueous lithium-ion battery LiTi2(PO4)(3)/LiMn2O4 with high power and energy densities as well as superior cycling stability. *Advanced Functional Materials* **2007,** 17, (18), 3877-3884.

60. Li, W.; Mckinnon, W. R.; Dahn, J. R., Lithium Intercalation from Aqueous-Solutions. *Journal of the Electrochemical Society* **1994,** 141, (9), 2310-2316.

61. Hunter, J. C., Preparation of a New Crystal Form of Manganese-Dioxide - Lambda-Mno2. *Journal of Solid State Chemistry* **1981,** 39, (2), 142-147.

62. Alias, N.; Mohamad, A. A., Advances of aqueous rechargeable lithium-ion battery: A review. *Journal of Power Sources* **2015,** 274, 237-251.

63. Cachet-Vivier, C.; Bach, S.; Pereira-Ramos, J. P., Electrochemical proton insertion in manganese spinel oxides from aqueous borate solution. *Electrochimica Acta* **1999,** 44, (16), 2705-2709.

64. Abu Eldahab, Y. E.; Saad, N. H.; Zekry, A., Enhancing the design of battery charging controllers for photovoltaic systems. *Renewable & Sustainable Energy Reviews* **2016,** 58, 646-655.

65. Schmeisser, D.; Schmidt, S.; Seibold, G.; Cherkashinin, G.; Jaegermann, W., Localized Gap States in LiCoO2 and Their Influence on the Transport Properties in Li Ion Batteries. *Battery/Energy Technology (General) - 216th Ecs Meeting* **2010,** 25, (35), 37-45.

66. Tsuruhama, T.; Hitosugi, T.; Oki, H.; Hirose, Y.; Hasegawa, T., Preparation of Layered-Rhombohedral LiCoO2 Epitaxial Thin Films Using Pulsed Laser Deposition. *Applied Physics Express* **2009,** 2, (8).

67. Bushkova, O. V.; Andreev, O. L.; Batalov, N. N.; Shkerin, S. N.; Kuznetsov, M. V.; Tyutyunnik, A. P.; Koryakova, O. V.; Song, E. H.; Chung, H. J., Chemical interactions in the cathode half-cell of lithium-ion batteries - Part I. Thermodynamic simulation. *Journal of Power Sources* **2006,** 157, (1), 477-482.

68. Zhu, X. J.; Zhan, H.; Zhou, Y. H., Synthesis, structure and electrochemical behavior of LiNi0.85Co0.15O2. *Acta Chimica Sinica* **2002,** 60, (10), 1742-1746.

69. Lee, D. H.; Carroll, K. J.; Chapman, K. W.; Borkiewicz, O. J.; Calvin, S.; Fullerton, E. E.; Meng, Y. S., Understanding improved electrochemical properties of NiO-doped NiF2-C composite conversion materials by X-ray absorption spectroscopy and pair distribution function analysis. *Physical Chemistry Chemical Physics* **2014,** 16, (7), 3095-3102.

70. Kim, Y.; Kim, S.; Choi, S., First-principles study of the change in the electronic properties of NiF2 by the introduction of oxygen. *Journal of Molecular Structure* **2013,** 1054, 293-296.

71. Lee, D. H.; Carroll, K. J.; Calvin, S.; Jin, S. H.; Meng, Y. S., Conversion mechanism of nickel fluoride and NiO-doped nickel fluoride in Li ion batteries. *Electrochimica Acta* **2012,** 59, 213-221.

72. Stock, B. D. C. a. S. R., *Elements of X-ray Diffraction*. 3rd ed.; Addison-Weshley Publishing Company, Inc.: 1956.

73. Fernandes, J. B.; Desai, B. D.; Dalal, V. N. K., Manganese-Dioxide - a Review of a Battery Chemical .1. Chemical Syntheses and X-Ray-Diffraction Studies of Manganese Dioxides. *Journal of Power Sources* **1985,** 15, (4), 209-237.

74. Lider, V. V., X-ray backscattering (diffraction at a Bragg angle of pi/2): A review. *Crystallography Reports* **2012,** 57, (5), 628-647.

75. Gerard, N., Heating Cells for X-Ray Diffraction Analysis . A General Review. *Bulletin De La Societe Chimique De France* **1970**, (1), 103-+.

76. Kagan, A. S.; Unikel, A. P., Method of Moments in X-Ray-Diffraction Analysis - (Review). *Industrial Laboratory* **1980,** 46, (5), 431-442.

77. Bolotina, N. B., X-ray diffraction analysis of modulated crystals: Review. *Crystallography Reports* **2007,** 52, (4), 647-658.

78. Ballaran, T. B.; Kurnosov, A.; Trots, D., Single-crystal X-ray diffraction at extreme conditions: a review. *High Pressure Research* **2013,** 33, (3), 453-465.

79. Das, R.; Ali, M. E.; Abd Hamid, S. B., Current Applications of X-Ray Powder Diffraction - a Review. *Reviews on Advanced Materials Science* **2014,** 38, (2), 95-109.

80. Milligan, W. O., A Review of the Application of X-Ray and Electron Diffraction Methods to Contact Catalysis. *Physical Review* **1945,** 67, (5-6), 197-197.

81. Midgley, P. A.; Eggeman, A. S., Precession electron diffraction - a topical review. *Iucrj* **2015,** 2, 126-136.

82. Baba-Kishi, K. Z., Review - Electron backscatter Kikuchi diffraction in the scanning electron microscope for crystallographic analysis. *Journal of Materials Science* **2002,** 37, (9), 1715-1746.

83. Dore, J. C.; Garawi, M.; Bellissent-Funel, M. C., Neutron diffraction studies of the structure of water at ambient temperatures, revisited [a review of past developments and current problems]. *Molecular Physics* **2004,** 102, (19-20), 2015-2035.

84. Zaccai, G., Lipids, Membrane-Proteins and Natural Membranes Studied by Neutron-Scattering and Diffraction - a Review. *Physica B & C* **1986,** 136, (1-3), 227-231.

85. Hussain, M. S., Neutron-Diffraction - a Review of Structural Studies of Short Hydrogen-Bonds. *Arabian Journal for Science and Engineering* **1983,** 8, (4), 355-366.

86. Clarke, D. R., Image Contrast in Scanning Electron Microscope - Review. *Journal of Materials Science* **1970,** 5, (8), 689-&.

87. Hollenberg, M. J.; Erickson, A. M., Scanning Electron-Microscope - Potential Usefulness to Biologists - Review. *Journal of Histochemistry & Cytochemistry* **1973,** 21, (2), 109-130.

88. Clarke, I. C., Articular-Cartilage - Review and Scanning Electron-Microscope Study .2. Territorial Fibrillar Architecture. *Journal of Anatomy* **1974,** 118, (Nov), 261-280.

89. Pool, D. W.; Chubb, J. C., A Critical Scanning Electron-Microscope Study of the Scolex of Bothriocephalus-Acheilognathi Yamaguti, 1934, with a Review of the Taxonomic History of the Genus Bothriocephalus Parasitizing Cyprinid Fishes. *Systematic Parasitology* **1985,** 7, (3), 199-211.

90. Lorimer, G. W., Quantitative X-Ray-Microanalysis of Thin Specimens in the Transmission Electron-Microscope - a Review. *Mineralogical Magazine* **1987,** 51, (359), 49-60.

91. Hinks, J. A., A review of transmission electron microscopes with in situ ion irradiation. *Nuclear Instruments & Methods in Physics Research Section B-Beam Interactions with Materials and Atoms* **2009,** 267, (23-24), 3652-3662.

92. Aranda, M. A. G., Recent studies of cements and concretes by synchrotron radiation crystallographic and cognate methods. *Crystallography Reviews* **2016,** 22, (3), 150-196.

93. Baden, E.; Jones, J. R.; Khedekar, R.; Burns, W. A., Neurofibromatosis of Tongue - Study by Optical and Electron Microscopies with Review of Literature from 1849 to 1977. *Archives D Anatomie Et De Cytologie Pathologiques* **1979,** 27, (1), 64-64.

94. Piper, J., A review of high-grade imaging of diatoms and radiolarians in light microscopy optical- and software-based techniques. *Diatom Research* **2011,** 26, (1-2), 57-72.

95. Lereu, A. L.; Passian, A.; Dumas, P., Near field optical microscopy: a brief review. *International Journal of Nanotechnology* **2012,** 9, (3-7), 488-501.

96. Lucas, M.; Riedo, E., Invited Review Article: Combining scanning probe microscopy with optical spectroscopy for applications in biology and materials science. *Review of Scientific Instruments* **2012,** 83, (6).

97. Adam, J. F.; Moy, J. P.; Susini, J., Table-top water window transmission x-ray microscopy: Review of the key issues, and conceptual design of an instrument for biology. *Review of Scientific Instruments* **2005,** 76, (9).

98. Yagodkin, Y. D.; Dobatkin, S. V., Application of electron microscopy and x-ray structural analysis for the determination of sizes of structural elements in nanocrystalline materials (Review). *Inorganic Materials* **2008,** 44, (14), 1520-1530.

99. Mottana, A., X-ray absorption spectroscopy in mineralogy: A review. *X-Ray and Inner-Shell Processes* **2003,** 652, 415-437.

100. Love, C. T.; Korovina, A.; Patridge, C. J.; Swider-Lyons, K. E.; Twigg, M. E.; Ramaker, D. E., Review of LiFePO4 Phase Transition Mechanisms and New Observations from X-ray Absorption Spectroscopy. *Journal of the Electrochemical Society* **2013,** 160, (5), A3153-A3161.

101. Grafe, M.; Donner, E.; Collins, R. N.; Lombi, E., Speciation of metal(loid)s in environmental samples by X-ray absorption spectroscopy: A critical review. *Analytica Chimica Acta* **2014,** 822, 1-22.

102. Crozier, E. D., A review of the current status of XAFS spectroscopy. *Nuclear Instruments & Methods in Physics Research Section B-Beam Interactions with Materials and Atoms* **1997,** 133, (1-4), 134-144.

103. Nagasaka, M.; Yuzawa, H.; Kosugi, N., Development and application of in situ/operando soft X-ray transmission cells to aqueous solutions and catalytic and electrochemical reactions. *Journal of Electron Spectroscopy and Related Phenomena* **2015,** 200, 293-310.

104. Bazin, D.; Guczi, L., A review of in situ XAS study on Co-based bimetallic catalysts relevant to CO hydrogenation. *Natural Gas Conversion Vii* **2004,** 147, 343-348.

105. Kumar, A.; Miller, J. T.; Mukasyan, A. S.; Wolf, E. E., In situ XAS and FTIR studies of a multi-component Ni/Fe/Cu catalyst for hydrogen production from ethanol. *Applied Catalysis a-General* **2013,** 467, 593-603.

106. Rehr, J. J.; Ankudinov, A. L., New developments in the theory of X-ray absorption and core photoemission. *Journal of Electron Spectroscopy and Related Phenomena* **2001,** 114, 1115-1121.

107. Young, N. A., The application of synchrotron radiation and in particular X-ray absorption spectroscopy to matrix isolated species. *Coordination Chemistry Reviews* **2014,** 277, 224-274.

108. Newville, M., Fundamentals of XAFS. *Spectroscopic Methods in Mineralology and Materials Sciences* **2014,** 78, 33-74.

109. Rehr, J. J., Theory and calculations of X-ray spectra: XAS, XES, XRS, and NRIXS. *Radiation Physics and Chemistry* **2006,** 75, (11), 1547-1558.

110. Armaroli, N.; Accorsi, G.; Cardinali, F.; Listorti, A., Photochemistry and photophysics of coordination compounds: Copper. *Photochemistry and Photophysics of Coordination Compounds I* **2007,** 280, 69-115.

111. Apostol, N. G.; Teodorescu, C. M., Surface Reactivity and Magnetism at Metal-Semiconductor Interfaces. *Size Effects in Nanostructures: Basics and Applications* **2014,** 205, 239-292.

112. Brion, D.; Escard, J., General Review of Application of X-Ray Photoelectron-Spectroscopy to Quantitative Surface Characterizations. *Journal De Microscopie Et De Spectroscopie Electroniques* **1976,** 1, (2), 227-246.

113. Nanse, G.; Papirer, E.; Fioux, P.; Moguet, F.; Tressaud, A., Fluorination of carbon blacks: An X-ray photoelectron spectroscopy study .1. A literature review of XPS studies of fluorinated carbons. XPS investigation of some reference compounds. *Carbon* **1997,** 35, (2), 175-194.

114. Moretti, G., Auger parameter and Wagner plot in the characterization of chemical states by X-ray photoelectron spectroscopy: a review. *Journal of Electron Spectroscopy and Related Phenomena* **1998,** 95, (2-3), 95-144.

115. Kawai, J., Total reflection X-ray photoelectron spectroscopy: A review. *Journal of Electron Spectroscopy and Related Phenomena* **2010,** 178, 268-272.

116. Colliex, C.; Krivanek, O. L.; Trebbia, P., Electron-Energy Loss Spectroscopy in the Electron-Microscope - a Review of Recent Progress. *Institute of Physics Conference Series* **1982**, (61), 183-188.

117. Thiry, P. A., Vibrations Measured at Surfaces by High-Resolution Electron-Energy Loss Spectroscopy - Updated Review (1982-1985). *Journal of Electron Spectroscopy and Related Phenomena* **1986,** 39, (1-4), 273-288.

118. Zabegaeva, U. G.; Maksimov, S. K., Capabilities of the Electron-Energy Loss Spectroscopy Method in Electron-Microscope Studies (Review). *Industrial Laboratory* **1990,** 56, (3), 278-283.

119. Nemoshkalenko, V. V.; Uvarov, V. N.; Borisenko, S. V., The electron energy loss and inverse photoemission spectroscopy of some metal oxides (review). *Metallofizika I Noveishie Tekhnologii* **1995,** 17, (5), 3-33.

120. Brydson, R., A brief review of quantitative aspects of electron energy loss spectroscopy and imaging. *Materials Science and Technology* **2000,** 16, (10), 1187-1198.

121. Cherkouk, C.; Nestler, T., Cathodes - Technological Review. *Review on Electrochemical Storage Materials and Technology* **2014,** 1597, 134-145.

122. Peterson, V. K.; Papadakis, C. M., Functional materials analysis using in situ and in operando X-ray and neutron scattering. *Iucrj* **2015,** 2, 292-304.

123. Brant, W. R.; Schmid, S.; Du, G. D.; Brand, H. E. A.; Pang, W. K.; Peterson, V. K.; Guo, Z. P.; Sharma, N., In Situ Neutron Powder Diffraction Using Custom-made Lithium-ion Batteries. *Jove-Journal of Visualized Experiments* **2014**, (93).

124. Weker, J. N.; Toney, M. F., Emerging In Situ and Operando Nanoscale X-Ray Imaging Techniques for Energy Storage Materials. *Advanced Functional Materials* **2015,** 25, (11), 1622-1637.

125. Harks, P. P. R. M. L.; Mulder, F. M.; Notten, P. H. L., In situ methods for Li-ion battery research: A review of recent developments. *Journal of Power Sources* **2015,** 288, 92-105.

126. Nonnenmann, S. S., A hot tip: imaging phenomena using in situ multi-stimulus probes at high temperatures. *Nanoscale* **2016,** 8, (6), 3164-3180.

127. Ma, X. Y.; Luo, W.; Yan, M. Y.; He, L.; Mai, L. Q., In situ characterization of electrochemical processes in one dimensional nanomaterials for energy storages devices. *Nano Energy* **2016,** 24, 165-188.

128. Overgaard, J.; Larsen, F. K.; Schiott, B.; Iversen, B. B., Electron density distributions of redox active mixed valence carboxylate bridged trinuclear iron complexes. *Journal of the American Chemical Society* **2003,** 125, (36), 11088-11099.

129. Dutta, A. K.; Maji, S. K.; Dutta, S., A symmetric oxo-centered trinuclear chloroacetato bridged iron(III) complex: Structural, spectroscopic and electrochemical studies. *Journal of Molecular Structure* **2012,** 1027, 87-91.

130. Boudalis, A. K.; Sanakis, Y.; Dahan, F.; Hendrich, M.; Tuchagues, J. P., An octanuclear complex containing the [Fe3O]7+ metal core: structural, magnetic, Mossbauer, and electron paramagnetic resonance studies. *Inorg Chem* **2006,** 45, (1), 443-53.

131. Taylor-Pashow, K.; Della Rocca, J.; Xie, Z.; Tran, S.; Lin, W., Postsynthetic modifications of iron-carboxylate nanoscale metal-organic frameworks for imaging and drug delivery. *Journal of the American Chemical Society* **2009,** 131, (40), 14261-14263.

132. Férey, G.; Millange, F.; Morcrette, M.; Serre, C.; Doublet, M. L.; Greneche, J. M.; Tarascon, J. M., Mixed-valence Li/Fe-based metal-organic frameworks with both reversible redox and sorption properties. *Angewandte Chemie-International Edition* **2007,** 46, (18), 3259-3263.

133. Schafer, A.; Huber, C.; Ahlrichs, R., Fully Optimized Contracted Gaussian-Basis Sets of Triple Zeta Valence Quality for Atoms Li to Kr. *Journal of Chemical Physics* **1994,** 100, (8), 5829-5835.

134. Férey, G.; Mellot-Draznieks, C.; Serre, C.; Millange, F.; Dutour, J.; Surblé, S.; Margiolaki, I., A chromium terephthalate-based solid with unusually large pore volumes and surface area. *Science (New York, N.Y.)* **2005,** 309, (5743), 2040-2042.

135. Armand, M.; Grugeon, S.; Vezin, H.; Laruelle, S.; Ribière, P.; Poizot, P.; Tarascon, J. M., Conjugated dicarboxylate anodes for Li-ion batteries. *Nature materials* **2009,** 8, (2), 120-125.

136. Chen, H.; Armand, M.; Demailly, G.; Dolhem, F.; Poizot, P.; Tarascon, J. M., From biomass to a renewable LixC6O6 organic electrode for sustainable Li-ion batteries. *ChemSusChem* **2008,** 1, (4), 348-355.

137. Le Gall, T.; Reiman, K. H.; Grossel, M. C.; Owen, J. R., Poly(2,5-dihydroxy-1,4-benzoquinone-3,6-methylene): a new organic polymer as positive electrode material for rechargeable lithium batteries. *Journal of Power Sources* **2003,** 119, 316-320.

138. Qu, J. Q.; Katsumata, T.; Satoh, M.; Wada, J.; Masuda, T., Synthesis and properties of polyacetylene and polynorbornene derivatives carrying 2,2,5,5-tetramethyl-1-pyrrolidinyloxy moieties. *Macromolecules* **2007,** 40, (9), 3136-3144.

139. Nishide, H.; Iwasa, S.; Pu, Y. J.; Suga, T.; Nakahara, K.; Satoh, M., Organic radical battery: nitroxide polymers as a cathode-active material. *Electrochimica Acta* **2004,** 50, (2-3), 827-831.

140. Toussaint, G.; Stevens, P.; Akrour, L.; Rouget, R.; Fourgeot, F., Development of a rechargeable zinc-air battery. *Metal/Air and Metal/Water Batteries* **2010,** 28, (32), 25-34.

141. Chen, H.; Cong, T. N.; Yang, W.; Tan, C.; Li, Y.; Ding, Y., Progress in electrical energy storage system: A critical review. *Progress in Natural Science* **2009,** 19, (3), 291-312.

142. Kim, H. I.; Kim, E. J.; Kim, S. J.; Shin, H. C., Influence of ZnO precipitation on the cycling stability of rechargeable Zn-air batteries. *Journal of Applied Electrochemistry* **2015,** 45, (4), 335-342.

143. Minakshi, M., Alkaline-Earth Oxide Modified MnO2 Cathode: Enhanced Performance in an Aqueous Rechargeable Battery. *Industrial & Engineering Chemistry Research* **2011,** 50, (14), 8792-8795.

144. Ma, H.; Li, C. S.; Su, Y.; Chen, J., Studies on the vapour-transport synthesis and electrochemical properties of zinc micro-, meso- and nanoscale structures. *Journal of Materials Chemistry* **2007,** 17, (7), 684-691.

145. Li, Q.; Xu, P.; Zhang, B.; Tsai, H. H.; Wang, J.; Wang, H. L.; Wu, G., One-step synthesis of Mn3O4/reduced graphene oxide nanocomposites for oxygen reduction in nonaqueous Li-O-2 batteries. *Chemical Communications* **2013,** 49, (92), 10838-10840.

146. Liu, Z.; Cui, T.; Pulletikurthi, G.; Lahiri, A.; Carstens, T.; Olschewski, M.; Endres, F., Dendrite-Free Nanocrystalline Zinc Electrodeposition from an Ionic Liquid Containing Nickel Triflate for Rechargeable Zn-Based Batteries. *Angewandte Chemie-International Edition* **2016,** 55, (8), 2889-2893.

147. Mcbreen, J.; Gannon, E., Bismuth Oxide as an Additive in Pasted Zinc Electrodes. *Journal of Power Sources* **1985,** 15, (2-3), 169-177.

148. Mcbreen, J.; Gannon, E., The Electrochemistry of Metal-Oxide Additives in Pasted Zinc Electrodes. *Electrochimica Acta* **1981,** 26, (10), 1439-1446.

149. Simons, T. J.; Salsamendi, M.; Howlett, P. C.; Forsyth, M.; MacFarlane, D. R.; Pozo-Gonzalo, C., Rechargeable Zn/PEDOT Battery with an Imidazolium-Based Ionic Liquid as the Electrolyte. *Chemelectrochem* **2015,** 2, (12), 2071-2078.

150. Huang, H.; Gu, S. J.; Gan, Y. P.; Tao, X. Y.; Zhang, W. K., ZnO/ZnO-Bi2O3 nanocomposite as an anode material for Ni-Zn rechargeable battery. *Advances in Chemical Engineering, Pts 1-3* **2012,** 396-398, 1725-1729.

151. Moser, F.; Fourgeot, F.; Rouget, R.; Crosnier, O.; Brousse, T., In situ X-ray diffraction investigation of zinc based electrode in Ni-Zn secondary batteries. *Electrochimica Acta* **2013,** 109, 110-116.

152. Harwig, H. A.; Gerards, A. G., Electrical-Properties of Alpha, Beta, Gamma and Delta Phases of Bismuth Sesquioxide. *Journal of Solid State Chemistry* **1978,** 26, (3), 265-274.

153. Tao, H. S.; Tong, X.; Gan, L.; Zhang, S. Q.; Zhang, X. M.; Liu, X., Effect of adding various carbon additives to porous zinc anode in rechargeable hybrid aqueous battery. *Journal of Alloys and Compounds* **2016,** 658, 119-124.

154. Berchmans, S.; Bandodkar, A. J.; Jia, W. Z.; Ramirez, J.; Meng, Y. S.; Wang, J., An epidermal alkaline rechargeable Ag-Zn printable tattoo battery for wearable electronics. *Journal of Materials Chemistry A* **2014,** 2, (38), 15788-15795.

155. Peles, A.; Pavlovic, V. P.; Filipovic, S.; Obradovic, N.; Mancic, L.; Krstic, J.; Mitric, M.; Vlahovic, B.; Rasic, G.; Kosanovic, D.; Pavlovic, V. B., Structural investigation of mechanically activated ZnO powder. *Journal of Alloys and Compounds* **2015,** 648, 971-979.

156. Liu, H. F.; Tripathy, S.; Hu, G. X.; Gong, H., Surface optical phonon and A(1)(LO) in ZnO submicron crystals probed by Raman scattering: Effects of morphology and dielectric coating. *Journal of Applied Physics* **2009,** 105, (5).

157. Prutton, M., *Surface Physics*. 2 ed.; Thetford, Oxford University Press: 1983.

158. Tringe, J. W.; Levie, H. W.; McCall, S. K.; Teslich, N. E.; Wall, M. A.; Orme, C. A.; Matthews, M. J., Enhanced Raman scattering and nonlinear conductivity in Ag-doped hollow ZnO microspheres. *Applied Physics a-Materials Science & Processing* **2012,** 109, (1), 15-23.

159. Nakata, A.; Arai, H.; Yamane, T.; Hirai, T.; Ogumi, Z., Preserving Zinc Electrode Morphology in Aqueous Alkaline Electrolytes Mixed with Highly Concentrated Organic Solvent. *Journal of the Electrochemical Society* **2016,** 163, (2), A50-A56.

160. Fan, H. Y.; Wang, G. N.; Hu, L. L., Infrared, Raman and XPS spectroscopic studies of Bi2O3-B2O3-Ga2O3 glasses. *Solid State Sciences* **2009,** 11, (12), 2065-2070.

161. Tahar, N. B.; Savall, A., Electrochemical degradation of phenol in aqueous solution on bismuth doped lead dioxide: a comparison of the activities of various electrode formulations. *Journal of Applied Electrochemistry* **1999,** 29, (3), 277-283.

162. Wang, X. J.; Liu, N.; Shi, S.; Chen, Y. X., XPS Depth Study on the Liquid Oxidation of Sn-Bi-Zn-X(Al/P) Alloy and the Effect of Al/P on the Film. *Advances in Materials Science and Engineering* **2015**.

163. Hanna, T. A.; Rieger, A. L.; Rieger, P. H.; Wang, X. Y., Evidence for an unstable Bi(II) radical from Bi-O bond homolysis. Implications in the rate-determining step of the SOHIO process. *Inorganic Chemistry* **2002,** 41, (14), 3590-3592.

164. Gaikwad, A. M.; Zamarayeva, A. M.; Rousseau, J.; Chu, H. W.; Derin, I.; Steingart, D. A., Highly Stretchable Alkaline Batteries Based on an Embedded Conductive Fabric. *Advanced Materials* **2012,** 24, (37), 5071-5076.

165. Gupta, T.; Kim, A.; Phadke, S.; Biswas, S.; Luong, T.; Hertzberg, B. J.; Chamoun, M.; Evans-Lutterodt, K.; Steingart, D. A., Improving the cycle life of a high-rate, high-potential aqueous dual ion battery using hyper-dendritic zinc and copper hexacyanoferrate. *Journal of Power Sources* **2016,** 305, 22-29.

166. Minakshi, M.; Ionescu, M., Anodic behavior of zinc in Zn-MnO2 battery using ERDA technique. *International Journal of Hydrogen Energy* **2010,** 35, (14), 7618-7622.

167. Minakshi, M.; Appadoo, D.; Martin, D. E., The Anodic Behavior of Planar and Porous Zinc Electrodes in Alkaline Electrolyte. *Electrochemical and Solid State Letters* **2010,** 13, (7), A77-A80.

168. Lee, S. M.; Kim, Y. J.; Eom, S. W.; Choi, N. S.; Kim, K. W.; Cho, S. B., Improvement in self-discharge of Zn anode by applying surface modification for Zn-air batteries with high energy density. *Journal of Power Sources* **2013,** 227, 177-184.

169. Yano, M.; Fujitani, S.; Nishio, K.; Akai, Y.; Kurimura, M., Effect of additives in zinc alloy powder on suppressing hydrogen evolution. *Journal of Power Sources* **1998,** 74, (1), 129-134.

170. Guha, J. P.; Kune, S.; Suvorov, D., Phase equilibrium relations in the binary system Bi2O3-ZnO. *Journal of Materials Science* **2004,** 39, (3), 911-918.

171. Radaev, S. F.; Simonov, V. I., Structure of Sillenites and Atomic Mechanisms of Isomorphous Substitutions in Them. *Kristallografiya* **1992,** 37, (4), 914-941.

172. Mel'nikova, T. I.; Kuz'micheva, G. M.; Bolotina, N. B.; Rybakov, V. B.; Zubavichus, Y. V.; Sadovskaya, N. V.; Mar'ina, E. A., Structural features of compounds of the sillenite family. *Crystallography Reports* **2014,** 59, (3), 353-361.

173. Yogeswaran, U.; Chen, S. M., Recent trends in the application of carbon nanotubes-polymer composite modified electrodes for biosensors: A review. *Analytical Letters* **2008,** 41, (2), 210-243.

174. Inamuddin; Alam, M. M., Studies on the Preparation and Analytical Applications of Various Metal Ion-Selective Membrane Electrodes Based on Polymeric, Inorganic and Composite MaterialsA Review. *Journal of Macromolecular Science Part a-Pure and Applied Chemistry* **2008,** 45, (12), 1086-1103.

175. Liu, X. M.; Huang, Z. D.; Oh, S. W.; Zhang, B.; Ma, P. C.; Yuen, M. M. F.; Kim, J. K., Carbon nanotube (CNT)-based composites as electrode material for rechargeable Li-ion batteries: A review. *Composites Science and Technology* **2012,** 72, (2), 121-144.

176. Zhi, M. J.; Xiang, C. C.; Li, J. T.; Li, M.; Wu, N. Q., Nanostructured carbon-metal oxide composite electrodes for supercapacitors: a review. *Nanoscale* **2013,** 5, (1), 72-88.

177. Chae, J. H.; Ng, K. C.; Chen, G. Z., Nanostructured materials for the construction of asymmetrical supercapacitors. *Proceedings of the Institution of Mechanical Engineers Part a-Journal of Power and Energy* **2010,** 224, (A4), 479-503.

178. Ho, M. Y.; Khiew, P. S.; Isa, D.; Tan, T. K.; Chiu, W. S.; Chia, C. H., A Review of Metal Oxide Composite Electrode Materials for Electrochemical Capacitors. *Nano* **2014,** 9, (6).

179. Sk, M. M.; Yue, C. Y.; Ghosh, K.; Jena, R. K., Review on advances in porous nanostructured nickel oxides and their composite electrodes for high-performance supercapacitors. *Journal of Power Sources* **2016,** 308, 121-140.

180. Bai, L.; Qu, D. Y.; Conway, B. E.; Zhou, Y. H.; Chowdhury, G.; Adams, W. A., Rechargeability of a Chemically Modified Mno2/Zn Battery System at Practically Favorable Power Levels. *Journal of the Electrochemical Society* **1993,** 140, (4), 884-889.

181. Sato, Y.; Kanda, M.; Niki, H.; Ueno, M.; Murata, K.; Shirogami, T.; Takamura, T., Long Life Sealed Nickel Zinc Cell Using a New Separator. *Journal of Power Sources* **1983,** 9, (2), 147-159.

182. Gu, W. T.; Borodin, O.; Zdyrko, B.; Lin, H. T.; Kim, H.; Nitta, N.; Huang, J. X.; Magasinski, A.; Milicev, Z.; Berdichevsky, G.; Yushin, G., Lithium-Iron Fluoride Battery with In Situ Surface Protection. *Advanced Functional Materials* **2016,** 26, (10), 1507-1516.

183. Joon Kyo Seo, H.-M. C., Katsunori Takahara, Karena W. Chapman, Olaf J. Borkiewicz, Mahsa Sina, and Y. Shirley Meng, Revisiting the conversion reaction voltage and the reversibility of CuF2 electrode in Li-ion batteries. In 2016.

184. Herbert, W. S., Fiftieth Anniversary: The Anniversary Issue on Primary Cell Systems: The Alkaline Manganese Dioxide Dry Cell. *Journal of The Electrochemical Society* **1952,** 99, (8), 190C-191C.

185. Gallaway, J. W.; Menard, M.; Hertzberg, B.; Zhong, Z.; Croft, M.; Sviridov, L. A.; Turney, D. E.; Banerjee, S.; Steingart, D. A.; Erdonmez, C. K., Hetaerolite Profiles in Alkaline Batteries Measured by High Energy EDXRD. *Journal of The Electrochemical Society* **2015,** 162, (1), A162-A168.

186. Hertzberg, B. J.; Huang, A.; Hsieh, A.; Chamoun, M.; Davies, G.; Seo, J. K.; Zhong, Z.; Croft, M.; Erdonmez, C.; Meng, Y. S.; Steingart, D., Effect of Multiple Cation Electrolyte Mixtures on Rechargeable Zn MnO2 Alkaline Battery. *Chemistry of Materials* **2016,** 28, (13), 4536-4545.

187. Johnson, C. S., Development and utility of manganese oxides as cathodes in lithium batteries. *Journal of Power Sources* **2007,** 165, (2), 559-565.

188. Jarvis, S. C., The Association of Cobalt with Easily Reducible Manganese in Some Acidic Permanent Grassland Soils. *Journal of Soil Science* **1984,** 35, (3), 431-438.

189. Mckeague, J. A.; Damman, A. W. H.; Heringa, P. K., Iron-Manganese and Other Pans in Some Soils of Newfoundland. *Canadian Journal of Soil Science* **1968,** 48, (3), 243-&.

190. Mckenzie, R. M., Synthesis of Birnessite, Cryptomelane, and Some Other Oxides and Hydroxides of Manganese. *Mineralogical Magazine* **1971,** 38, (296), 493-&.

191. Julien, C. M.; Massot, M.; Poinsignon, C., Lattice vibrations of manganese oxides: Part I. Periodic structures. *Spectrochimica Acta Part A: Molecular and Biomolecular Spectroscopy* **2004,** 60, (3), 689-700.

192. Thackeray, M. M., Manganese oxides for lithium batteries. *Progress in Solid State Chemistry* **1997,** 25, (1–2), 1-71.

193. Su, D.; Ahn, H. J.; Wang, G., Hydrothermal synthesis of alpha-MnO2 and beta-MnO2 nanorods as high capacity cathode materials for sodium ion batteries. *Journal of Materials Chemistry A* **2013,** 1, (15), 4845-4850.

194. Julien, C.; Massot, M.; Rangan, S.; Lemal, M.; Guyomard, D., Study of structural defects in γ-MnO2 by Raman spectroscopy. *Journal of Raman Spectroscopy* **2002,** 33, (4), 223-228.

195. Kanevskii, L. S.; Dubasova, V. S., Degradation of lithium-ion batteries and how to fight it: A review. *Russian Journal of Electrochemistry* **2005,** 41, (1), 1-16.

196. Wu, C.; Zhu, C. B.; Ge, Y. W.; Zhao, Y. P., A Review on Fault Mechanism and Diagnosis Approach for Li-Ion Batteries. *Journal of Nanomaterials* **2015**.

197. Minakshi, M.; Singh, P., Synergistic effect of additives on electrochemical properties of MnO2 cathode in aqueous rechargeable batteries. *Journal of Solid State Electrochemistry* **2012,** 16, (4), 1487-1492.

198. Kartini, E.; Putra, T. P.; Jahya, A. K.; Insani, A.; Adams, S., Neutron Scattering Study on Cathode LiMn2O4 and Solid Electrolyte 5(Li2O)(P2O5). *4th International Conference on Advances in Nuclear Science and Engineering (Icanse 2013)* **2014,** 1615, 24-32.

199. Fillaux, F.; Cachet, C.; Parker, S. F.; Tomkinson, J.; Quivy, A.; Yu, L. T., Inelastic neutron scattering studies of the proton dynamics in bi-doped manganese oxides. *Journal of the Electrochemical Society* **2000,** 147, (11), 4184-4188.

200. Kijima, N.; Ikeda, T.; Oikawa, K.; Izumi, F.; Yoshimura, Y., Crystal structure of an open-tunnel oxide alpha-MnO2 analyzed by Rietveld refinements and MEM-based pattern fitting. *Journal of Solid State Chemistry* **2004,** 177, (4-5), 1258-1267.

201. Tseng, L. T.; Lu, Y. H.; Fan, H. M.; Wang, Y. R.; Luo, X.; Liu, T.; Munroe, P.; Li, S.; Yi, J. B., Magnetic properties in alpha-MnO2 doped with alkaline elements. *Scientific Reports* **2015,** 5.

202. Patrice, R.; Gerand, B.; Leriche, J. B.; Seguin, L.; Wang, E.; Moses, R.; Brandt, K.; Tarascon, J. M., Understanding the second electron discharge plateau in MnO2-based alkaline cells. *Journal of the Electrochemical Society* **2001,** 148, (5), A448-A455.

203. Mandal, S.; Andreanov, A.; Crespo, Y.; Seriani, N., Incommensurate helical spin ground states on the hollandite lattice. *Physical Review B* **2014,** 90, (10).

204. Shin, J.; Kim, M.; Cirera, J.; Chen, S.; Halder, G. J.; Yersak, T. A.; Paesani, F.; Cohen, S. M.; Meng, Y. S., MIL-101(Fe) as a lithium-ion battery electrode material: a relaxation and intercalation mechanism during lithium insertion. *Journal of Materials Chemistry A* **2015,** 3, (8), 4738-4744.

205. Bowden, W.; Bofinger, T.; Zhang, F.; Iltchev, N.; Sirotina, R.; Paik, Y.; Chen, H.; Grey, C.; Hackney, S., New manganese dioxides for lithium batteries. *Journal of Power Sources* **2007,** 165, (2), 609-615.

206. Fey, G. T. K.; Kao, H. M.; Muralidharan, P.; Kumar, T. P.; Cho, Y. D., Electrochemical and solid-state NMR studies on LiCoO2 coated with Al2O3 derived from carboxylate-alumoxane. *Journal of Power Sources* **2006,** 163, (1), 135-143.

207. Grey, C. P.; Lee, Y. J., Lithium MAS NMR studies of cathode materials for lithium-ion batteries. *Solid State Sciences* **2003,** 5, (6), 883-894.

208. Amalraj, S. F.; Aurbach, D., The use of in situ techniques in R&D of Li and Mg rechargeable batteries. *Journal of Solid State Electrochemistry* **2011,** 15, (5), 877-890.

209. Gu, W. T.; Yushin, G., Review of nanostructured carbon materials for electrochemical capacitor applications: advantages and limitations of activated carbon, carbide-derived carbon, zeolite-templated carbon, carbon aerogels, carbon nanotubes, onion-like carbon, and graphene. *Wiley Interdisciplinary Reviews-Energy and Environment* **2014,** 3, (5), 424-473.

210. Woo, S. I.; Kim, K. W.; Cho, H. Y.; Oh, K. S.; Jeon, M. K.; Tarte, N. H.; Kim, T. S.; Mahmood, A., Current status of combinatorial and high-throughput methods for discovering new materials and catalysts. *Qsar & Combinatorial Science* **2005,** 24, (1), 138-154.

211. Saal, J. E.; Kirklin, S.; Aykol, M.; Meredig, B.; Wolverton, C., Materials Design and Discovery with High-Throughput Density Functional Theory: The Open Quantum Materials Database (OQMD). *Jom* **2013,** 65, (11), 1501-1509.

212. Koyama, M.; Tsuboi, H.; Endou, A.; Takaba, H.; Kubo, M.; Del Carpio, C. A.; Miyamoto, A., Combinatorial computational chemistry approach for materials design: Applications in deNOx catalysis, Fischer-Tropsch synthesis, lanthanoid complex, and lithium ion secondary battery. *Combinatorial Chemistry & High Throughput Screening* **2007,** 10, (2), 99-110.

213. Kafizas, A.; Parkin, I. P., Inorganic thin-film combinatorial studies for rapidly optimising functional properties. *Chemical Society Reviews* **2012,** 41, (2), 738-781.